

# Development of the X-57 Aerodynamic Database

*Michael A. Frederick, Mark S. Smith, Seung Y. Yoo, Ryan Wallace  
Armstrong Flight Research Center, Edwards, California, 93523*

*Jared C. Duensing, Jeffrey A. Housman  
Ames Research Center, Moffett Field, California, 94043*

*Karen A. Deere, Jeffrey K. Viken  
Langley Research Center, Hampton, Virginia, 23681*

## NASA STI Program Report Series

Since its founding, NASA has been dedicated to the advancement of aeronautics and space science. The NASA scientific and technical information (STI) program plays a key part in helping NASA maintain this important role.

The NASA STI program operates under the auspices of the Agency Chief Information Officer. It collects, organizes, provides for archiving, and disseminates NASA's STI. The NASA STI program provides access to the NTRS Registered and its public interface, the NASA Technical Reports Server, thus providing one of the largest collections of aeronautical and space science STI in the world. Results are published in both non-NASA channels and by NASA in the NASA STI Report Series, which includes the following report types:

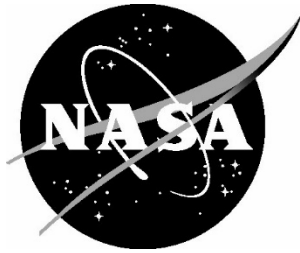
- **TECHNICAL PUBLICATION.** Reports of completed research or a major significant phase of research that present the results of NASA Programs and include extensive data or theoretical analysis. Includes compilations of significant scientific and technical data and information deemed to be of continuing reference value. NASA counterpart of peer-reviewed formal professional papers but has less stringent limitations on manuscript length and extent of graphic presentations.
- **TECHNICAL MEMORANDUM.** Scientific and technical findings that are preliminary or of specialized interest, e.g., quick release reports, working papers, and bibliographies that contain minimal annotation. Does not contain extensive analysis.
- **CONTRACTOR REPORT.** Scientific and technical findings by NASA-sponsored contractors and grantees.

- **CONFERENCE PUBLICATION.** Collected papers from scientific and technical conferences, symposia, seminars, or other meetings sponsored or co-sponsored by NASA.
- **SPECIAL PUBLICATION.** Scientific, technical, or historical information from NASA programs, projects, and missions, often concerned with subjects having substantial public interest.
- **TECHNICAL TRANSLATION.** English-language translations of foreign scientific and technical material pertinent to NASA's mission.

Specialized services also include organizing and publishing research results, distributing specialized research announcements and feeds, providing information desk and personal search support, and enabling data exchange services.

For more information about the NASA STI program, see the following:

- Access the NASA STI program home page at <http://www.sti.nasa.gov>



# Development of the X-57 Aerodynamic Database

*Michael A. Frederick, Mark S. Smith, Seung Y. Yoo, Ryan Wallace  
Armstrong Flight Research Center, Edwards, California, 93523*

*Jared C. Duensing, Jeffrey A. Houseman  
Ames Research Center, Moffett Field, California, 94043*

*Karen A. Deere, Jeffrey K. Viken  
Langley Research Center, Hampton, Virginia, 23681*

National Aeronautics and  
Space Administration

Armstrong Flight Research Center  
Edwards, California, 93523

---

April 2025

The use of trademarks or names of manufacturers in this report is for accurate reporting and does not constitute an official endorsement, either expressed or implied, of such products or manufacturers by the National Aeronautics and Space Administration.

Available from:

NASA STI Program / Mail Stop 050  
NASA Langley Research Center  
Hampton, VA 23681-2199

## Table of Contents

Abstract .....	1
Nomenclature .....	1
Symbols .....	3
1 Introduction .....	3
2 Configuration Descriptions.....	5
2.1 Modification-III .....	5
2.2 Modification-IV .....	5
3 Database Sources .....	6
3.1 Computational Fluid Dynamics Solver Descriptions .....	6
3.1.1 STAR-CCM+® .....	7
3.1.2 Launch Ascent and Vehicle Aerodynamics .....	8
3.1.3 USM3D.....	9
3.1.4 Kestrel.....	9
4 Steady-State Computational Fluid Dynamics Results .....	10
4.1 Modification-III Power Off.....	11
4.1.1 Longitudinal Results .....	12
4.1.2 Lateral-Directional Results .....	12
4.1.3 Control Surface Deflection Results .....	13
4.2 Modification-III Cruise Motor Effects .....	14
4.3 Modification-IV High-lift System.....	16
4.3.1 Nominal Operation .....	17
4.3.1.1 Longitudinal Results .....	17
4.3.1.2 Lateral-Directional Results .....	18
4.3.1.3 Control Surface Results .....	18
4.3.2 Contactor Failures.....	19
4.3.2.1 Longitudinal Results .....	20
4.3.2.2 Lateral-Directional Results .....	20
4.3.2.3 Control Surface Deflections.....	20
4.4 Ground Effect.....	21
5 Forced Oscillation Computational Fluid Dynamics Results.....	21
5.1 Forced Oscillation Data Reduction Method.....	21
5.2 Power-Off Results.....	22
5.2.1 Longitudinal Derivatives .....	22
5.2.2 Lateral-Directional Derivatives .....	22
5.3 High-Lift Power .....	23

5.3.1	Longitudinal Derivatives .....	23
5.3.2	Lateral-Directional Derivatives .....	23
6	Construction of the Database .....	23
6.1	Aerodynamic Model Structure .....	23
6.2	Uncertainties .....	24
6.3	Baseline Model .....	24
6.4	Cruise Propeller Effects .....	25
6.5	High-Lift Propeller Effects.....	25
6.6	High-Lift Propeller Contactor Failure Models .....	25
7	Summary.....	25
8	Figures .....	26
9	References .....	60

## Abstract

An aerodynamic database for the National Aeronautics and Space Administration X-57 Maxwell all-electric airplane project was created and used for a desktop and piloted flight simulation capability. The database was generated from Computational Fluid Dynamics estimates obtained from four different Computational Fluid Dynamics solvers by teams from three National Aeronautics and Space Administration Centers: Armstrong Flight Research Center, Ames Research Center, and the Langley Research Center. In total, over 2,500 different Computational Fluid Dynamics simulations were run to create the database, which models the steady-state aerodynamics of both free flight and ground effect, the dynamic derivatives, and the aerodynamic-propulsive effects of the two wingtip-mounted cruise motors and the 12 high-lift motors distributed over the leading edge of the wing. The Computational Fluid Dynamics results showed that the wingtip-mounted motors for the Modification-III configuration provided approximately 4.8 percent reduction in cruise drag. For the Modification-IV configuration, the lift augmentation provided by the 12 high-lift motors yielded a lift coefficient in the range of 4.2 to 4.4, which exceeded the design goal of 3.95. The Computational Fluid Dynamics results from the various solvers were reduced and combined to create an aerodynamic model of the X-57 Modification-III and Modification-IV configurations that were then implemented in flight simulators to allow for airworthiness evaluations and mission planning.

## Nomenclature

AFRC	=	Armstrong Flight Research Center
AR	=	aspect ratio
ARC	=	Ames Research Center
ARMD	=	Aeronautics Research Mission Directorate
Amp	=	Ampere
BEM	=	blade element momentum
b	=	span
$\bar{c}$	=	mean aerodynamic chord
CAD	=	Computer Aided Design
CFD	=	Computational Fluid Dynamics
CFL	=	Courant-Friedrichs-Lewy
CGT	=	Chimera Grids Tools
Const	=	constant
$C_D$	=	drag coefficient
$C_L$	=	lift coefficient
$C_{L_{max}}$	=	maximum lift coefficient
$C_l$	=	rolling moment coefficient
$C_{L_p}$	=	roll damping coefficient
$C_{L_r}$	=	rolling moment coefficient due to yaw rate
$C_m$	=	pitching moment coefficient
$C_{m_q}$	=	pitch damping coefficient
$C_n$	=	yawing moment coefficient
$C_{n_p}$	=	yawing moment coefficient due to roll rate
$C_{n_r}$	=	yaw damping coefficient
$C_P$	=	power coefficient
$C_p$	=	pressure coefficient

$C_{Power\ on}$	=	generalized aerodynamic coefficient, power on (cruise or high lift)
$C_{Power\ off}$	=	generalized aerodynamic coefficient, power off (cruise or high lift)
$C_Q$	=	torque coefficient
$C_T$	=	thrust coefficient
$C_Y$	=	side force coefficient
DEP	=	Distributed Electric Propulsion
D	=	drag force
d	=	propeller diameter
deg	=	degrees
EAS	=	equivalent airspeed
f	=	frequency
ft	=	feet
ft/s	=	foot per second
$F_X$	=	x-axis body force
$F_Y$	=	y-axis body force
$F_Z$	=	z-axis body force
HLP	=	high-lift propeller
Hp	=	pressure altitude
$h$	=	height above ground
hl	=	high lift
hp	=	horsepower
J	=	advance ratio
KEAS	=	knots equivalent airspeed
KCAS	=	knots calibrated airspeed
KIAS	=	knots indicated airspeed
Kn	=	knots
KTAS	=	knots true airspeed
k	=	non-dimensional frequency
kW	=	kilowatts
LaRC	=	Langley Research Center
LAVA	=	Launch, Ascent, and Vehicle Aerodynamics
Min	=	minimum
Max	=	maximum
lb	=	pound
lb <sub>f</sub>	=	pound force
$L$	=	lift force
LA	=	left battery bus A
LB	=	left battery bus B
M	=	Mach number
Mod	=	Modification
m	=	meter
m/s	=	meters per second
$M_x$	=	rolling moment
$M_y$	=	pitching moment
$M_z$	=	yawing moment
N	=	Newton
N•m	=	Newton-meter
NASA	=	National Aeronautics and Space Administration
Ops	=	operations
P	=	power
POR	=	percentage over range

prop	=	propeller
Q	=	torque
QCR2000	=	Quadratic Constitutive Relation
$\bar{q}$	=	dynamic pressure
$q$	=	pitch rate
RA	=	right battery bus A
RANS	=	Reynolds-averaged Navier-Stokes
RB	=	right battery bus B
RC	=	Rotation Curvature
$Re_c$	=	Reynolds number based on wing chord
RPM	=	revolutions per minute
stab	=	stabilator
s	=	seconds
sq ft	=	square feet
S	=	planform area
SA	=	Spallart-Allmaras
t	=	time
T	=	thrust
TE	=	trailing edge
V	=	true airspeed
$V_{inf}$	=	freestream velocity
$V_{S0}$	=	stall speed, landing configuration
$V_{S0hl}$	=	stall speed, landing configuration with high-lift system operative
$V_{S1}$	=	stall speed, takeoff configuration
$X_B$	=	x-axis, aircraft body axes
$X_S$	=	x-axis, aircraft stability axes
$Y_B$	=	y-axis, aircraft body axes
$Y_S$	=	y-axis, aircraft stability axes
$Z_B$	=	z-axis, aircraft body axes
$Z_S$	=	z-axis, aircraft stability axes

### Symbols

$\alpha$	=	angle of attack
$\beta$	=	angle of sideslip
$\beta_p$	=	propeller blade pitch angle
$\delta_a$	=	aileron deflection
$\delta_f$	=	flap deflection
$\delta_r$	=	rudder deflection
$\delta_s$	=	stabilator deflection
$\Delta$	=	change in coefficient
$\rho$	=	air density

## 1 Introduction

The National Aeronautics and Space Administration (NASA) Aeronautics Research Mission Directorate (ARMD) is working on technologies to develop environmentally sustainable aircraft (ref. 1). Electric aircraft may offer several potential advantages over existing internal combustion-propelled aircraft, such as a reduced reliance on fossil fuels, reduced carbon emissions, and a lower noise footprint (ref. 2). The NASA X-57 Maxwell electric airplane, shown in fig. 1, is an all-electric airplane being developed by NASA along with ESAero (San Luis Obispo, California) serving as the prime contractor. The objectives of the project are outlined in the diagram shown in fig. 2. A major design driver during the

development of the X-57 airplane is to demonstrate five times lower energy consumption compared to an equivalent light-twin, general aviation airplane powered by an internal combustion engine (ref. 3). The reduction in energy consumption is expected to come from a three-times increase in efficiency due to increased propulsive efficiency using electric propulsors and a further increase in efficiency of 1.5 times due to decreased drag from outfitting the airplane with a new, high-aspect-ratio wing, optimized for cruise efficiency.

The X-57 aircraft is a modified Tecnam P2006T (Costruzioni Aeronautiche TECNAM S.p.A, Capua, Italy) twin-engine airplane that has been outfitted with a traction battery system, electric motors, and motor controllers to replace the P2006T internal combustion engines. The X-57 effort was broken into different phases referred to as modifications or “Mods.” The Mod-I configuration was a short flight-test series using a rental P2006T airplane that had research instrumentation added to it to characterize the performance of the P2006T airplane. For Mod-II, a P2006T airplane, purchased for the X-57 effort, was converted to an electric airplane. The airplane was modified with a traction battery system to provide power for electric motors used for propulsion and to provide power for other aircraft systems. The traction batteries are a custom design using 18650 Commercial off the Shelf (COTS) lithium-ion batteries arranged into packs that are stored in the cabin of the aircraft. The total weight of the traction batteries is approximately 800 lb. A detailed description of the traction battery system can be found in ref. 4. The two gasoline engines that come with the P2006T airplane were replaced with two JM-57D electric motors, hereafter referred to as cruise motors, developed by Joby Aviation (Santa Cruz, California). The cruise motors are rated for a maximum torque of 255 Newton-meter ( $N\cdot m$ ) and provide 60 kW continuous shaft power at 2,250 revolutions per minute (RPM) and 72 kW peak power at 2,700 RPM. Each cruise motor was fitted with an MT-Propeller (Bavaria, Germany) MTV-7-A/152-64 three-bladed propeller with an electrically driven hub to control blade pitch. More information on the cruise motor design can be found in ref. 5.

The Mod-III configuration consists of the same traction battery system used in Mod-II, but the P2006T wing has been replaced with a new, high-aspect-ratio wing designed for a cruise speed of 150 kn (knots) true airspeed, at a pressure altitude of 8,000 ft. The electric cruise motors used in Mod-II are moved to the wingtips to help reduce induced drag by means of rotating the propellers counter to the direction of the wingtip vortices. The high-aspect-ratio Mod-III wing provides better cruise performance than the P2006T wing, but results in higher takeoff and landing speeds and generally worse low-speed performance. The Mod-IV configuration includes a high-lift system comprised of 12 electric motors and propellers distributed along the span of the leading edge of the new wing. The high-lift motors increase the maximum attainable lift coefficient to recover the low-speed performance of the P2006T airplane. Each high-lift motor is rated at 10.7 kW power. Illustrations showing the Mod-II, Mod-III, and Mod-IV configurations are shown in fig. 3. Note that the 12 high-lift motors are installed on the Mod-III wing, but the propeller blades are folded back, flush with the nacelle, and the motors are inactive for this configuration.

This report will focus on the development of the aerodynamic database that is used in flight simulations of the X-57 Mod-III and Mod-IV configurations. Two different simulations capabilities have been developed for the X-57 effort. First, a batch simulation, referred to as the desktop simulation, was developed using the Simulink® (The MathWorks Inc., Natick, Massachusetts) environment. The desktop simulation models most of the airplane systems such aerodynamics, propulsion, landing gear, mass properties, and the traction battery system in a 6-degree of freedom simulation of the flight dynamics of the airplane. This simulation is primarily used for model development and batch engineering analyses of the airplane. The second simulation used by the X-57 project is the NASA Armstrong Flight Research Center (AFRC) fixed-base piloted X-57 flight simulation. The piloted simulation setup (shown in fig. 4) features a cockpit representative of the X-57 airplane with flight controls, motor torque and speed levers, and a heads-down display. The outside field of view is projected on a wide, panoramic screen on the wall in front of the cockpit. The propulsion, aerodynamics, landing gear, and traction battery models used in the desktop simulation are converted to C-code using Simulink® Coder™ and implemented in the piloted simulation framework. Other models such as mass properties, landing gear, atmosphere, and equations of

motion are modeled using pre-existing AFRC-simulation models, adjusted, where applicable, for the X-57 airplane. The AFRC simulation model is used for airworthiness evaluations and for pilot training.

## 2 Configuration Descriptions

The aerodynamic database described in this report was developed to support airworthiness evaluations of the Mod-III and Mod-IV configurations via the aforementioned simulation capabilities. The Mod-II configuration retaining the P2006T wing was not expected to deviate appreciably from the P2006T aerodynamics and will not be discussed in this report. The following sections describe aspects of the outer-mold-line geometries of Mods III and IV that were relevant to the computational fluid dynamics (CFD) studies performed on the two configurations used to generate the data for the aerodynamic database.

### 2.1 Modification-III

The Modification-III (Mod-III) configuration replaces the P2006T wing with a new, high-aspect-ratio wing designed to minimize drag at cruise conditions (refs. 6-7). A comparison between the P2006T wing and Mod-III wing reference quantities is shown in table 1.

Table 1. Wing reference quantities.

Reference Parameter	Tecnam P2006T (Mod-II)	Mod-III/IV
$\bar{c}$ , ft	4.40	2.13
b, ft	37.40	31.62
S, ft <sup>2</sup>	158.88	66.67
AR	8.81	15.0
Wing loading, lb/ft <sup>2</sup>	13.40	45.0
Cruise, $C_L$	0.275	0.75

The Mod-III wing uses a custom designed airfoil to achieve a design cruise lift coefficient of  $C_L = 0.75$ . For comparison, the Tecnam P2006T cruise lift coefficient is  $C_L = 0.275$ . To help minimize the increase in induced drag resulting from the larger cruise lift coefficient for Mod-III, the aspect ratio (AR) of the Mod-III wing was increased to AR = 15 compared to an AR = 5.51 for the P2006T wing. In terms of planform, the Mod-III wing has a mean aerodynamic chord of  $\bar{c} = 2.13$  ft and a span of  $b = 31.6$  ft versus  $\bar{c} = 4.4$  ft and  $b = 37.4$  ft for the P2006T wing. Figure 5 shows an overlay comparing the planforms areas between the P2006T airplane and the X-57 airplane with the new, high-aspect-ratio wing. The planform area of the Mod-III wing is approximately 42 percent of the P2006T planform area. For the Mod-III configuration, the cruise motors have been placed in the nacelles located at the wingtips. Each cruise motor propellor spins opposite to the wingtip vortex to further reduce induced drag at cruise. Analytical predictions early in the design cycle of the Mod-III configuration suggest that the wingtip-mounted propellor could reduce the induced drag by 10 percent (ref. 3). Distributed along the leading edge of the Mod-III wing are 12 high-lift propulsors powered by electric motors and housed in the nacelles along the wing; however, they remain unpowered with the propeller blades folded flush with the nacelle surface for Mod-III operations.

### 2.2 Modification-IV

The Modification-IV (Mod-IV) configuration uses the same wing as Mod-III, but with the 12 high-lift electric propulsors powered for low-speed flight. Figure 6 provides an illustration of a high-lift motor and relevant details related to the motor design. The motors are powered by the aircraft traction power system. This system is separated into two parts: traction battery A and traction battery B. Each traction battery is

connected to a pallet that contains electrical contactors that direct power to the high-lift propulsors. The power distribution system was designed to prevent a complete failure of all the high-lift propulsors on one side of the airplane. Contactor pallets A and B, illustrated in fig. 7, contain electrical contactors which direct power to three high-lift motors on each side of the wing. A single electrical contactor failure will result in an asymmetric condition, where three high-lift motors on one half of the wing will become inactive, depending on which contactor fails.

The high-lift propulsors are used for low-speed operations below 110 kn calibrated airspeed (KCAS) to recover the stall speed of the P2006T airplane that was adjusted for the higher gross weight of Mod-IV (3,000 lb) compared to the P2006T gross weight (2,712 lb). At the 3,000-lb design weight for Mod-IV, the weight-adjusted stall speed goal is 58 KCAS compared to 55 KCAS for the P2006T. The high-lift motors are independently controlled by motor controllers that schedule motor torque and RPM as a function of pressure altitude and equivalent airspeed. Under nominal operation, referred to as the airspeed mode, the high-lift motor controllers compute propeller RPM using air data measurements from a National Advisory Committee for Aeronautics (NACA)-style nose boom on the nose of the X-57 airplane. The high-lift system propeller blades are retracted and flush against the motor nacelle during cruise operations with the high-lift system inactive to minimize drag. During landing operations, the pilot will activate the high-lift system at an airspeed of approximately 110 kn indicated airspeed (KIAS). The high-lift motors will then spin up to the commanded RPM based on pressure altitude and kn equivalent airspeed (KEAS) measurements derived from the nose boom. The centripetal acceleration, due to motor spin-up, forces the high-lift propellers to deploy from their retracted position when the high-lift motors are not spinning. As the airplane slows down, the high-lift motor torque increases linearly with airspeed to a maximum torque of 16.2 ft-lb at an airspeed of 58 KEAS. A generalized diagram of the high-lift motor torque schedule is shown in fig. 8. More details on the design, operation, and scheduling of the high-lift motors can be found in ref. 3 and refs. 8-11.

### **3 Database Sources**

Early on in the project, two wind-tunnel tests of a 19-percent scale model of the Mod-III configuration were conducted using the NASA Langley Research Center (LaRC) 12-ft wind tunnel. These tests were focused on steady-state aerodynamic and dynamic derivative estimates used for aerodynamic modeling of Mod-III. Flap deflections were not included in these tests because the slotted flaps could not appropriately be modeled at this small of a scale and Reynolds number (approximately 19 percent scale and  $Re_c = 150,000$ ). The steady-state data from these wind-tunnel tests were not included in the final aero database for several reasons including the inability to model flap deflections, evolving changes to the outer mold line that occurred after the wind-tunnel tests, and the need to model the aerodynamic-propulsive effects of the cruise and high-lift motors, which couldn't be modeled in the 12-ft tunnel.

The X-57 aerodynamic database described in this report was created from over 2,500 CFD cases run on the Mod-III and Mod-IV configurations. Several aircraft configurations were analyzed computationally for the aero database, including Mod-III with and without cruise motor power, Mod-IV high-lift power for nominal and contactor failure cases, and ground effects for both Mod-III and Mod-IV. Forced oscillation CFD cases were used for dynamic derivative estimation for cruise power off and with high-lift power on. For most of the configurations studied, CFD simulations were run with control surfaces both neutral and then deflected over their full operating range. Angle-of-attack and angle-of-sideslip sweeps were conducted with control surfaces neutral. The aerodynamic data shown in this report will focus exclusively on the CFD results except for the dynamic derivative results, where wind-tunnel data is shown for comparison due to the complexity of modeling dynamic derivatives in CFD.

#### **3.1 Computational Fluid Dynamics Solver Descriptions**

Four different Computational Fluid Dynamics (CFD) solvers were used during the effort with participation from three different NASA Centers: AFRC, the Ames Research Center (ARC), and LaRC. The STAR-CCM+® (Siemens Digital Industries, Plano, Texas) solver (ref. 12) was the primary Navier

Stokes CFD solver used by the AFRC. The Launch, Ascent, and Vehicle Aerodynamics (LAVA) Navier Stokes CFD solver (ref. 13) was the primary solver used by the ARC. The LaRC initially started the effort using the LaRC-developed USM3D (ref. 14) Navier Stokes CFD solver and relied heavily on that solver for the Mod-III configuration, but then, switched over to the CREATE™-AV Kestrel (refs. 15-16) Navier Stokes CFD solver for Mod-IV. All CFD runs were modeled as fully turbulent Reynolds-averaged Navier-Stokes (RANS) using the Spallart-Allmaras (SA) turbulence model (ref. 17). All solvers except USM3D also implemented the Rotation Curvature (RC) (ref. 18) and Quadratic Constitutive Relation (QCR2000) (ref. 19) correction to the standard SA model. The USM3D solver used the QCR2000 correction only. The actuator disk approach was used by all solvers to model the cruise and high-lift propeller flow for the power-on cases. This approach allowed efficient modeling of the propeller effects on the airplane and wing aerodynamics by approximating the volume of the propeller disk as a source of additional flow momentum and energy without modeling the individual blades dynamically rotating, which would be very expensive computationally.

The general approach for running CFD cases was to utilize all the solvers for angle-of-attack sweeps looking at longitudinal aerodynamics. Beta sweeps at constant angle of attack were primarily run with STAR-CCM+® and LAVA solvers, with some spot checks from USM3D and/or Kestrel depending on the configuration. Control surface deflections were assigned with one solver being primary and the others used for spot checks. The primary solver used for stabilator sweeps was STAR-CCM+®, and LAVA was the primary solver used for aileron and rudder sweeps. The following sections describe each solver in more detail.

### 3.1.1 STAR-CCM+®

The STAR-CCM+® solver is a commercially available comprehensive CFD package consisting of computer aided design (CAD) solid modeling and surfacing preprocessing tools, high-quality mesher capable of generating various unstructured grid topologies using polyhedral, trimmer (cartesian), and tetrahedral cells with prism layers, various steady and unsteady flow solvers, and CFD solution postprocessing, and flow visualization tools. All the tools within STAR-CCM+® are tightly integrated, resulting in efficient workflow for producing high-quality CFD meshes and solutions.

The coupled compressible Reynolds-averaged Navier-Stokes solver in finite-volume, cell-centered formulation was utilized for both steady and unsteady simulations in this project. The second-order Roe flux-difference splitting scheme along with the Hybrid Gauss Least-Square Reconstruction method and the Venkatakrishnan limiter was used to discretize the convective terms. The algebraic multigrid linear solver using the Gauss-Seidel relaxation scheme was utilized to solve the system of linearized equations. Flow was assumed fully turbulent using the Spalart-Allmaras one-equation turbulence model with rotation correction. Quadratic constitutive relationship was only included on Mod-IV simulations. The Courant-Friedrichs-Lewy (CFL) number was linearly ramped from 0.01 to 25.0 within the first 100 iterations. All simulations were performed using a uniform freestream condition as the initial condition, without a low-Mach preconditioner. A half-span model was used when aircraft configuration and freestream conditions were symmetrical. The unsteady simulations, used to compute the dynamic derivatives, were performed by rotating the entire grid system in the direction associated with the dynamic derivatives about the moment reference center. The number of subiterations ensured that residual of the pseudo time step dropped at least two orders of magnitude.

Body-force actuator disks were used to model the high-lift propellers and wingtip cruise propellers. Thrust and torque distribution of the wingtip cruise propellers were modeled using the Goldstein distribution, which was included in STAR-CCM+®. The thrust and torque distribution of the high-lift propellers were computed using Blade Element Momentum (BEM) theory, and the results were fed into STAR-CCM+® in a tabulated form.

The computational mesh was created using the polyhedral topology combined with the prism layer mesh. The far field was specified to be 50 span lengths away from the airplane. The wall spacing was specified such that the  $y^+$  value would be less than 0.333. The prism layer mesh contained 31 layers and the total height was specified based on the turbulent boundary layer thickness, then adjusted based on

preliminary solutions. Cell size of individual components of the aircraft (fuselage, vertical tail, rudder, stabilator, and wing) were specified as a percentage of a reference length variable to simplify the process of systematically creating meshes of different resolution. Volumetric refinement zones were added in the power-on simulations to capture the physics added by the propellers. The overall grid quality was high, based on the metrics of the STAR-CCM+<sup>®</sup> grid diagnostic tool, with the face validity being above 0.95 for 99.9 percent of the cells.

The convergence criteria of the steady simulations were based on the standard deviation of the forces and moments as well as the trend of the residuals. The simulation was considered converged if the standard deviation of all relevant forces and moments were less than  $1e-4$  for the final 2,000 iterations, and the residual forces and moments showed asymptotic behavior. For the unsteady simulations, a simulation was considered converged if the time history of the relevant forces and moments showed repeated periodic behavior for more than three cycles.

### **3.1.2 Launch Ascent and Vehicle Aerodynamics**

The structured curvilinear flow solver within the Launch Ascent and Vehicle Aerodynamics (LAVA) solver framework was used for the database generation process. Two versions of the LAVA curvilinear solver were used: the legacy solver, and the refactorization version, which has a 9- to 12-times faster run time compared to the legacy solver. The compressible RANS equations in strong conservation law form are discretized using a finite difference formulation, and the Spalart-Allmaras turbulence model using the RC and QCR2000 corrections to close the RANS system of equations. A second-order modified Roe convective flux discretization scheme (refs. 20-21) was used with third-order left and right state reconstruction. For database cases computed using the earlier version of the solver, the linearized system of equations was solved at each nonlinear iteration using an Alternating Line Jacobi method, whereas the refactored version utilizes a preconditioned Generalized Minimal Residual Method (GMRES) solver (ref. 22). For all steady simulations, the nonlinear equations are marched in pseudo time to the final steady-state solution, whereas for unsteady calculations, the physical time derivative terms are included in the calculation and discretized using a second-order backward differencing formula. The far-field domain boundaries are set using a Riemann-invariant far-field boundary condition placed 1,000 body lengths away from the aircraft, and the calculation is initialized using freestream conditions. For time-dependent dynamic moving body simulations, used to predict stability derivatives of the airplane, the entire grid system, including the aircraft surfaces, were rotated using a prescribed pitching, rolling, or yawing motion. Time-varying volume preserving metric terms are used to ensure preservation of the geometric conservation law, which is required to get second-order accuracy.

All computations were performed on body-fitted structured curvilinear overset grids. Accommodations were made for mesh updates, which were required for geometric configuration changes such as control surface deflections. All structured grids follow best-practice methodologies with respect to stretching ratio, wall spacing, and grid quality metrics, as outlined in ref. 23. Structured surface patches were constructed using a combination of Pointwise (ref. 24) and Chimera Grids Tools (CGT) (ref. 25) software packages, whereas volume zones were generated by hyperbolically marching surface domains away from the wall boundaries using CGT. Off-body Cartesian zones were also generated around each major airplane component to serve as an interface between body-fitted volumetric zones and the far-field Cartesian zone that stretches to the far-field domain boundaries. Following preliminary grid sensitivity studies, the grid systems that would be used for all database work would target an average  $y^+$  of approximately 0.8 for all cases, a maximum stretching ratio of 1.16 in all curvilinear coordinate directions, and an average of approximately 130 million points (ref. 26).

Convergence criteria used for steady-state simulations was derived from the standards used for various high-lift prediction workshop studies (refs. 27-28). These criteria include targeting a standard deviation in the integrated drag coefficient below  $10e^{-5}$ , as measured sufficiently across many nonlinear iterations, with no discernable upward or downward trend in any aerodynamic coefficients. The aerodynamic coefficients were then averaged over many nonlinear iterations, using averaging windows large enough to capture multiple cycles of the lowest frequency fluctuations. While some cases were

unable to achieve this standard deviation requirement, all cases were run until load fluctuations in nonlinear iteration space were deemed statistically stationary. To confirm the lack of an upward or downward trend, various averaging windows were tested for selected cases to ensure the reported aerodynamic loads and moments would remain essentially unchanged. For the unsteady moving body simulations, dual time stepping is utilized, and at least two orders-of-magnitude convergence during the subiteration procedure is achieved before starting the next time step. These simulations are run for four to eight cycles of forced motion until the predicted forces and moments achieve a time-periodic behavior.

### **3.1.3 USM3D**

The USM3D CFD solver developed at LaRC is a cell-centered, finite volume Euler and Navier-Stokes method. Each solution was computed with a global time stepping, time-accurate RANS method until convergence or solution periodicity was achieved. The time-stepping scheme used was the implicit Gauss-Seidel method, and the spatial differencing scheme of Euler fluxes was the Roe flux difference-splitting scheme. The Newton method (3-point backward differencing without pseudo time and up to 15 subiterations) was used for the time-accurate scheme. The solver was run in first-order spatial accuracy until the residual dropped two orders of magnitude, at which point the solver automatically switched to generate second-order, spatially-accurate solutions. The RC correction was not used with USM3D. Further details and USM3D results of the Mod-III configuration are found in ref. 29.

The legacy USM3D solver requires a tetrahedral, unstructured mesh. The mesh is initially created with prism layers in the boundary layer, then each prism is subdivided into three anisotropic tetrahedral cells to satisfy the USM3D solver while mimicking the benefit of prism layers in the boundary layer. This gridding approach works well to match results with solvers using mixed-element unstructured meshes. A semi-span mesh was used with cases involving symmetric flow conditions and geometric settings. A full-span mesh was used with cases involving asymmetric power, sideslip conditions, and control surface deflections. For cases with power, the legacy USM3D solver required actual patches in the grid and in the location of the actual-sized propeller to be modeled. The actuator disk model for each propeller required an inflow and an outflow patch that reside in the same location.

USM3D has two options for implementing actuator disks for modeling propellers: either uniform loading, or a user-specified thrust distribution. The actuator disk model for USM3D requires nine values for each propeller: the rotor outer radius; the x-, y- and z-coordinate of the location of the rotor center; a normalized advance ratio; a normalized thrust coefficient; a normalized torque coefficient; the rotational direction; and the type of rotor condition.

For steady problems, two main criteria were used to determine solution convergence: a drop in residual of two orders of magnitude, and the convergence of force and moment coefficients to less than 0.5 percent change over a specified range of iterations. The coefficients were averaged over the specified range of iterations and the standard deviation and percent over range (POR) was calculated. The POR is computed with the difference in the coefficient at the beginning and end of the range, normalized by the average, and multiplied by 100. Steady solutions were deemed converged when the POR of each aerodynamic coefficient was less than 0.5. For unsteady problems, a drop in residuals of two orders of magnitude was preferable, and periodicity in the force and moment coefficients was needed to compute a reasonable average of the coefficients. In some situations, unsteady flows with large regions of flow separation prevented large or smooth decreases in the solution residuals, and engineering judgement was used to determine convergence.

### **3.1.4 Kestrel**

The Kestrel CFD solver (refs. 30-31) was developed by the Department of Defense Computational Research and Engineering Acquisition Tools and Environment (CREATE™-AV) group. The time-stepping scheme used was the implicit Gauss-Seidel method, and the inviscid flux scheme was HLLE++. Each solution was computed with a global time stepping, time-accurate RANS method until convergence or solution periodicity was achieved. Fully turbulent solutions were computed with the SA turbulence model. At the start of this work, only the RC option to the SA turbulence model was available in Kestrel.

Later, however, the QCR2000 option also became available such that solutions were computed with SA QCR2000 for comparisons with USM3D results and SA RC QCR2000 for comparisons with LAVA and STAR-CCM+®.

A mixed-element, unstructured mesh with prisms in the boundary layer and tetrahedral in the far field was used with the Kestrel solver. A semi-span mesh was used with cases involving symmetric flow conditions and symmetric geometric settings. A full-span mesh was used with cases involving asymmetric power, sideslip conditions, and control surface deflections. For cases with power, the version of the Kestrel solver used for this work required actual patches in the grid and in the location of an actual-sized propeller to be modeled. The actuator disk model for each propeller required an inflow and an outflow patch that reside in the same location.

Kestrel has two options for implementing actuator disks for modeling propellers: either uniform loading or a triangular thrust distribution. The triangular thrust distribution option was used to match the thrust distributions of the high-lift propellers more closely; however, this option wasn't appropriate to match the thrust distribution of the cruise propellers. The inputs for the boundary condition include the RPM, the thrust vector direction, thrust, and the location of the maximum thrust along the radius. Since the grids were made with positive x in the flow direction, the thrust vector for the high-lift propellers was specified as -1, 0, 0. To specify the rotation of the propeller, a positive RPM is used when the rotation gives a right-hand rule vector in the direction of the thrust vector and a negative RPM when the rotation gives a right-hand rule vector in the opposite direction of the thrust vector.

For steady problems, two main criteria were used to determine solution convergence: a drop in residual of two orders of magnitude, and the convergence of force and moment coefficients to less than 0.5 percent change over a specified range of iterations. Steady solutions were deemed converged when the percent over the averaged range of each aerodynamic coefficient was less than 0.5. For unsteady problems, a drop in residuals of two orders of magnitude was preferable, and periodicity in the force and moment coefficients was needed to compute a reasonable average of the coefficients. In some situations, unsteady flows with large regions of flow separation prevented large or smooth decreases in the solution residuals, and engineering judgement was used to determine convergence.

## **4 Steady-State Computational Fluid Dynamics Results**

Over 2,500 different Computational Fluid Dynamics (CFD) cases were run during the course of the study. Due to the sheer number of cases that were run for this effort, the results of every case that was analyzed will not be presented in the text of this report. Furthermore, each subset of CFD results presented in the following sections of this report will not be analyzed in great detail; however, general takeaways from the results, and some of the more important or interesting results will be discussed.

The CFD effort started with the simplest configuration, Mod-III (with no propulsors), then progressed in complexity by adding on cruise propulsors, and then looking at ground effects for the unpowered Mod-III aircraft. The analysis work then moved on to the Mod-IV configuration for both nominal and several failure scenario cases, and then ground effect with the high-lift system operating. After the steady-state portion of the aerodynamic database had been completed, the team worked on forced oscillation CFD cases for dynamic derivative estimation.

The X-57 simulation uses a conventional body-fixed coordinate system, as shown in fig. 9. In this system, the origin is located at the center of gravity of the aircraft, and the x-axis is positive, forward out the nose; the y-axis is positive, out the right wing; and the z-axis is positive, down. The CFD results were reported in stability axes for lift and drag coefficients and aircraft body axes for side force and all three moment coefficients. Positive aileron and stabilator deflections were defined as trailing-edge down, and positive rudder deflection is trailing-edge left. The control surface sign conventions and deflection ranges are given in fig. 9.

#### 4.1 Modification-III Power Off

An initial set of CFD cases was chosen to simulate the Modification III (Mod-III) aircraft with no cruise motor propulsors. Cases were run for three different flap settings: 0, 10, and 30 deg deflections representing cruise, takeoff, and landing configurations, respectively. Speed and altitude for the CFD runs were chosen based on the flap setting with the flaps retracted (0 deg) representing high-speed cruise, landing flaps (30 deg) representing a speed near an estimated  $1.2 V_{S0}$ , and takeoff flaps (10 deg) representing speeds near an estimated  $1.2 V_{S1}$ , as shown in table 2.

Table 2. Modification III (power off) Computational Fluid Dynamics conditions.

Configuration	Altitude, ft	Mach	KCAS	Flaps, deg
Landing	2,500	0.139	88	30
Takeoff	2,500	0.149	94	10
Cruise	8,000	0.233	133	0

Each flap setting included an angle-of-attack sweep, a single-sided beta sweep at various angles of attack, and control surface sweeps at various angles of attack, as shown in tables 3 and 4.

Table 3. Modification-III (power off) angle-of-attack and angle-of-sideslip Computational Fluid Dynamics simulation ranges (all flap settings unless otherwise noted).

Alpha (deg)	Beta (deg)
-2	0
0	0
2	0
4	0
8	0
10	0
12	0
14	0
15	0
16	0
17	0
18	0
19	0
20	0
22	0
2	5, 10, 15, 20
8	5, 10, 15, 20
12	5, 10, 15, 20
*16, 15, 14	5, 10, 15, 20

\* 16 deg for flaps 0 deg; 15 deg for flaps 10 deg; and 14 deg for flaps 30 deg.

Table 4. Modification III (power off) control surface deflection Computational Fluid Dynamics simulation ranges (all flap settings unless otherwise noted).

Alpha, deg	Beta, deg	Stab, deg	Aileron, deg	Rudder, deg
2	0	-5, 5, -15, -12, -15	0	0
8				
*16, 15, 14				
2	5	-5, -12		
2	0	0	-25, -15, -10, -5, 5, 10, 18	0
8				
*16, 15, 14				
2	-5,5		-25, -15, 10, 18	
2	0	0	0	-5, -10, -18, -28
8				
*16, 15, 14				
2	-5,5			

\* 16 deg for flaps at 0 deg; 15 deg for flaps at 10 deg; and 14 deg for flaps at 30 deg.

Additional test conditions were run, as needed, if there were discrepancies between the various solvers. All four of the CFD solvers were used for the Mod-III power-off analysis, but not all four solvers ran every single case.

#### 4.1.1 Longitudinal Results

Lift, drag, and pitching moment coefficient were computed for the three different flap settings. The coefficients are defined according to eqs. (1)-(3), below.

$$C_L = \frac{L}{\bar{q}S} \quad (1)$$

$$C_D = \frac{D}{\bar{q}S} \quad (2)$$

$$C_m = \frac{M_y}{\bar{q}S\bar{c}} \quad (3)$$

Figures 10-12 show the CFD results for  $C_L$ ,  $C_D$ , and  $C_m$  as a function of angle of attack. The solvers predicted a  $C_{L_{max}} = 2.1$ -2.3 for flaps at 0 deg. Landing flaps (30 deg) increased the maximum lift coefficient by about 31 percent to  $C_{L_{max}} = 2.75$ -3.03. Both STAR-CCM+® and LAVA tend to have higher estimates of  $C_{L_{max}}$  than Kestrel and USM3D. The Kestrel and USM3D solutions also tend to have  $C_{L_{max}}$  occur at a lower angle of attack than STAR-CCM+® and LAVA. The drag coefficient  $C_D$  results show good agreement between the various solvers for the different flaps settings and  $C_D$  increases with flap settings, as expected. Pitching moment has a negative slope indicating positive static stability in the pitch axis.

#### 4.1.2 Lateral-Directional Results

Most of the lateral-directional cases were run using STAR-CCM+® and LAVA, with some limited runs from USM3D to spot check the solutions from the other two solvers. Side force, rolling moment coefficient, and yawing moment coefficient were computed for the three different flap settings. The

maximum angle of attack simulated in CFD decreased between flaps 0, 10, and 30 deg to avoid the stall angle-of-attack region for the particular flap deflection. The lateral-directional coefficients are defined according to eqs. (4)-(6), below.

$$C_Y = \frac{F_Y}{\bar{q}S} \quad (4)$$

$$C_l = \frac{M_x}{\bar{q}Sb} \quad (5)$$

$$C_n = \frac{M_z}{\bar{q}Sb} \quad (6)$$

Figures 13-15 show the results for side force coefficient  $C_Y$  as a function of sideslip angle for the various flap settings and at different angles of attack. As expected,  $C_Y$  has a negative slope when plotted as a function of sideslip. In general, there is good agreement between the solvers with some small deviations at higher angles of attack and sideslip. Figures 16-18 show the results for rolling moment coefficient  $C_l$ . The negative slope of the plots demonstrates positive roll stability. For flaps 0 and 10 deg, shown in figs. 16 and 17, there is a decrease in the slope magnitude at 12 deg angle of attack as the sideslip angle increases beyond 5 deg, which would indicate a reduction in roll stability; however, that same behavior is not present at angles of attack of 16 and 15 deg for flaps 0 and 10 deg, respectively. For flaps 30 deg,  $C_l$  is linear with sideslip angle for all sideslip angles only at an angle of attack of 2 deg. Figures 19-21 show the results for yawing moment coefficient  $C_n$ . The slope of the data is positive with sideslip angle indicating positive directional stability. At the highest simulated angle of attack for all flap settings, the initial slope, between 0 and 5 deg sideslip, is generally quite flat, particularly for STAR-CCM+<sup>®</sup>, with a noticeable increase in slope as the sideslip angle increases beyond 5 deg.

#### 4.1.3 Control Surface Deflection Results

The X-57 airplane has an all-moving horizontal stabilator for pitch control, ailerons for roll control, and a rudder for yaw control. Force and moment coefficients due to the control surface deflections were estimated from CFD for the full-deflection ranges of each control surface. The control surface deflection ranges that were simulated are shown in table 4.

Aileron deflections were modeled as single sided with only the right aileron being deflected because the results for the left aileron can be assumed to be antisymmetric to those obtained for the right aileron. This practice is a somewhat standard in CFD or wind-tunnel testing of aircraft. Rudder deflections were modeled in the negative direction only due to the airplane symmetry. To split up the work amongst the CFD solvers, one solver was typically used as the primary solver for a particular control surface, and the other solvers were used for spot checks of the results. The STAR-CCM+<sup>®</sup> solver was used as the primary solver for the stabilator deflections, and LAVA was the primary solver for aileron and rudder deflection.

Figure 22 shows pitching moment  $C_m$  due to stabilator deflection for a range of angle of attack and for all three flap settings. As expected, the slopes of the curves are negative, which agrees with the deflection definition in fig. 9, where a positive deflection produces a negative moment. The agreement between STAR-CCM+<sup>®</sup> and LAVA is very good, and  $C_m$  is essentially linear with stabilator deflection for all cases simulated.

Figures 23 and 24 show rolling and yawing moment coefficients  $C_l$  and  $C_n$  due to aileron deflection. The rolling moment coefficient has a negative slope and is essentially linear in the range of aileron deflection of -25 to 5 deg, with a reduction in slope for aileron deflections greater than 5 deg. An interesting behavior happens at flaps 10 deg, at an angle of attack of 15 deg (middle plot in fig. 23). The aileron loses effectiveness at aileron deflections lower than negative 10 deg; however, that same

phenomenon does not continue at flaps 0 or 30 deg, indicating a potential sensitivity at 15 deg angle of attack at flaps 10 deg. Figure 24 shows that  $C_n$  has somewhat of a parabolic behavior with aileron deflection with the yawing moment coefficient increasing from 0 as the aileron deflects in both positive and negative directions. Given that only the right aileron was deflected in these simulations, both a positive and negative aileron deflection should increase the drag on the right wing for larger aileron deflections, which generally results in a positive yawing moment, as shown in the plots in fig. 24.

Figures 25 and 26 show rolling and yawing moment coefficients  $C_l$  and  $C_n$  due to rudder deflection. Negative deflection of the rudder produces a force in the negative y-direction on the vertical tail. Because the aerodynamic center of the vertical tail is above the airplane z-axis center of gravity, the force on the tail due to negative rudder deflection is expected to produce a negative rolling moment, which agrees with the results shown in fig. 25. For flaps 10 deg, at an angle of attack of 15 deg, there is an abrupt change in rolling moment between negative 10 and negative 18 deg rudder deflection, but the overall magnitudes of the rolling moment are very small. Yawing moment due to rudder deflection is linear for all conditions tested, as shown in fig. 26, with good agreement between both LAVA and STAR-CCM+®.

## 4.2 Modification-III Cruise Motor Effects

As mentioned in Section 2.1, the electric cruise motors are located at the wingtips of the new high-aspect-ratio wing used for the Mod-III/IV configurations. The motors were moved to the wingtips, as opposed to being located further inboard like they are on the P2006T wing, to reduce the induced drag by having the propellers rotating counter to the wingtip vortices. A portion of the propeller slipstream affects the flow on the outboard section of the wing, resulting in small increments to the overall airplane  $C_D$ ,  $C_L$ , and  $C_m$ . In order to capture the aero-propulsive effects of the cruise motors, CFD simulations of Mod-III (with the cruise propulsors) were run using the STAR-CCM+®, LAVA, and USM3D solvers. Table 5 shows the conditions that were simulated in CFD for the cruise motor analysis.

Table 5. Cruise motor Computational Fluid Dynamics conditions.

Hp, ft	KCAS	V, ft/s	$\rho$ , slug/ft <sup>3</sup>	RPM	J	$\beta_p$ , deg	$C_T$	$C_T$	$C_Q$
2,500	42.8	75	0.002208	2,250	0.4	14	0.0989	0.0608	0.0097
						18	0.1371	0.0911	0.0145
						22	0.1673	0.1219	0.0194
						26	0.1857	0.1487	0.0237
2,500	64.3	112.5	0.002208	2,250	0.6	14	0.0539	0.0421	0.0067
						18	0.1001	0.0788	0.0125
						22	0.1422	0.1195	0.0190
						26	0.1744	0.1579	0.0251
2,500	85.7	150	0.002208	2,250	0.8	14	-0.0004	0.0074	0.0012
						18	0.0499	0.0486	0.0077
						22	0.1003	0.0979	0.0156
						26	0.1466	0.1514	0.0241
8,000	98.6	187.5	0.001868	2,250	1.0	18	-0.0064	0.0014	0.0002
						22	0.0479	0.0563	0.0090
						26	0.1021	0.1201	0.0191
						30	0.1522	0.1884	0.0300
8,000	118.4	225	0.001868	2,250	1.2	22	-0.0085	-0.0021	-0.0003
						26	0.0498	0.0686	0.0109
						30	0.1075	0.1490	0.0237
8,000	128.2	243.75	0.001868	2,250	1.3	22	-0.0366	-0.0365	-0.0058
						26	0.0223	0.0364	0.0058
						30	0.0826	0.1215	0.0193
						34	0.1401	0.2142	0.0341
15,000	123.8	262.5	0.001496	2,250	1.4	26	-0.0057	0.0003	0.0001
						30	0.0567	0.0896	0.0143
						34	0.1177	0.1889	0.0301
15,000	125.8	266.67	0.001496	2,000	1.6	30	0.0030	0.0134	0.0021
						34	0.0694	0.1242	0.0198
						38	0.1341	0.2482	0.0395
15,000	141.6	300	0.001496	2,000	1.8	30	-0.0504	-0.0756	-0.0120
						34	0.0183	0.0425	0.0068
						38	0.0897	0.1816	0.0289
						40	0.1234	0.2537	0.0404

The cruise motor propellers were modeled in CFD using actuator disks, with thrust and torque coefficient data estimated using a blade element momentum (BEM) model of the propellers. Equations (7)-(10) show how the advance ratio, thrust, power, and torque coefficients were calculated. The advance ratio in the CFD simulations was varied from  $J = 0.4$  to  $1.8$ . This range fully encompasses the range of advance ratios expected in flight, which is closer to  $J = 0.7$  to  $1.5$ . The CFD simulations were run with blade pitch values  $\beta_p = 14$ - $40$  deg, which encompasses the range of blade pitch conditions that might be

encountered over the flight envelope with the cruise motors set between idle and peak power. For a given advance ratio, a sweep of four different blade pitch values was simulated, as shown in table 5. Propeller thrust, power, and torque coefficients were computed for the propeller actuator disks and were used as inputs in the CFD simulations.

$$J = \frac{V}{\left(\frac{RPM}{60} d\right)} \quad (7)$$

$$C_T = \frac{T}{\left(\rho \left(\frac{RPM}{60}\right)^2 d^4\right)} \quad (8)$$

$$C_P = \frac{P}{\left(\rho \left(\frac{RPM}{60}\right)^3 d^5\right)} \quad (9)$$

$$C_Q = \frac{Q}{\left(\rho \left(\frac{RPM}{60}\right)^2 d^5\right)} = \frac{C_P}{2\pi} \quad (10)$$

Figures 27-29 show deltas  $\Delta C_D$ ,  $\Delta C_L$ , and  $\Delta C_m$  due to the cruise propeller operation as a function of advance ratio and blade pitch angle. The delta for each coefficient is defined, as shown in eq. 11, below.

$$\Delta Coefficient = C_{Power\ on} - C_{Power\ off} \quad (11)$$

The operation of the cruise motor was predicted to produce a small decrease in drag coefficient that is stronger ( $\Delta C_D$  more negative) as the advance ratio decreases due to spinning the propellers counter to the wingtip vortices. At the Mod-III design cruise condition of 150 KTAS at 8,000 ft pressure altitude, the advance ratio, based on an RPM of 2,250, would be approximately  $J = 1.35$ , and the blade pitch is estimated to be approximately  $\beta_p = 30$  deg. Figure 27 shows the change in drag coefficient at those conditions is approximately  $\Delta C_D = -0.0014$ . The CFD simulations only included one cruise motor, so the total drag coefficient reduction in flight, at the cruise condition with both cruise motors operating, is predicted to be about two times that value or  $\Delta C_D = -0.0028$ . This reduction in drag is estimated to be about 4.8 percent of the total aircraft drag without cruise motor effects at that flight condition, assuming a gross weight of 3,000 lb.

As expected, due to the accelerated flow over the outboard portion of the wing, the cruise motor produces a small increase in lift as shown in fig. 28. For the advance ratio range expected in flight of  $J = 0.7$  to  $1.5$ , the increase in lift coefficient is on the order of  $\Delta C_L = 0-0.05$  for one motor. Cruise motor operation also results in a small decrease in pitching moment (nose down) in the range of  $\Delta C_m = -0.03$  to  $0$  for advance ratios  $J = 0.7$  to  $1.5$ , as shown in fig. 29.

### 4.3 Modification-IV High-lift System

The bulk of the CFD effort for the X-57 aerodynamic database was modeling the aero-propulsive effects of the 12 high-lift motors distributed along the leading edge of the wing for the Mod-IV configuration. Similar to the cruise motors, the high-lift propulsors were modeled in CFD as actuator disks with thrust, torque, and power coefficient data obtained from a BEM model of the high-lift propellers. The bulk of the CFD cases covered the nominal operation of the high-lift system with all 12 high-lift motors operating at the same RPM, which was derived from two-dimensional look-up tables that are a function of pressure altitude and equivalent airspeed. Additional cases simulating individual failures

of both the A and B traction system electrical contactors were run to investigate how high-lift system failures would affect the aircraft aerodynamics.

#### 4.3.1 Nominal Operation

The nominal concept of operations for the high-lift system is for all 12 of the motors to be operating at the same RPM. The CFD simulations were run at seven different airspeeds in the high-lift motor operating schedule. Table 6 shows the actuator disk settings used for the high-lift propulsors, at the different airspeeds.

Table 6. High-lift Propeller Nominal Operation Actuator Disk Settings.

Hp, ft	KCAS	V, ft/s	$\rho$ , slug/ft <sup>3</sup>	RPM	J	$C_T$	$C_P$	$C_Q$	T, lbf	P, kW	Q, lbf-ft
2,500	35	61.3	0.002208	3545	0.5490	0.3125	0.3134	0.0499	30.7	4.7	9.3
2,500	50	87.6	0.002208	4661	0.5966	0.3058	0.3152	0.0502	52.0	10.7	16.1
2,500	58	101.6	0.002208	4702	0.6860	0.2848	0.3075	0.0489	49.3	10.7	16.0
2,500	65	113.8	0.002208	4379	0.8250	0.2473	0.2874	0.0457	37.1	8.1	13.0
2,500	75	131.3	0.002208	3962	1.0521	0.1788	0.2367	0.0377	22.0	4.9	8.7
2,500	90	157.6	0.002208	3428	1.4595	0.0366	0.0809	0.0129	3.4	1.1	2.2
2,500	100	175	0.002208	3451	1.6098	-0.0198	0.0018	0.0003	-1.8	0.0	0.0

At speeds of 58, 75, and 90 KCAS, a full set of CFD cases, equivalent to what was run for the Mod-III power-off configuration, were completed for both landing and takeoff flaps settings (flaps 30 and 10 deg). At the four other speeds of 35, 50, 65, and 110 KCAS, a subset of cases was run to reduce the total number of cases analyzed. The following sections will concentrate on the CFD results for high-lift motor power settings of 10.7 kW, 8.1 kW, and 4.9 kW, which correspond to airspeeds of 58, 65, and 75 KCAS, respectively, at a pressure altitude of 2,500 ft.

##### 4.3.1.1 Longitudinal Results

As mentioned in Section 2.2, the design goal for the high-lift system is a maximum lift coefficient  $C_{L_{max}} \geq 3.95$ . This lift coefficient is required to achieve a stall speed of 58 KCAS for the Mod-IV configuration at 3,000 lb. The 58 KCAS stall speed is the equivalent stall speed for the P2006T airplane, adjusted to the heavier gross weight of the Mod-IV configuration. Figure 30 shows the CFD-predicted lift coefficient at flaps 30 deg for a high-lift motor setting of 10.7 kW for the various solvers. The maximum lift coefficient ranged from  $C_{L_{max}} = 4.4$ -4.58, which provides a lift margin of between 11 to 16 percent over the goal of  $C_{L_{max}} \geq 3.95$ . It's important to note that these simulations were run with the horizontal tail at a neutral setting (0 deg deflection); therefore, at most angles of attack, the horizontal tail provides a small contribution to the total aircraft lift coefficient, as shown in fig. 30. This additional lift would not be present in trimmed flight, where some negative stabilator deflection is needed to provide a nose up pitching moment to counter the negative wing-body pitching moment. Conversely, the thrust provided by the high-lift motors has a component in the lift direction that is proportional to the total thrust of the high-lift system and the sine of the angle of attack of the airplane. The component of thrust in the lift direction from the high-lift system effectively cancels out the loss in lift due to having a non-zero stabilator deflection; thus, making the results from fig. 30 a reasonable estimate of the maximum airplane lift coefficient.

The rest of the results presented for the high-lift system under nominal operation are presented as deltas to the force and moment coefficients, as opposed to the absolute values. The deltas for the high-lift system were defined, as shown in eq. (11). Figures 31-33 show the  $\Delta C_D$ ,  $\Delta C_L$ , and  $\Delta C_m$  due to the high-lift system for power settings of 10.7, 8.1, and 4.9 kW, respectively, for both flaps at 30 and 10 deg. The

change in drag coefficient at 10.7 kW is considerable and results in a total aircraft drag coefficient that is over two times the power-off drag for Mod-III. The additional drag produced by the high-lift system is beneficial, though, as it helps negate some of the thrust effects of the high-lift system and should conceivably make it easier for the airplane to achieve the proper glide slope during landing. In fig. 32, the increase in  $C_L$  at 10.7 kW is between  $\Delta C_L = 1-1.5$  which is approximately a 60% increase over Mod-III. The pitching moment increment due to the high-lift system, shown in fig. 33, is generally positive and is larger for landing flaps compared to takeoff flaps. Figure 33 shows an interesting trend in  $\Delta C_m$  for flaps at 30 deg at 10.7 kW. Below about 10 deg angle of attack,  $\Delta C_m$  is positive but takes a sudden downward trend going slightly negative at higher angles of attack. This behavior is not present for flaps at 10 deg.

#### 4.3.1.2 Lateral-Directional Results

Because the primary purpose of the high-lift system is to produce additional lift for low-speed operations using all 12 high-lift motors operating at the same power setting, the high-lift system wasn't expected to have significant effects on the lateral-directional aerodynamics of the aircraft under nominal operations. The CFD cases, however, were run at 5, 10, 15, and 20 deg of sideslip at 2, 8, and 12 deg angles of attack for both flaps at 10 and 30 deg to quantify any effects from the high-lift system on the lateral-directional aerodynamics. Similar to what was done for the power-off sideslip CFD cases, the highest angle of attack simulated was dependent on the flaps setting with 15 and 14 deg angle of attack used for flaps at 10 and 30 deg, respectively.

Figures 34-39 show the deltas to the lateral-directional force and moment coefficients for the Mod-IV configuration for high-lift power settings of 10.7 and 4.9 kW. The high-lift system results in a small negative  $\Delta C_Y$  that tends to increase in absolute magnitude with sideslip angle and be larger in magnitude for lower angles of attack, as shown in Figures 34 and 35. The results for angles of attack greater than 8 deg tend to show more scatter amongst the solvers and a lack of a defined trend suggesting a higher uncertainty in the results at higher angles of attack. Figures 36 and 37 shows the change in rolling moment  $\Delta C_l$  with sideslip. At an angle of attack of 2 deg, there is a negative  $\Delta C_l$  that slightly increases in magnitude with increasing sideslip. The CFD results for higher angles of attack show some significant discrepancies between solvers and no definitive trends making it hard to draw any general conclusions. The change in yawing moment  $\Delta C_n$  due to sideslip, shown in figures 38 and 39, is generally very small and, like the results for  $\Delta C_Y$  and  $\Delta C_l$ , shows more variation at higher angles of attack.

#### 4.3.1.3 Control Surface Results

The CFD simulations were run with the control surfaces deflected to investigate the effects of the high-lift system on the control surface effectiveness. As was done for Mod-III, the primary control surfaces were swept through their full deflection ranges for different angles of attack. STAR-CCM+<sup>®</sup> was the primary solver used for the stabilator deflection cases and LAVA was the primary solver used for the aileron and rudder cases.

Figure 40 shows  $\Delta C_m$  versus stabilator deflection for two different power settings at angles of attack of 2, 8, and 15 deg for flaps at 10 deg and angles of attack of 2, 8, and 14 deg for flaps at 30 deg. In general, at higher power settings and lower angles of attack the high-lift system provides a positive increase in pitching moment for a given stabilator setting. There is an interesting drop, however, in  $\Delta C_m$  for flaps at 30 deg at 10.7 kW power,  $\alpha = 2$  deg and  $\delta_s = -15$  deg. This drop is a result of flow separation on the horizontal stabilator due to the high-lift system blowing over the fully deflected stabilator. Figure 41 shows flow visualization comparisons between Mod-III power off at -15 deg stabilator deflection and the same configuration with high-lift power at 10.7 kW. With no high-lift blowing, the flow on the stabilator is still attached at full negative stabilator deflection, but the addition of high-lift power creates a large separation bubble on the underside of the stabilator. It's interesting to note that this phenomenon is not present for flaps at 10 deg.

The increment to rolling moment  $\Delta C_l$  is plotted versus aileron deflection in fig. 42. As with the Mod-III cases, the simulations were run with only the right aileron deflected. As expected, blowing tends to increase the effectiveness of the ailerons, but there is an interesting behavior at positive aileron

deflections for flaps at 30 deg,  $\alpha = 14$  deg, and 4.9 kW. Positive right aileron deflection should produce a negative rolling moment, but the increment due to blowing at this angle of attack is positive (that is, the high-lift blowing is reducing the effectiveness of the aileron). This positive increment in  $\Delta C_l$  at aileron deflections above  $\delta_a = 5$  deg is due to a pocket of separation that forms between the second and third high-lift pylons on the right-hand side of the wing as the aileron is deflected beyond 5 deg, as shown in fig. 43.

Figure 44 shows  $\Delta C_n$  versus rudder deflection with the high-lift system operating at both 10.7 kW and 4.9 kW. In general, the high-lift system appears to have a minimal change in the rudder effectiveness. For flaps at 30 deg, there is a small constant change in yawing moment with  $\Delta C_n \sim 0.0025$  to 0.005. At 4.9 kW and  $\alpha = 14$  deg,  $\Delta C_n$  linearly decreases with rudder deflection and is out of family with the other data. The flaps at 10 deg results are similar to flaps at 30 deg with the exception of a small increase in yawing moment with  $\Delta C_n \sim 0.01$  for full rudder deflection.

#### 4.3.2 Contactor Failures

As described in Section 2.2 Mod-IV and shown in fig. 7, electrical power is supplied to the high-lift motors by the traction batteries via two sets of electrical contactors mounted on pallets (A and B). A single electrical contactor failure was deemed to be a credible hazard. As such, the team decided that this scenario needed to be modeled in the aero database. From fig. 7, a failure of one of the two electrical contactors connected to the high-lift system on pallet A will shut down power to high-lift motors 1, 3, and 5 or 8, 10, and 12, depending on which contactor fails. A failure of one of the contactors on pallet B will shut down power to high-lift motors 2, 4, and 6 or 7, 9, and 11, depending on which contactor fails. Failure of an electrical contactor on pallet B was assumed to be the more serious failure (pallet A versus pallet B) due to the loss of the inboard high-lift motors near the wing root. The rationale for this assumption is twofold. First, the propwash from the inboard high-lift motors was expected to have the most influence on the flow over the horizontal stabilator. And second, the propwash from the inboard high-lift motors was seen to help prevent the flow separation that occurred at the wing root at higher angles of attack in the Mod-III CFD solutions.

The CFD simulations were run for the failure A and failure B scenarios at the same airspeeds used for the nominal operation of the high-lift system except the 35 KCAS case, which is a speed the represents ground operations. The CFD cases were similar to those run for the nominal high-lift scenario with full angle of attack, sideslip, and control surface sweeps being conducted at 58, 75, and 90 KCAS. Due to the asymmetry produced by the high-lift motor failures on one wing, all CFD simulations were run using full-span grids, and for aileron deflection cases, the combined aileron deflection from both left and right ailerons was modeled as opposed to the single sided deflections that were used for the nominal high-lift and for Mod-III CFD. The operational high-lift motors were simulated using the same actuator disk settings used for the nominal high-lift scenario as shown in table 4. The failed motors were assumed to be in a windmilling state due to the loss of power to the motors from the electrical contactor failure. Windmilling was considered to be the worst-case scenario for the failed motors because of the additional drag associated with the windmilling propellers. Table 7 shows the actuator disk settings used for the failed motors.

Table 7. High-lift propeller contactor failure failed motor actuator disk settings.

Hp, ft	KCAS	V, ft/s	$\rho$ , slug/ft <sup>3</sup>	RPM	J	$C_T$	$C_P$	$C_Q$	T, lbf	P, kW	Q, lbf-ft
2,500	50	87.6	0.002208	1,651	1.6844	-0.0496	-0.0352	-0.0056	-1.1	-0.1	-0.2
2,500	58	101.6	0.002208	1,937	1.6652	-0.0418	-0.0253	-0.0040	-1.2	-0.1	-0.2
2,500	65	113.8	0.002208	2,184	1.6542	-0.0373	-0.0199	-0.0032	-1.4	-0.1	-0.2
2,500	75	131.3	0.002208	2,357	1.7685	-0.0328	-0.0147	-0.0023	-1.4	-0.1	-0.2
2,500	90	157.6	0.002208	3,065	1.6324	-0.0285	-0.0101	-0.0016	-2.1	-0.1	-0.2

#### 4.3.2.1 Longitudinal Results

Figures 46-48 show a comparison of  $C_L$ ,  $C_D$ , and  $C_m$  between nominal high-lift system operation and contactor failure scenarios A and B. Total coefficient values, as opposed to deltas, were plotted to show a direct comparison between the nominal high-lift operation and the failure scenario results. As expected, with the loss of 25 percent of the high-lift propulsors, the lift coefficient is lower for the two failure scenarios, compared to the nominal operation, as shown in fig. 47. Both failures have  $C_{L_{max}}$  at a lower angle of attack than the nominal operation with failure B generally peaking at a lower angle of attack than failure A. The earlier loss of lift for failure B is due to separation on the wing root, which is near the failed high-lift propulsor. The failures reduce the total drag and pitching moment coefficients of the aircraft, as shown in figs. 46 and 48.

#### 4.3.2.2 Lateral-Directional Results

Figures 49-51 show  $C_Y$ ,  $C_l$ , and  $C_n$  for the contactor A and B failures. The coefficients are plotted as a function of the angle of attack to show how the asymmetry caused by the failed motors on one side effects the lateral-directional forces and moments. The figures do not include data for nominal, symmetric high-lift operation for comparison because the lateral-directional forces and moments for nominal operation at zero sideslip would be zero due to symmetry with all 12 high-lift motors operating nominally. Figure 49 shows that the side force coefficient slowly increases with increasing angle of attack up until about  $\alpha = 8-12$  deg (depending on the solver), after which the coefficient shows a marked increase. The results from USM3D for the contactor A failure are a departure from the rest of the CFD solvers showing a steady linear increase in  $C_Y$  with angle of attack. Rolling moment coefficient, shown in fig. 50, has a similar trend with the side force coefficient showing a large increase (observed between  $\alpha = 8-12$  deg). Yawing moment coefficient, shown in fig. 51, has more spread between the solvers, but generally appears to be somewhat constant with angle of attack until the  $\alpha = 8-12$  deg, which is where the behavior becomes more erratic.

#### 4.3.2.3 Control Surface Deflections

Stabilator and aileron sweeps were simulated for both contactor failure scenarios. Rudder sweeps were not simulated. Due to the asymmetry of the failures – with only one wing losing partial power – aileron sweeps were modeled with both ailerons deflected, compared to previous nominal Mod-IV and Mod-III CFD cases where only the right aileron was deflected. Figure 52 shows a comparison of  $C_m$  versus stabilator deflection for both nominal high-lift and the two contactor failure cases. Note that the nominal stabilator deflection cases were only run using STAR-CCM+<sup>®</sup>, whereas the failure cases were run mainly using LAVA with some spot checks from STAR-CCM+<sup>®</sup>. As mentioned previously, LAVA was the primary solver used for the contactor failures. Figure 52 shows that there appears to be a small reduction in  $C_m$ , between the two failures, and the nominal case for a given stabilator deflection. Comparing the two failure cases, failure B has slightly lower  $C_m$  than failure A, which is likely due to the loss of the most inboard propulsor in failure B; being the most inboard propulsor, its wake would be expected to have the most direct impingement on the stabilator; hence, the reduction in  $C_m$ , as compared to failure A.

Figure 53 shows a comparison of  $C_l$  versus aileron deflection for both nominal and the two failure cases. Because the nominal high-lift cases only modeled the right-hand aileron, the CFD results from the nominal high-lift runs were combined to yield an estimate of  $C_l$  for the deflection of both the right and left aileron. This combination was necessary to allow for comparison with the contactor failure cases where it was necessary to deflect both ailerons due to the asymmetry of the failure. As might be expected by failing half of the high-lift propulsors on the right wing, the reduction in lift on the right wing causes a positive rolling moment for the two failure cases, as shown in fig. 53.

## 4.4 Ground Effect

The CFD simulations were run to estimate ground effects of Mod-III with the power off and Mod-IV for the aero database. Cases were run for the five different ground plane heights from 5.8 to 31.2 ft. These heights are measured as the vertical distance from the wing-leading edge to the ground plane and represent a range of heights from the approximate wing (resting height above ground with the landing gear deployed) to one wingspan above the ground. For these simulations, a moving ground plane was used and was simulated as a viscous wall using the STAR-CCM+<sup>®</sup> solver and as an inviscid wall with the LAVA solver. The reason for using different ground plane treatments (STAR-CCM+<sup>®</sup> and LAVA) was due to different sets of best practices for the two different solvers. The angle-of-attack sweeps were run for each ground plane height. At the lowest ground plane height (5.8 ft), the angle of attack was limited to 12 deg, as larger angles of attack result in the tail striking the ground.

Figure 54 shows the change in  $C_L$  (at flaps 30 deg as a function of the height above the ground plane) normalized by the wingspan  $\left(\frac{h}{b}\right)$  for both power-off and high-lift power settings of 4.9 and 10.7 kW, respectively. The power-off plot shows a positive  $\Delta C_L$  for angles of attack less than 12 deg that decreases in magnitude moving towards the free air values at  $\frac{h}{b} = 1$ , which is approximately one span height above the ground. At angles of attack of 12 and 14 deg, the  $\Delta C_L$  is negative. Note that these two angles of attack are near  $C_{L_{max}}$  for the wing in free air, at flaps 30 deg. With high-lift power on, there is generally an increase in  $\Delta C_L$  with an increasing power setting for  $\frac{h}{b} < 0.5$ ; however, there are some angles of attack where  $\Delta C_L$  is negative. Figure 55 shows the same data but for flaps at 10 deg. In general, the trends are similar for flaps at 10 deg, compared to flaps at 30 deg. Figure 56 shows the change in  $C_m$  at flaps at 30 deg for power off and high-lift power settings of 4.9 and 10.7 kW. The results show a negative  $\Delta C_m$  for  $\frac{h}{b} < 0.5$  and trends towards zero at  $\frac{h}{b} = 1$ . The trends observed with flaps at 10 deg, shown in fig. 57, are similar to what was observed with flaps at 30 deg.

## 5 Forced Oscillation Computational Fluid Dynamics Results

As mentioned previously, dynamic derivative data for an early, clean (flaps retracted) Mod-III configuration was collected from a wind-tunnel test in the LaRC 12-ft low-speed wind tunnel. The test was run on a 19-percent scale model of the X-57 airplane with a zero-flap deflection. Due to a variety of concerns with the wind-tunnel test data including, but not limited to, installation effects, Reynolds number effects, and the lack of being able to model flaps, the decision was made to use unsteady CFD to estimate the damping derivatives for the Mod-III and Mod-IV configurations. As with the static CFD runs, the CFD simulations started out simple by modeling the powered off Mod-III aircraft and eventually increased in complexity by adding in the high-lift propulsors. To mimic the wind-tunnel test, the unsteady CFD simulations were performed using single-axis forced oscillation movement.

### 5.1 Forced Oscillation Data Reduction Method

As the CFD was initially used as a check of the forced oscillation wind-tunnel testing, the starting point for stability derivative estimation was to use the traditional analysis technique of decomposing the aerodynamic coefficient time history into in-phase and out-of-phase components, and then integrating over several oscillation cycles (ref. 32). A simpler technique is to estimate the angle and rate derivatives using a least-squares fit to the coefficient time history. If no bias term is used in the model, the least-squares technique is identical to the traditional one. While the two analysis techniques yield the same results, the use of separate formulations sometimes pointed out CFD processing problems that may have otherwise been harder to notice.

Though not used for this work, a real-time version of the traditional data analysis approach was created that could provide stability derivative estimates after each CFD iteration. For the least-squares approach, a recursive least-squares algorithm could be used to provide real-time results. The real-time

methods could be incorporated into automated checks that could stop CFD runs once the stability derivatives have sufficiently converged.

## 5.2 Power-Off Results

Table 8 shows the conditions that were analyzed for Mod-III. Separate CFD simulations were run for each axis of rotation with the aircraft oscillating in a sinusoidal motion with a fixed amplitude and frequency that was dependent on the particular axis of rotation. The CFD cases were run with flaps set at 0, 10, and 30 deg. The CFD results for flaps at 0 deg were compared with the corresponding dynamic derivatives obtained from the 12-ft wind-tunnel test.

Table 8. Forced oscillation Computational Fluid Dynamic conditions.

Hp, ft	KCAS	Vinf, ft/s	Flap	Axis	Amplitude, deg	k	Frequency, cycles/s
8,000	133	253	0	Pitch	5	0.02169	0.820
8,000	133	253	0	Roll	10	0.28632	0.729
8,000	133	253	0	Yaw	5	0.14316	0.365
2,500	94	164.6	10	Pitch	5	0.02169	0.534
2,500	94	164.6	10	Roll	10	0.28632	0.474
2,500	94	164.6	10	Yaw	5	0.14316	0.237
2,500	88	154.1	30	Pitch	5	0.02169	0.500
2,500	88	154.1	30	Roll	10	0.28632	0.444
2,500	88	154.1	30	Yaw	5	0.14316	0.222

### 5.2.1 Longitudinal Derivatives

Pitch damping  $C_{m_q}$  was the only longitudinal dynamic derivative that was estimated for the aero database. Figure 58 shows the CFD estimates for  $C_{m_q}$  as a function of angle of attack. Compared to the wind-tunnel data, the CFD estimates were more negative, indicating a greater degree of pitch damping. The wind-tunnel data were not corrected for installation effects, which may be one reason for the difference between the two methods. A lesson learned from this process, for application moving forward, is to decrease the pitch oscillation amplitude as the nominal angle of attack increases towards the stall angle of attack in order to keep the simulation out of the post-stall angle-of-attack region, which causes  $C_{m_q}$  to rapidly decrease in magnitude (trend towards 0). The Kestrel data for flaps at 30 deg show this rapid decrease in the value of  $C_{m_q}$  as angle of attack is increased past 10 deg. As a reminder, the steady-state CFD results for this configuration showed a stall angle of attack of approximately 14 deg, so a pitch oscillation of 5 deg, which is added to the nominal angle of attack of 10 deg, puts the model into a post-stall region for a portion of the oscillation cycle.

### 5.2.2 Lateral-Directional Derivatives

Figure 59 shows the estimates for roll damping  $C_{l_p}$ . The CFD data for flaps at 0 deg show good agreement with the wind-tunnel data, where  $C_{l_p}$  is negative and decreases in magnitude with increasing angle of attack. The negative value of the derivative indicates positive dynamic roll stability. There are no significant differences between flaps at 0, 10, and 30 deg. Figure 60 shows the results for the yawing moment due to roll rate derivative  $C_{n_p}$ . Again, the flaps at 0 deg, CFD match the wind-tunnel data fairly well until angles of attack above 12 deg are reached. The CFD predicts that increasing flap deflections will cause the magnitude of  $C_{n_p}$  to increase.

The CFD results for yaw damping  $C_{n_r}$  and the cross derivative rolling moment due to yaw rate  $C_{l_r}$  are shown in figures 61 and 62. The  $C_{n_r}$  estimates from the CFD show similar trends to the 12-ft wind-tunnel data, but there is significant variation when comparing the individual solvers. The  $C_{n_r}$  values for all flap settings are negative, indicating positive dynamic stability. Figure 62 shows the CFD estimates for  $C_{l_r}$ . At angles of attack below 5 deg, the flaps at 0 deg, and CFD results from all three solvers agree well with the wind-tunnel data, but then the CFD results tend to diverge at angles of attack greater than 5 deg. For flaps at 30 deg, the CFD results start to exhibit a steep increase in  $C_{l_r}$  above an angle of attack of 10 deg, similar to how the  $C_{m_q}$  results tended to rapidly increase towards zero at higher angles of attack, near the steady-state stall angle of attack.

### 5.3 High-Lift Power

Dynamic derivatives were also estimated at high-lift power settings of 4.9 and 10.7 kW using the same actuator disk conditions used for the Mod-IV steady-state analysis and at the same flight conditions. The two solvers used for this effort were STAR-CCM+® and Kestrel. In general, the high-lift system tended to increase the magnitude of the damping derivatives.

#### 5.3.1 Longitudinal Derivatives

Figure 63 shows comparisons of  $C_{m_q}$  as a function of angle of attack for 4.9 and 10.7 kW, for flaps at 30 deg. For comparison, the power-off  $C_{m_q}$  estimates from CFD are included in the plot. At angles of attack below 8 deg, pitch damping tends to increase (values become more negative) as the high-lift power setting increases. Above 10 deg angle of attack,  $C_{m_q}$  with high-lift blowing tends to move toward zero, with STAR-CCM+® predicting a nearly-zero value at an angle of attack of 13 deg and Kestrel predicting a positive, unstable  $C_{m_q}$  at 12 deg angle of attack. The reason for the trend towards zero is thought to be the same as what was described for the power off  $C_{m_q}$  (Section 5.2.1), where the model pitch oscillation amplitude ventures into the post-stall angle-of-attack region.

#### 5.3.2 Lateral-Directional Derivatives

Figures 64-67 show comparisons of the lateral-directional derivatives with the high-lift power on, along with the power-off results for flaps at 30 deg. Roll damping  $C_{l_p}$  (shown in fig. 64) tends to trend negative with an increasing high-lift power setting for all angles of attack, with the exception of the Kestrel, and results in a 12-deg angle of attack for 4.9 kW. The cross derivative  $C_{n_p}$  (shown in fig. 65) has a similar trend to  $C_{l_p}$ , where the damping increases with an increased high-lift power setting, except for the Kestrel results at 12-deg angle of attack with the high-lift system at 4.9 kW.

Figure 66 shows the results for yaw damping  $C_{n_r}$  along with the power-off results for Mod-III for flaps at 30 deg. Similar to the other derivatives, high-lift power tends to increase  $C_{n_r}$ , although the STAR-CCM+® results show that 4.9 kW blowing has a larger magnitude  $C_{n_r}$  than 10.7 kW, whereas the Kestrel results are the opposite. The CFD results for  $C_{l_r}$  (shown in fig. 67) tend to show more variation for a given solver when compared to the power-off results, making it harder to make any general conclusions about the power-on effects on  $C_{l_r}$ .

## 6 Construction of the Database

### 6.1 Aerodynamic Model Structure

The overall aerodynamic model consists of a baseline, power-off model for the X-57 and sections that add aerodynamic effects due to the cruise and high-lift propellers. A diagram of the model structure is shown in fig. 68. The high-lift propeller effects include the modeling of multiple failure modes. Each section of the overall aerodynamic model contains uncertainty terms. The uncertainties are implemented

differently in different parts of the model (for example, as scale factors that multiply some terms or bias terms that are added to other components).

The aerodynamic model tables were created by combining the results from the myriad CFD solvers. Results were combined in different fashions, depending on what results were available for a particular model section (that is, how many CFD solvers, whether the solvers ran the same flight and/or power conditions, and so on), as well as the coverage of the condition space, and the shape of the response surface. Where multiple solvers ran the same conditions, averaging the results was the preferred method of creating the tables. If the conditions didn't match, parametric (least-squares) surface fitting or a non-parametric fitting tool was used to create the tables. In some places, interpolation or extrapolation was used to estimate data for one CFD solver so that results could more easily be blended with another solver.

## 6.2 Uncertainties

Uncertainties can be applied to most components of the X-57 aerodynamic model through either biases or scale factors. The power-off model contains uncertainty biases that are specified in tables for 1-sigma, and then multiplied by a signed amount when the aerodynamic model is used. The 1-sigma uncertainties were based on a combination of engineering judgment, the scatter between the different CFD solver results, and the accuracy of parametric surface fits (where used). Where parametric fits were used, uncertainties were generated based on the standard errors in the model parameters. The role of engineering judgment was to shape the uncertainty tables and to set floors for the uncertainty values. For some terms, the starting point for the uncertainty table was a flat percentage of 5 or 10 percent. For other terms, such as power-on deltas, the starting point was an uncertainty table that produced a resulting aerodynamic delta of zero at 3-sigma.

The uncertainties for the power-on sections of the aerodynamic model are implemented as scale factors that increase or decrease the magnitude of the power-on aerodynamic deltas. Separate scale factors are applied to each part of the model (for example, one scale factor is used for scaling all the high-lift rudder deltas, whereas other scale factor values are used to scale the left- and right-aileron high-lift deltas). Early versions of the aerodynamic model solely used sigma-based uncertainty terms for the power-on deltas, but the resulting model was cumbersome and arguably contained too many uncertainty terms to be used effectively. In the case of the high-lift rudder and aileron uncertainties, using grouped scale factors instead of bias tables reduced the number of uncertainty terms from twelve to three. Similar reductions across the high-lift, cruise, and failure models produced an uncertainty model that was considerably more manageable. The reduced complexity comes at the cost of not being able to independently vary all the aerodynamic coefficients in each part of the model, in essence, for example, making the assumption that all high-lift rudder deltas get stronger or weaker together. Separate scale factors can be applied to the individual force and moment deltas for the base high-lift and cruise propeller effects and for the high-lift effects on the stabilator.

## 6.3 Baseline Model

The baseline aerodynamic model consists of the bare airframe force and moment coefficients and additional components due to rate derivatives and control surface deflections. The base force and moment coefficients are scheduled with angle of attack, sideslip, and flap deflection. Rate derivatives are only dependent on angle of attack. Control surface effects are modeled as deltas, not derivatives. Ground effects are scheduled with angle of attack, flap deflection, and height above ground.

Uncertainties for the power-off aerodynamics are implemented as sigma-based bias terms, except for the ground effect uncertainties, which are implemented as a scale factor that acts on all ground effect aerodynamic terms. Left and right ailerons have separate uncertainty terms. Additional uncertainty terms are included for  $C_{L_\alpha}$  and  $C_{m_\alpha}$  so that the lift curve slope and static stability can be changed, since the regular uncertainty terms would only bias the  $C_L$  and  $C_m$  curves up and down (thereby only changing trim conditions). Likewise, separate terms are included for  $C_{m_{\delta_S}}$ .

## 6.4 Cruise Propeller Effects

Aerodynamic effects due to the cruise propellers are modeled for the base forces and moments, ground effect (CFD data not presented in this report for brevity), and ailerons (at zero sideslip). The CFD results indicated that the cruise propellers did not significantly change the effectiveness of the rudder and stabilator. Cruise propeller effects are functions of advance ratio and blade pitch. For the base terms and aileron deltas, effects are modeled separately for the left and right propellers. The rate derivative and ground effect tables are based on the average advance ratio from the two propellers. The ground effect tables do not depend on blade pitch.

The CFD results indicated the cruise propellers produced some aerodynamic changes with sideslip and aileron deflection, but the results were inconsistent. Rather than creating standalone, always-on tables for these effects, uncertainties were implemented as sigma-based uncertainty biases. While these aileron and beta uncertainties are implemented separately for the left and right sides, a single scale factor is applied to them. Early versions of the aerodynamic model included similar sigma-based uncertainties for the flap effects, but they were removed from the model because the magnitudes were small, and the effects could be captured using other terms in the model.

## 6.5 High-Lift Propeller Effects

High-lift propeller effects are modeled for the base force and moment coefficients, the rate derivatives, and all of the control surfaces. Ground effect deltas are also included. High-lift effects are functions of advance ratio. The base forces and moments are modeled separately for the left and right sides, assuming each propeller on that side has the same advance ratio; other terms use an overall average advance ratio – the advance ratio for propeller 7 is used for the left side, and propeller 8 is used for the right side.

While the CFD for the non-failure cases used the same advance ratio for all twelve high-lift propellers, there was a need to model asymmetric high-lift effects, apart from the contactor failure scenarios. A limited number of CFD cases (data not presented in this report for brevity) were performed with non-operating high-lift propellers on one side. Results from these cases were used to create asymmetric lateral-directional aerodynamic deltas that are used if one side has failed, with the assumption that the left and right effects can be superimposed. When there is no failure, nominal high-lift lateral-directional deltas are used based on an average advance ratio for the entire wing. For the pitch terms, separate left and right contributions are always used, implemented simply by halving the table lookup results from each side.

## 6.6 High-Lift Propeller Contactor Failure Models

External to the main high-lift effects model is a separate model for the various electrical contactor failures. The aerodynamic effects differ depending on whether contactor A or B has failed. In the aerodynamic model, tables exist for left- and right-side (A and B) contactor failures. In the simulation, a failure mode flag is used to select between those four cases, as well as the cases where both sides have either an A or B contactor failure. The simulation does not include the option to have a contactor A on one side and B on the other. There are no uncertainties for the contactor failure aerodynamic model.

# 7 Summary

An aerodynamic database was created for the X-57 Modification-III and Modification-IV configurations. This database was constructed entirely from Computational Fluid Dynamics estimates of the force and moment coefficients, which were estimated using four different computational solvers. The Computational Fluid Dynamics simulations modeled not only the power-off aerodynamics of the Modification-III configuration but also the aero-propulsive effects due to the cruise motors mounted at the airplane wingtips and the high-lift motors distributed along the leading edge of the wing for the Modification-IV configuration. The cruise motor placement at the wing tips, rotating counter to the wingtip vortices, was predicted to reduce the induced drag coefficient by  $\Delta C_D = -0.0028$ , which is

approximately 4.8 percent of the total airplane drag at cruise, assuming a gross weight of 3,000 lb. For the Modification-IV configuration, the estimated lift coefficient at maximum high-lift power (10.7 kW) produced  $C_{L_{max}} = 4.4-4.58$ , which provides a lift margin of between 11-16 percent over the design goal of  $C_{L_{max}} \geq 3.95$ , at the weight-adjusted stall speed of 58 KCAS. Unsteady Computational Fluid Dynamics simulations were run on both the Modification-III and Modification-IV configurations to provide estimates of dynamic derivatives for the two configurations. In general, the blowing due to the high-lift system increased the damping in all three axes. The Computational Fluid Dynamics data were reduced and used to create aerodynamic models of the Modification-III and Modification-IV configurations that included an uncertainty model for the aerodynamics. These models were implemented in batch, and piloted simulations of the X-57 airplane were used for airworthiness evaluations and mission planning for the Modification-III and Modification-IV configurations.

## 8 Figures



Figure 1. The X-57 Maxwell airplane (Modification II configuration).




	<p><b>Mod II:</b> Retrofit a baseline General Aviation aircraft with an electric propulsion system.</p>	<p><b>Mod III:</b> Modify the configuration with a cruise-optimized wing and distributed electric propulsion system.</p>	<p><b>Mod IV:</b> Design for adequate low speed takeoff and landing characteristics with an integrated DEP system.</p>
<p><b>OBJ-1:</b> Develop distributed electric propulsion (DEP) airworthiness standards with industry.</p>	<p><u>Mod II reduces risk for Mods III and IV:</u> Optimize the design for cruise power consumption with a target of 3.3x reduction in energy from the baseline aircraft.</p>	<p><u>Mod III provides cruise speed data for DEP designs, technologies and systems:</u> Optimize the design for improved cruise power consumption with a target of 1.5x reduction in energy from the mod II configuration.</p>	<p><u>Mod IV provides low speed data for DEP designs, technologies and systems:</u> Design the integrated system to have a minimum controlled flight speed of 58 KCAS or less while maintaining acceptable pilot workload and handling qualities.</p>
<p><b>OBJ-2:</b> Increase regulators' proficiency in the development of airworthy electric aircraft and distributed electric propulsion systems.</p>			
<p><b>OBJ-3:</b> Share X-57 integrated DEP design &amp; lessons learned with industry and academic stakeholders.</p>			
<p><b>OBJ-4:</b> Provide a reference vehicle for DEP technology advancement.</p>			

Figure 2. The X-57 project objectives for Modifications II, III, and IV.



Figure 3. The X-57 configurations.



Figure 4. Armstrong Flight Research Center X-57 piloted simulation cockpit layout.

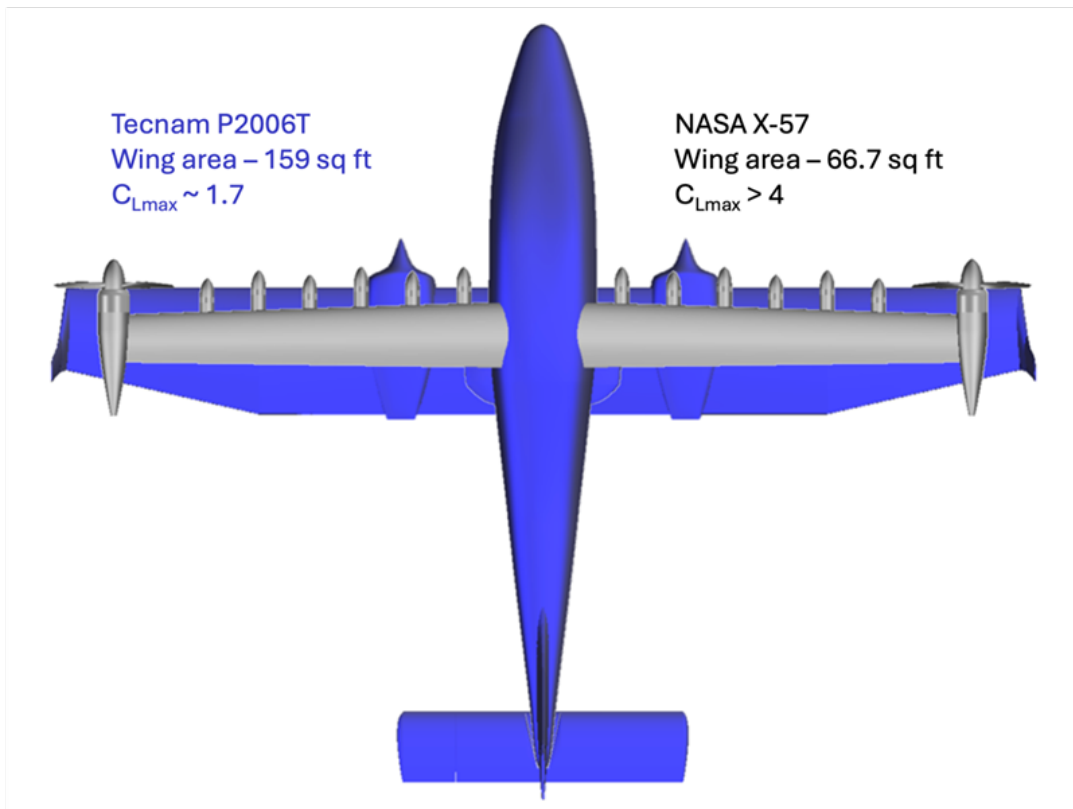


Figure 5. Comparison between the Tecnam P2006T airplane, and the X-57 Modification III wing planforms.



- 5 blades, 1.89 ft (0.576m) Diameter
- 91.1 Activity Factor
- Design Condition
  - Sea Level, 1976 US Standard Atmosphere
  - 58.0 KEAS (23.9 m/s) Freestream Velocity
- Performance @ Design Condition
  - 4550 RPM @ 450 ft/s (137 m/s) tip speed
  - 14.3 hp (10.7 kW) Shaft Power
  - 16.2 ft-lb (22.0 N-m) Shaft Torque
  - 48.2 lbf (215 N) Gross Thrust
  - 1.11 Integrated Lift Coefficient

Figure 6. High-lift propeller and motor descriptions.

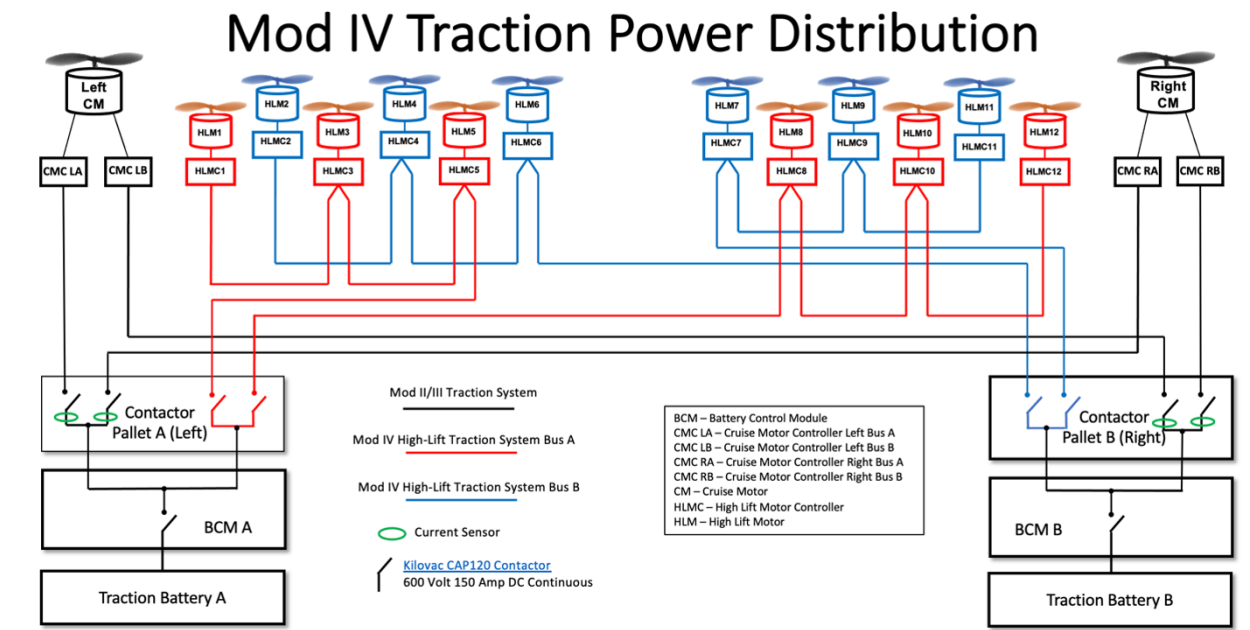


Figure 7. The X-57 high-lift traction power system layout.

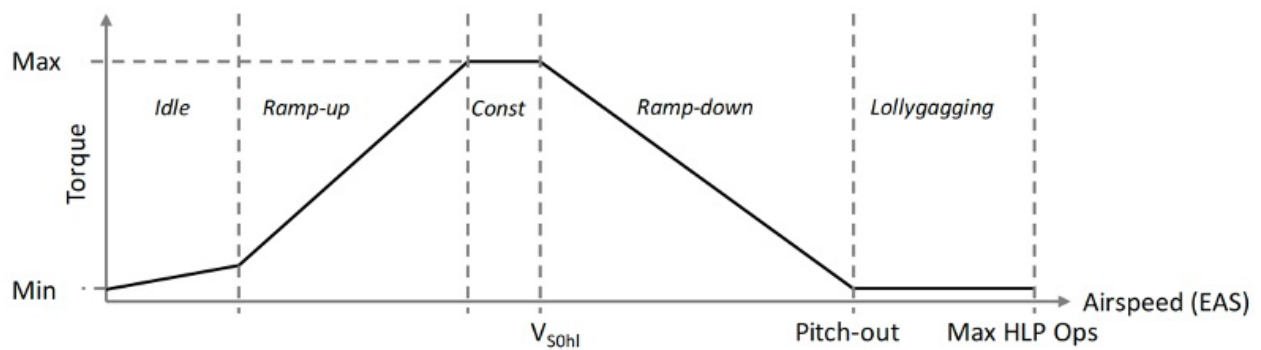


Figure 8. Notional plot of high-lift motor torque schedule with airspeed.

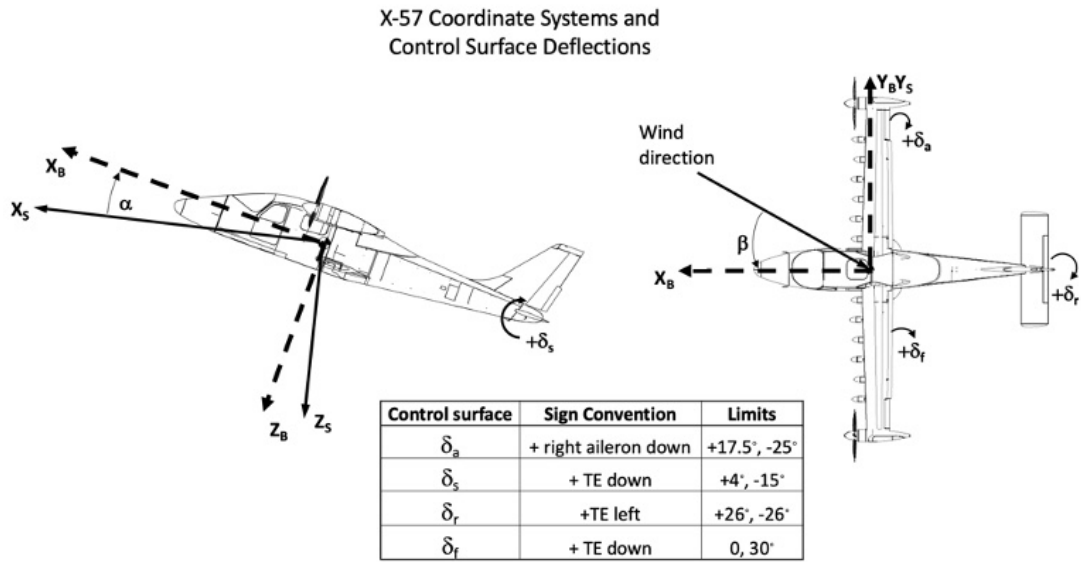


Figure 9. The X-57 coordinate systems and control surface deflection definitions.

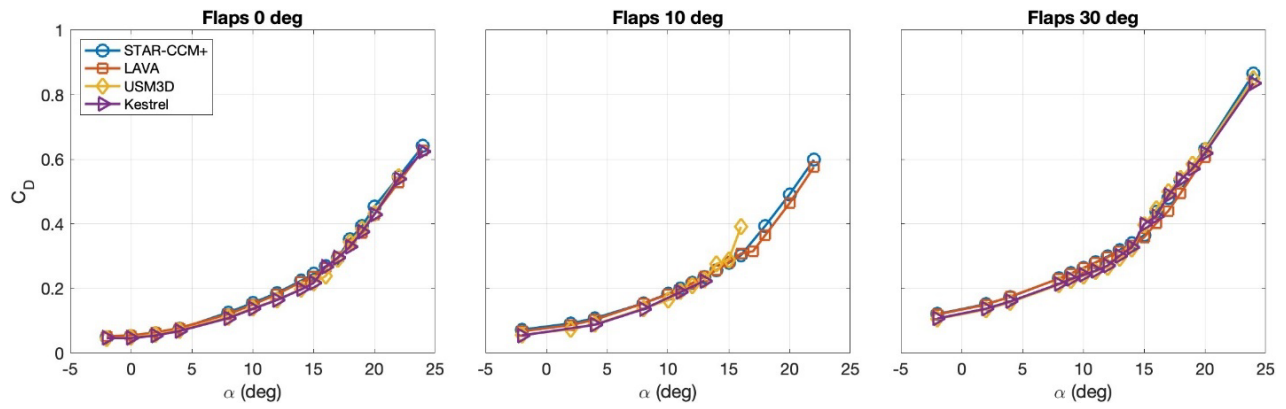


Figure 10. Modification III drag coefficient  $C_D$ .

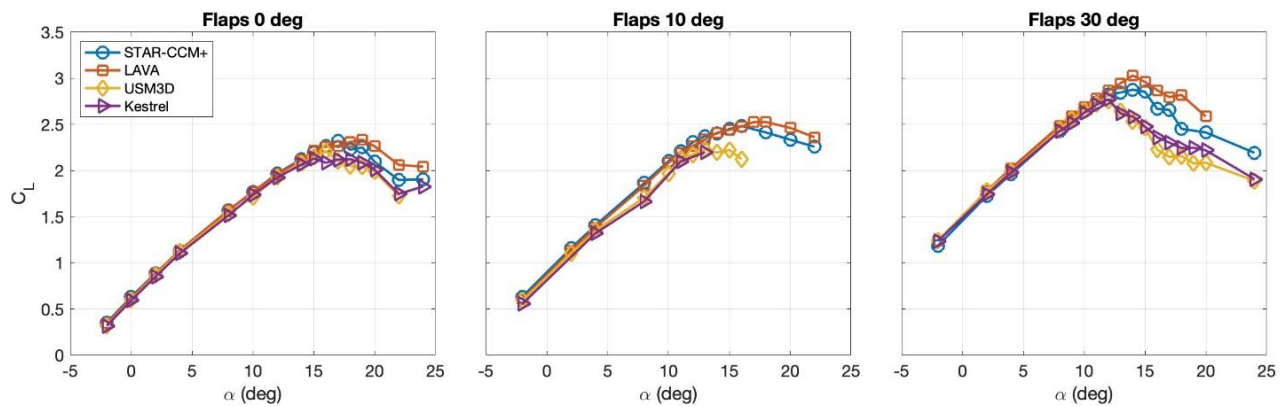


Figure 11. Modification III lift coefficient  $C_L$ .

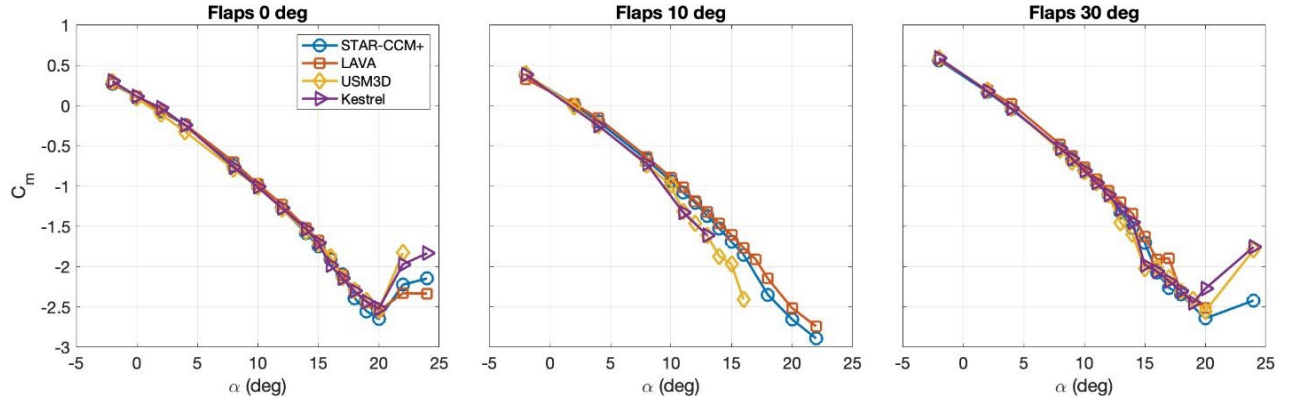


Figure 12. Modification III pitching moment coefficient  $C_m$ .

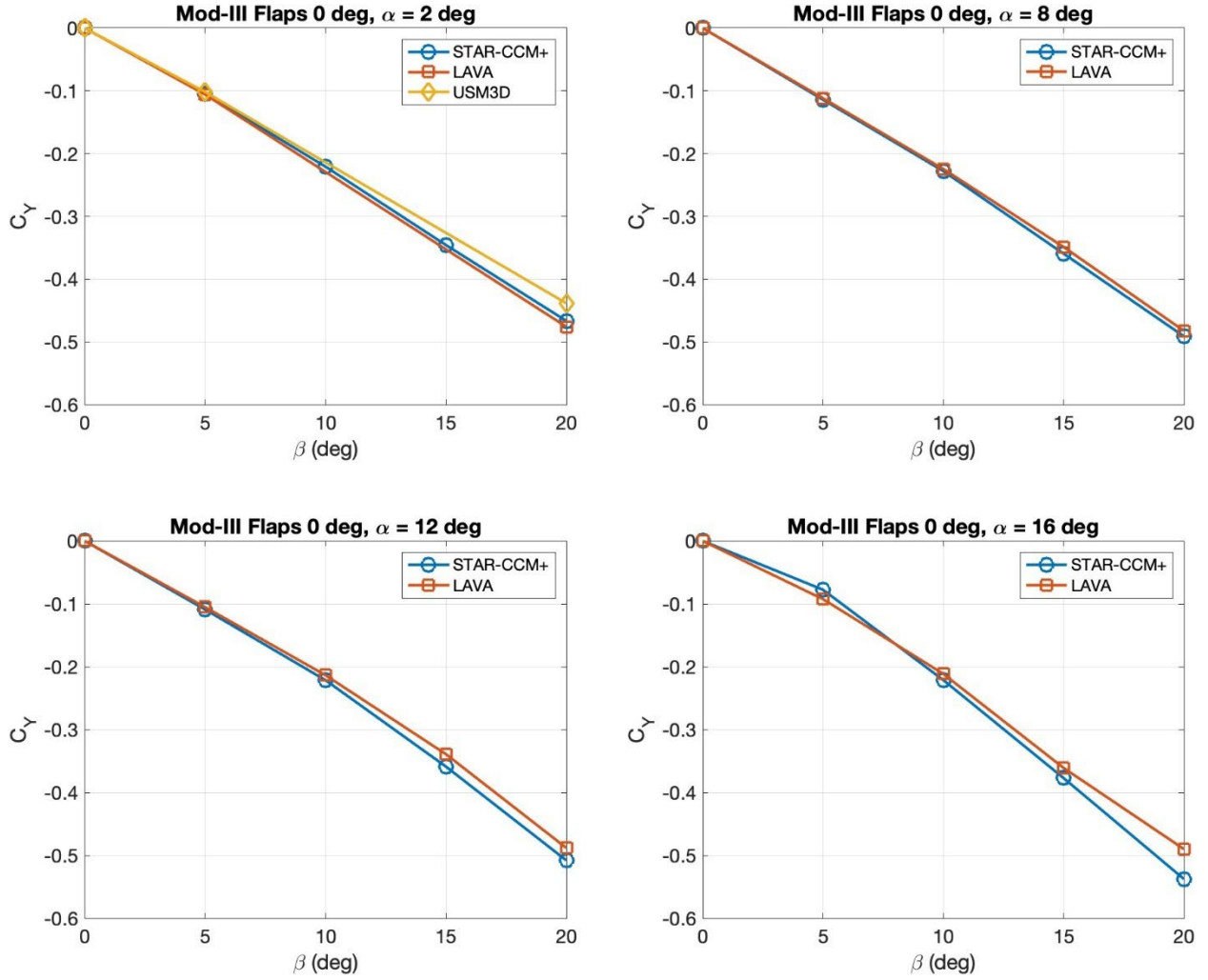


Figure 13. Modification III side force coefficient  $C_Y$ , flaps at 0 deg.

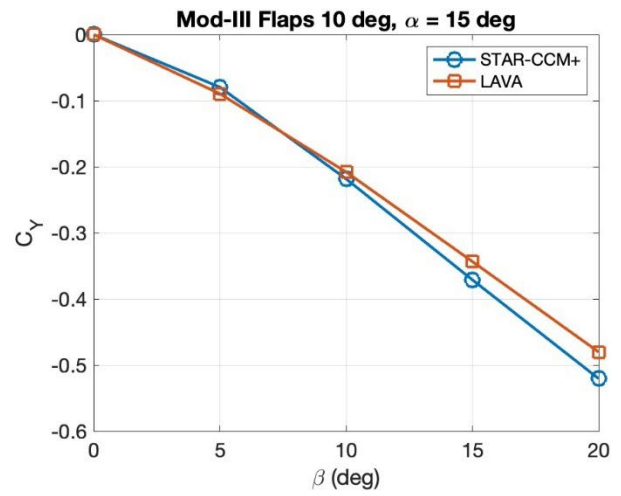
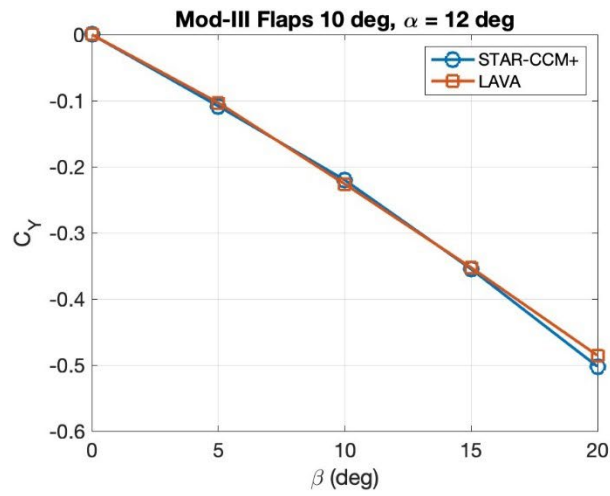
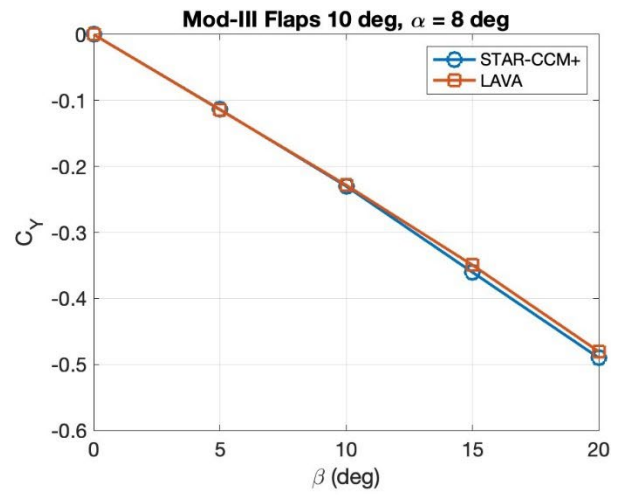
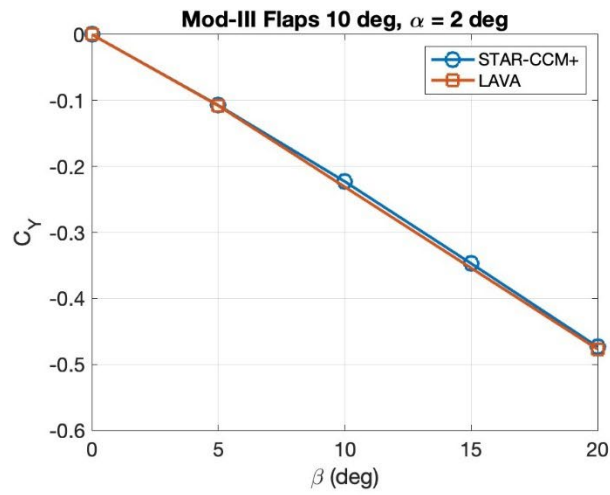


Figure 14. Modification III side force coefficient  $C_Y$ , flaps at 10 deg.

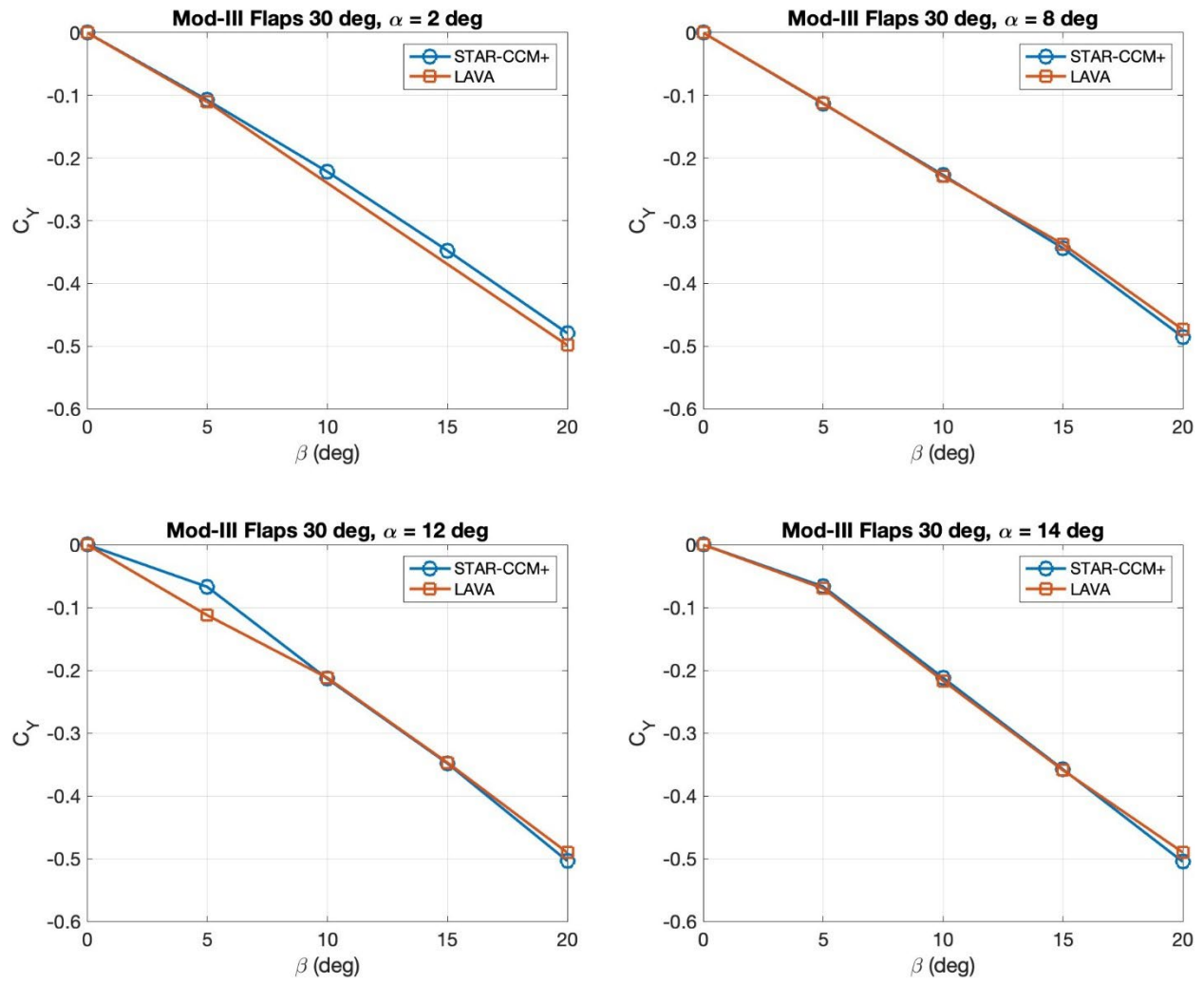


Figure 15. Modification III side force coefficient  $C_Y$ , flaps at 30 deg.

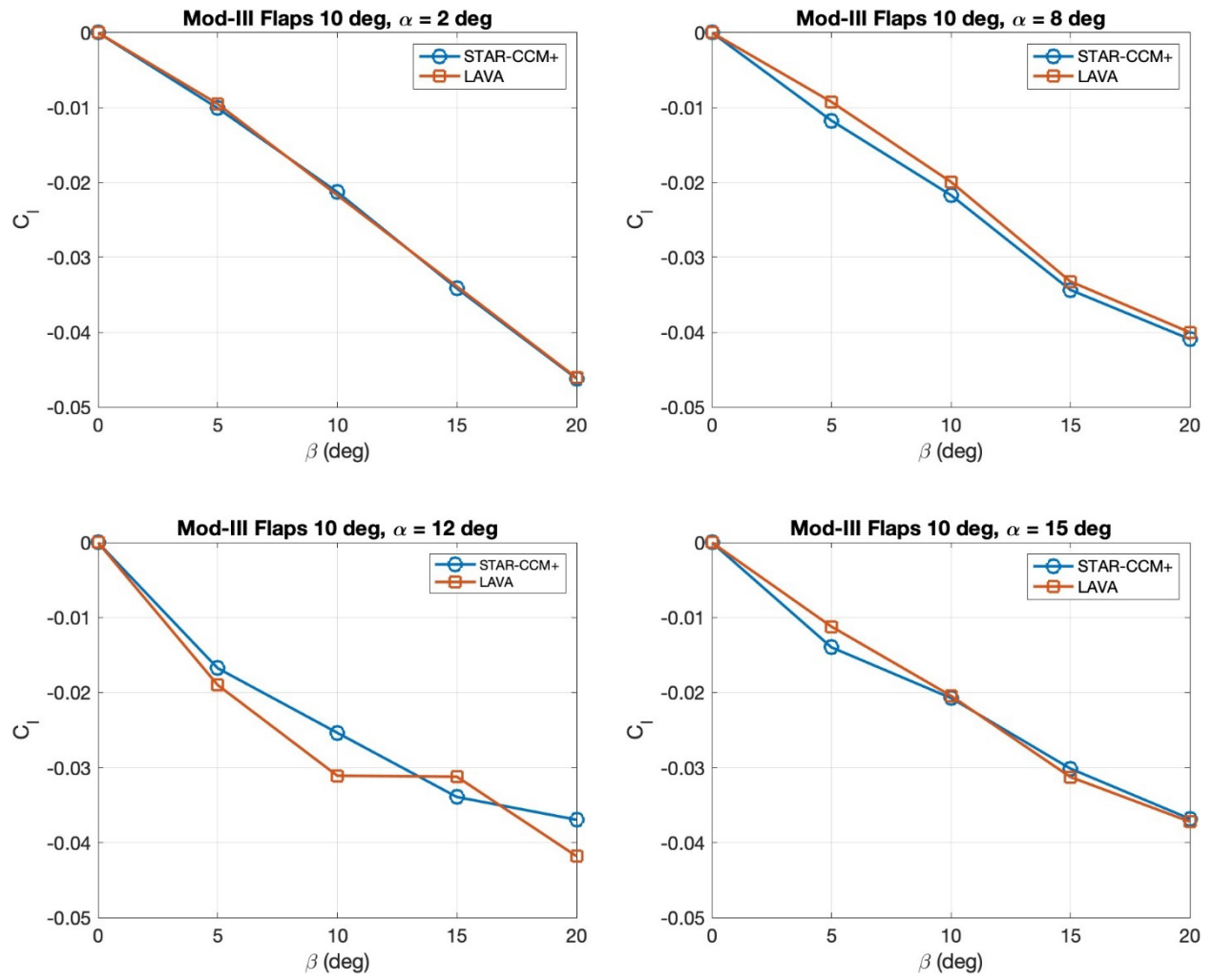


Figure 16. Modification III rolling moment coefficient  $C_l$ , flaps at 0 deg.

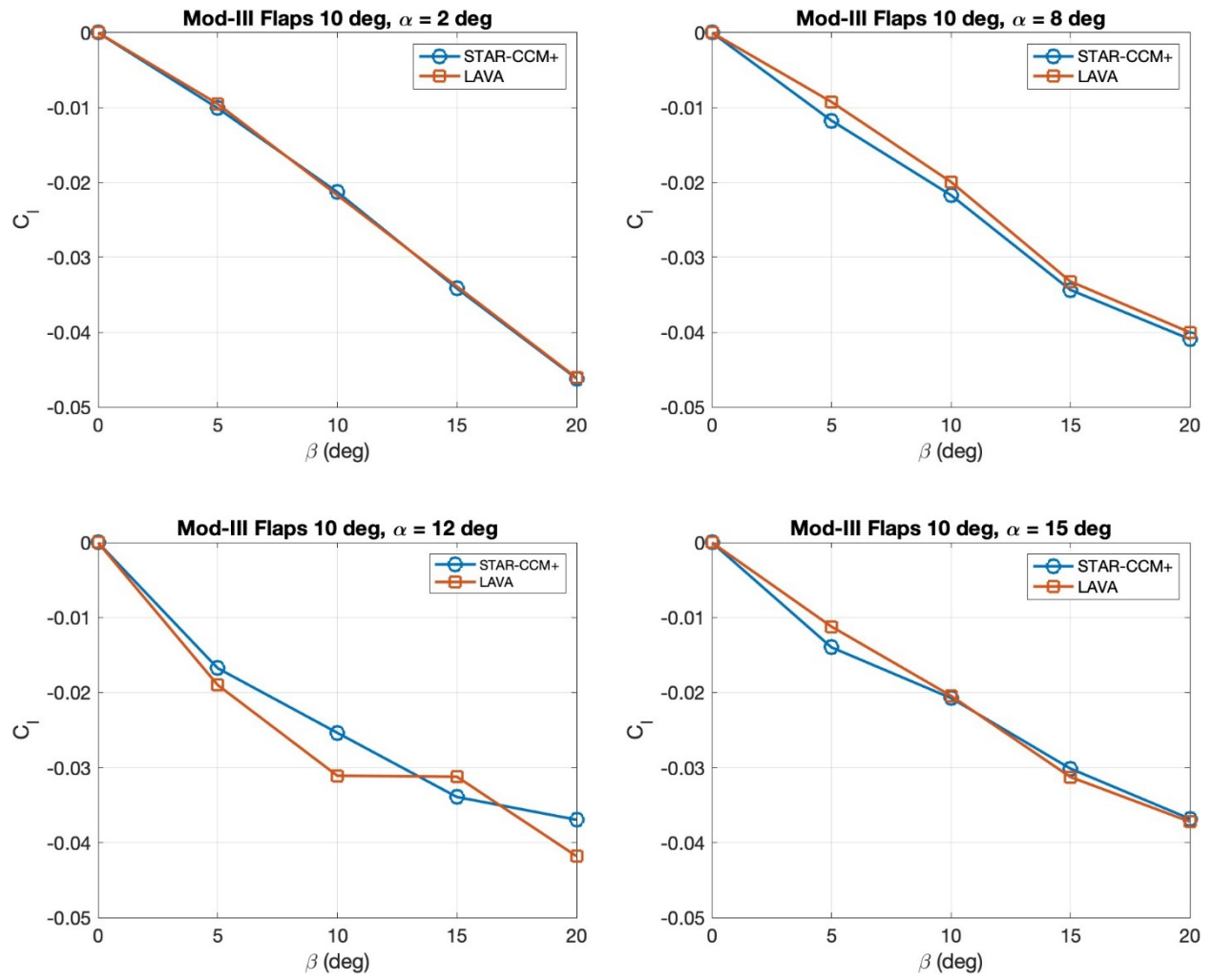


Figure 17. Modification III rolling moment coefficient  $C_l$ , flaps at 10 deg.

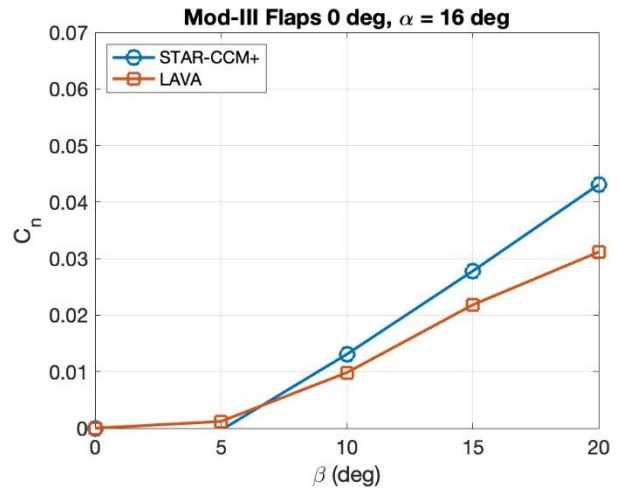
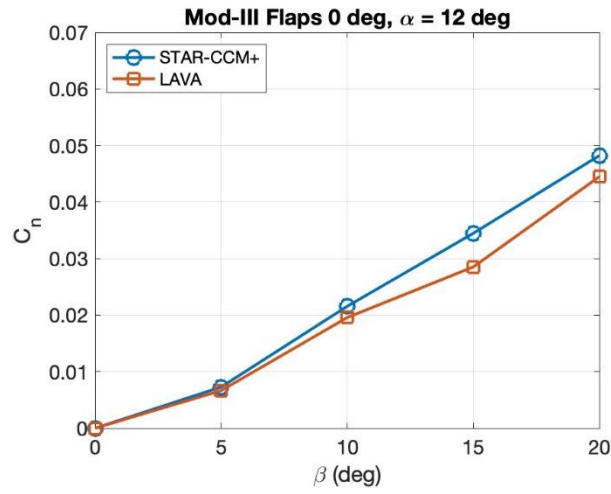
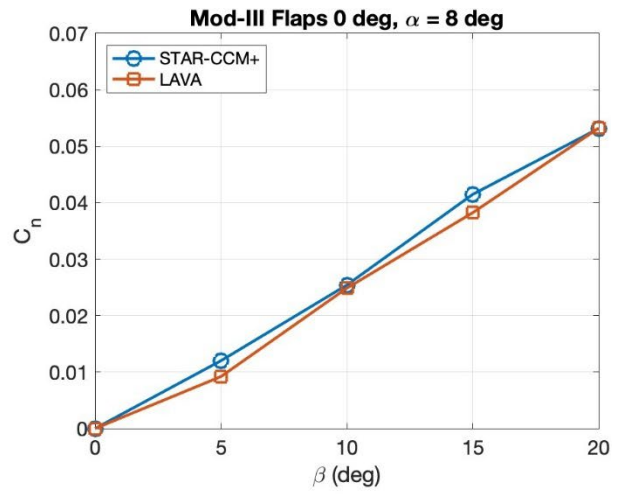
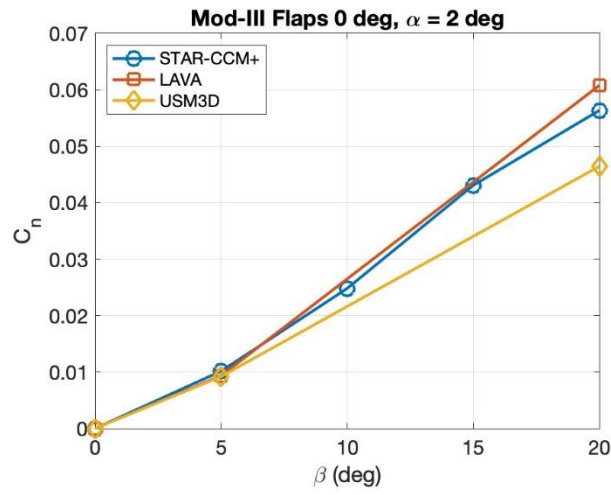


Figure 18. Modification III rolling moment coefficient  $C_l$ , flaps at 30 deg.

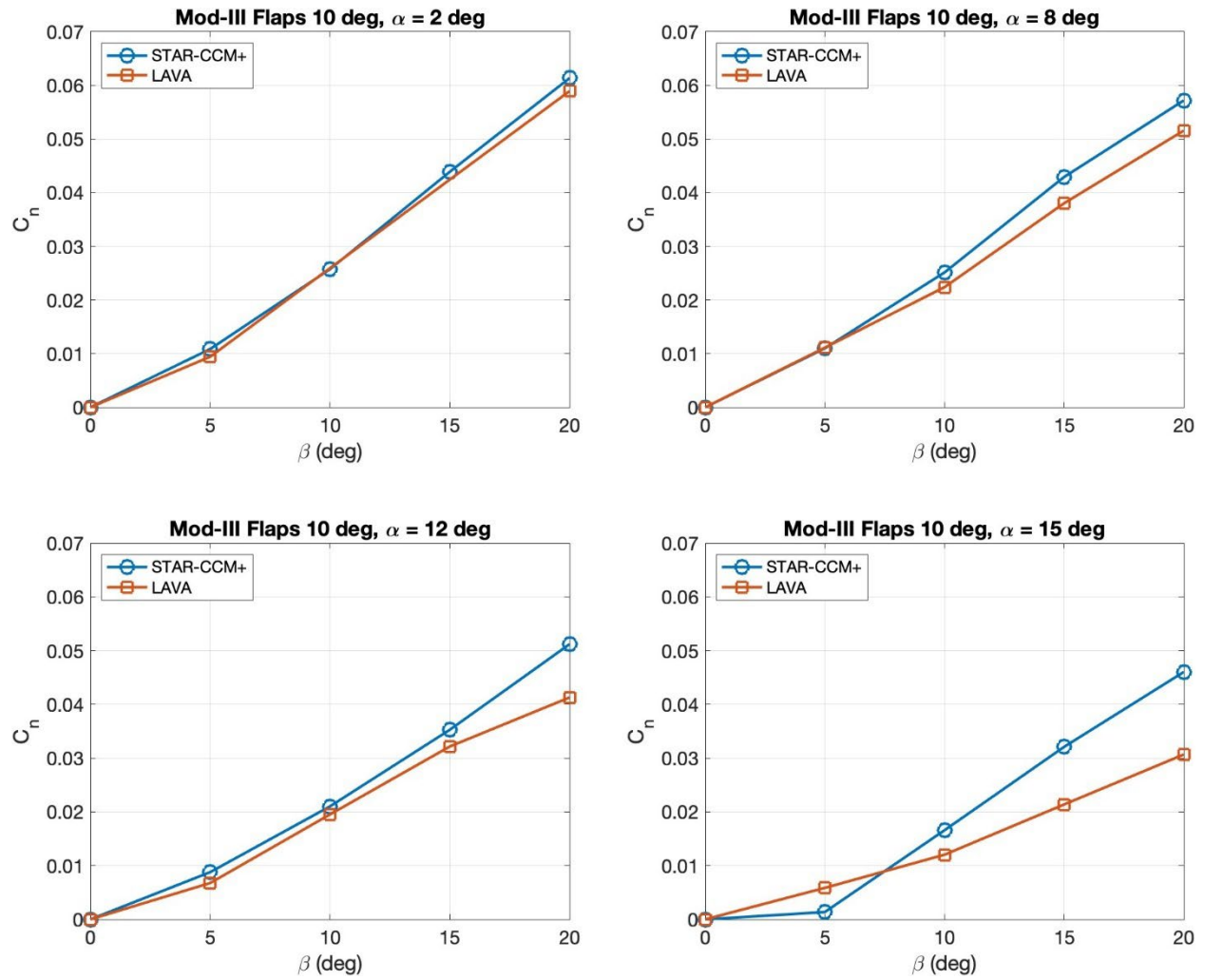


Figure 19. Modification III yawing moment coefficient  $C_n$ , flaps at 0 deg.

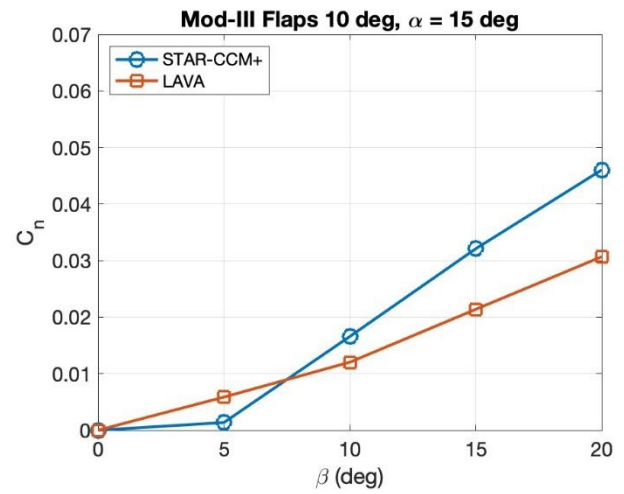
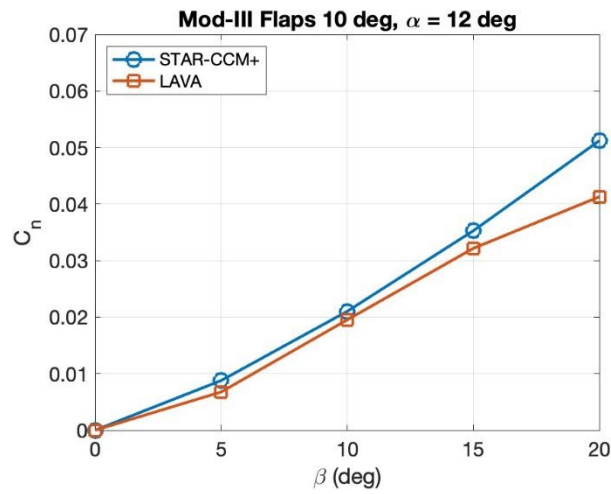
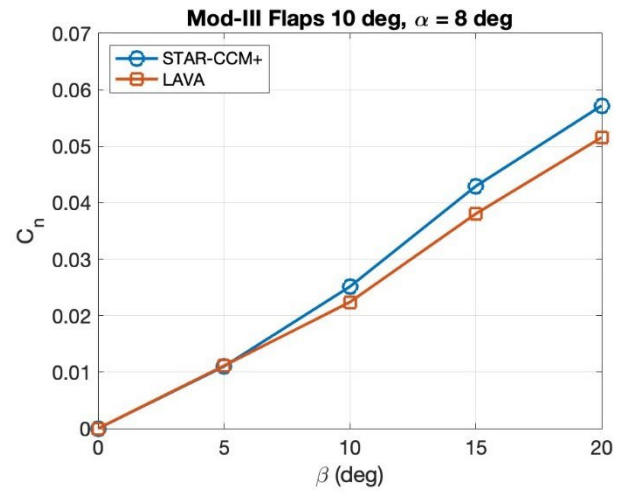
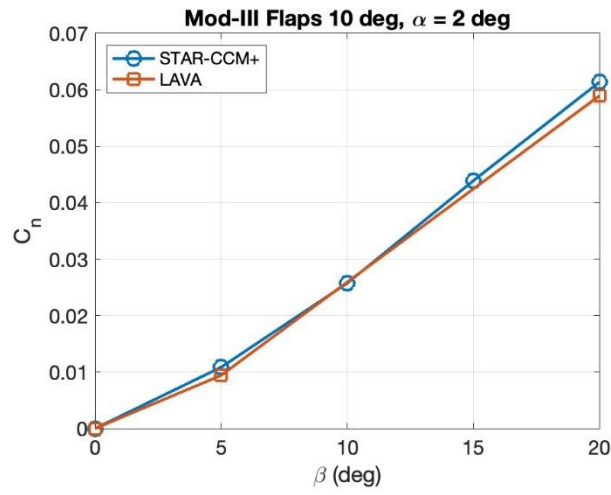


Figure 20. Modification III yawing moment coefficient  $C_n$ , flaps at 10 deg.

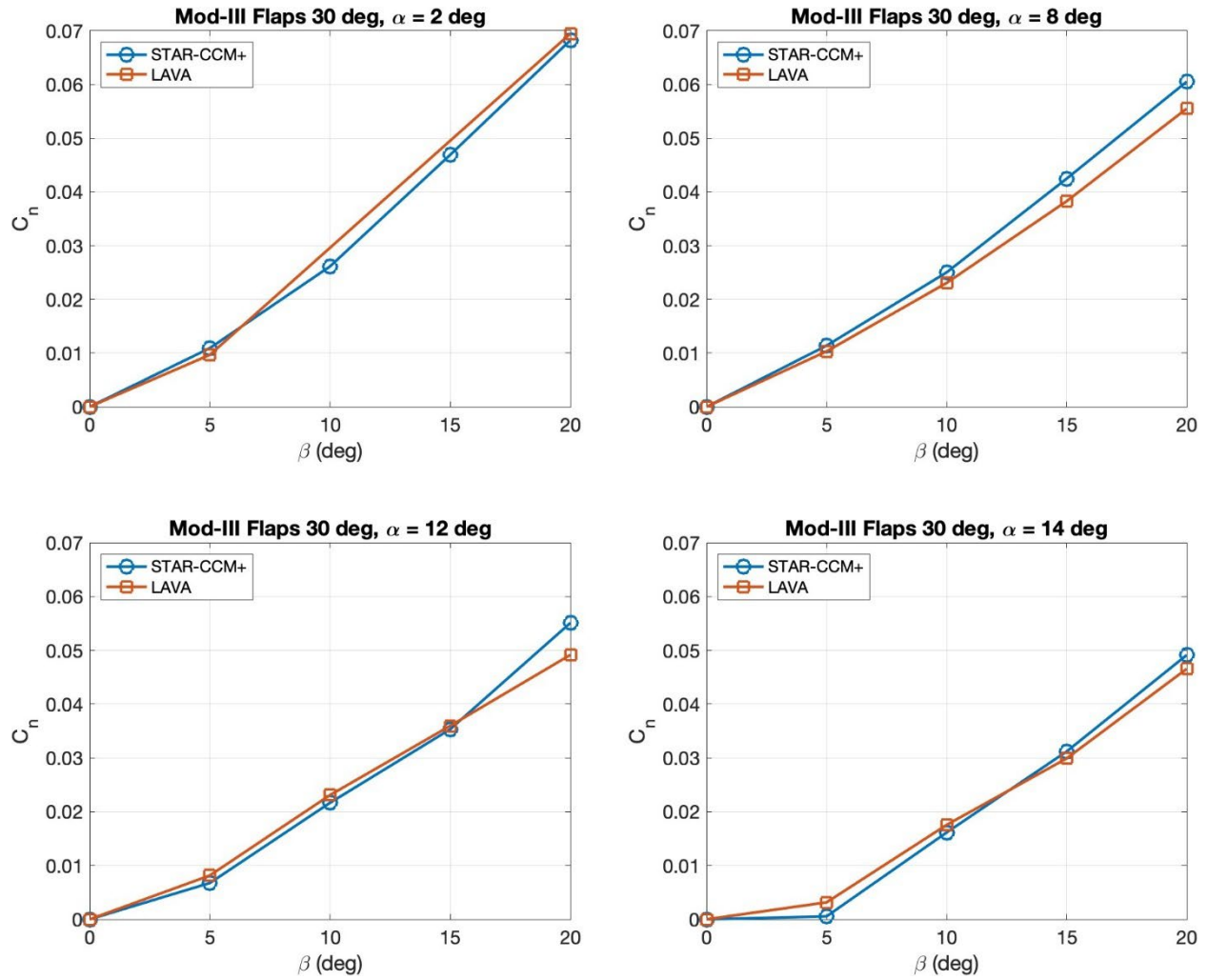


Figure 21. Modification III yawing moment coefficient  $C_n$ , flaps at 30 deg.

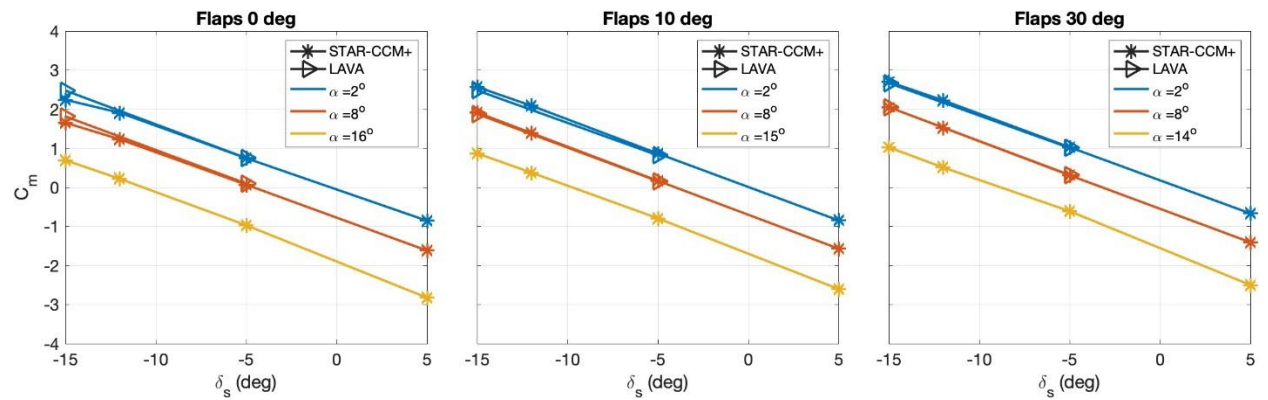


Figure 22. Modification III pitching moment coefficient  $C_m$  due to stabilator deflection.

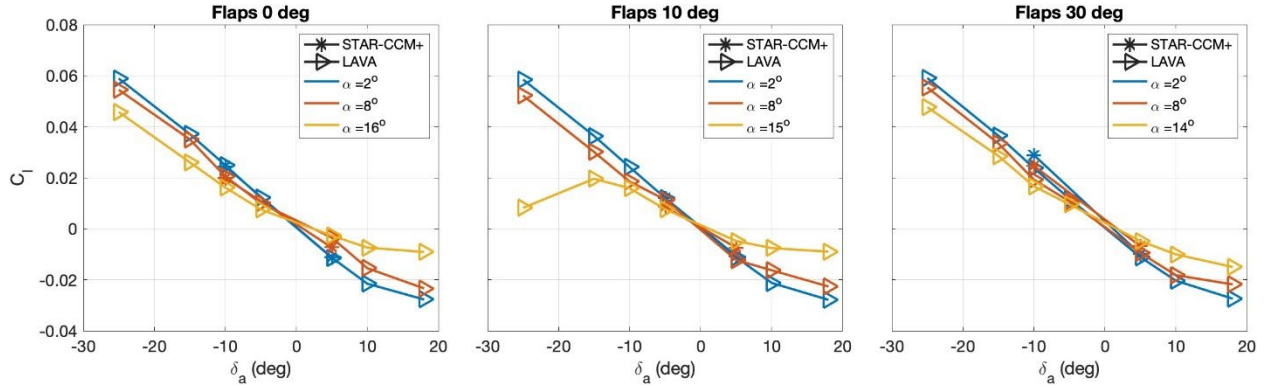


Figure 23. Modification III rolling moment coefficient  $C_l$  due to aileron deflection (right aileron deflection only).

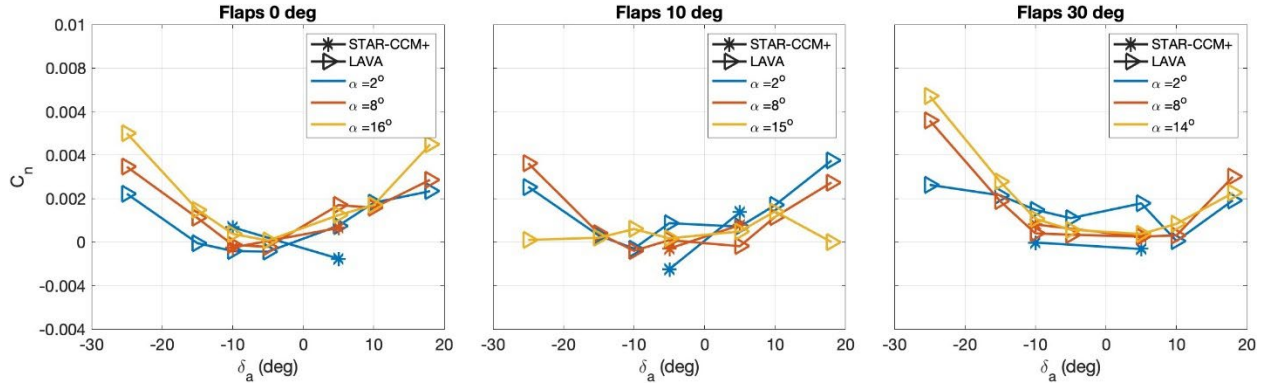


Figure 24. Modification III yawing moment coefficient  $C_n$  due to aileron deflection (right aileron deflection only).

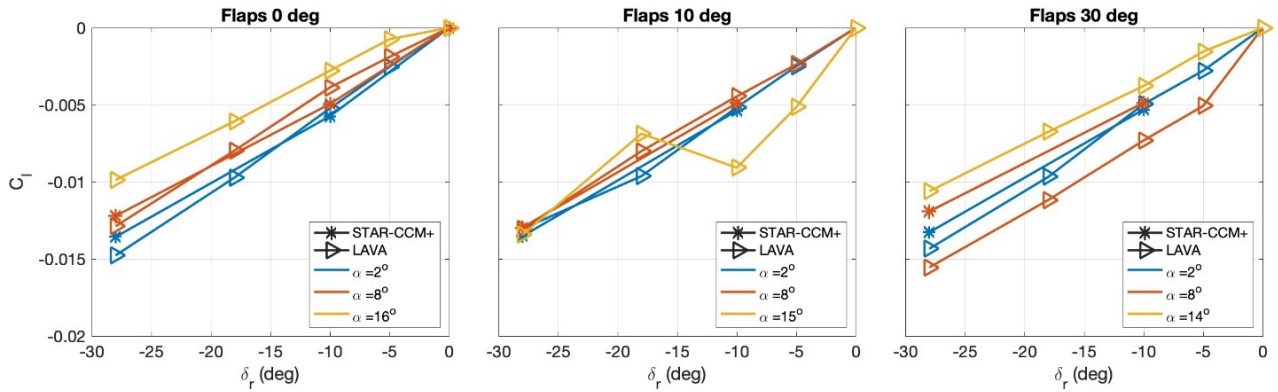


Figure 25. Modification III rolling moment coefficient  $C_l$  due to rudder deflection.

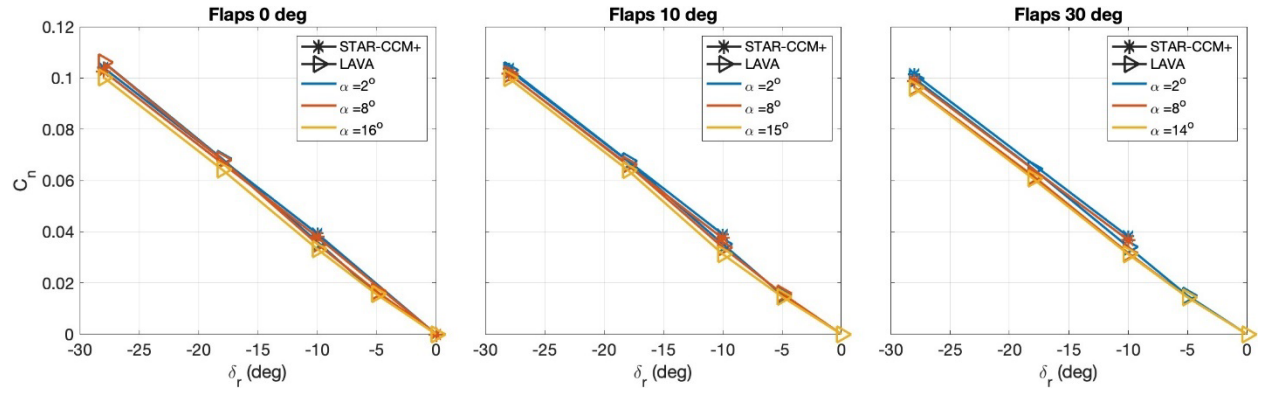


Figure 26. Modification III yawing moment coefficient  $C_n$  due to rudder deflection.

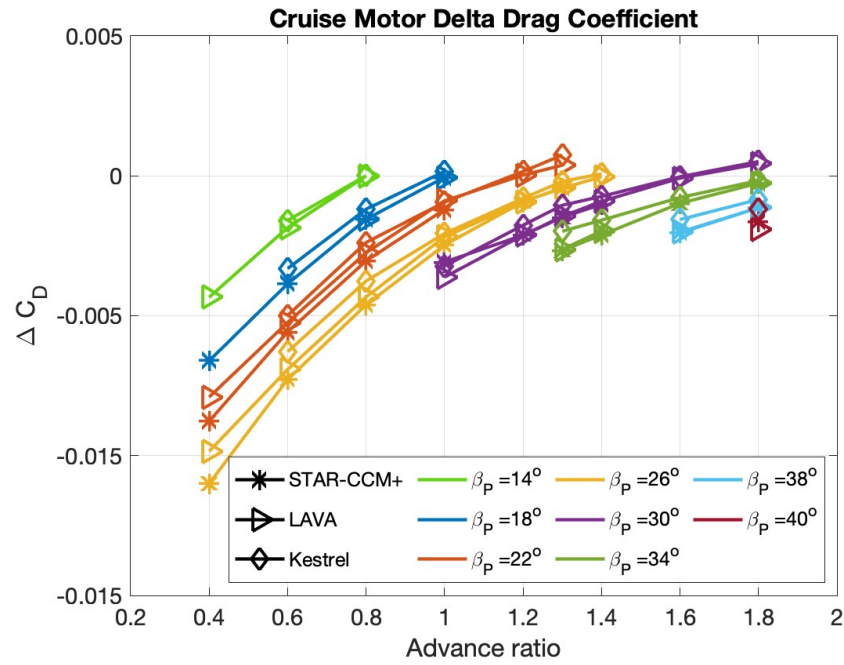


Figure 27. Drag coefficient increment  $\Delta C_D$  due to cruise motor (single motor).

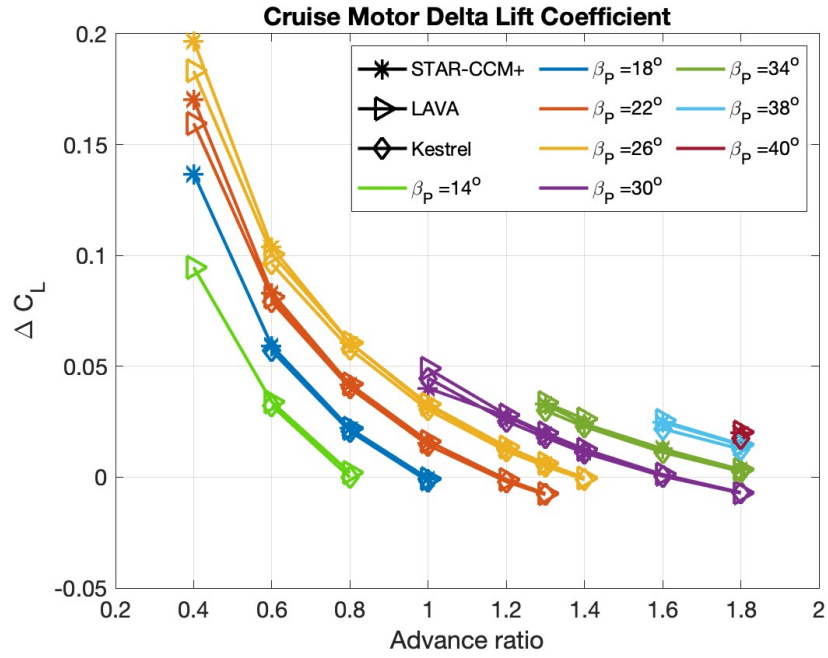


Figure 28. Lift coefficient increment  $\Delta C_L$  due to cruise motor (single motor).

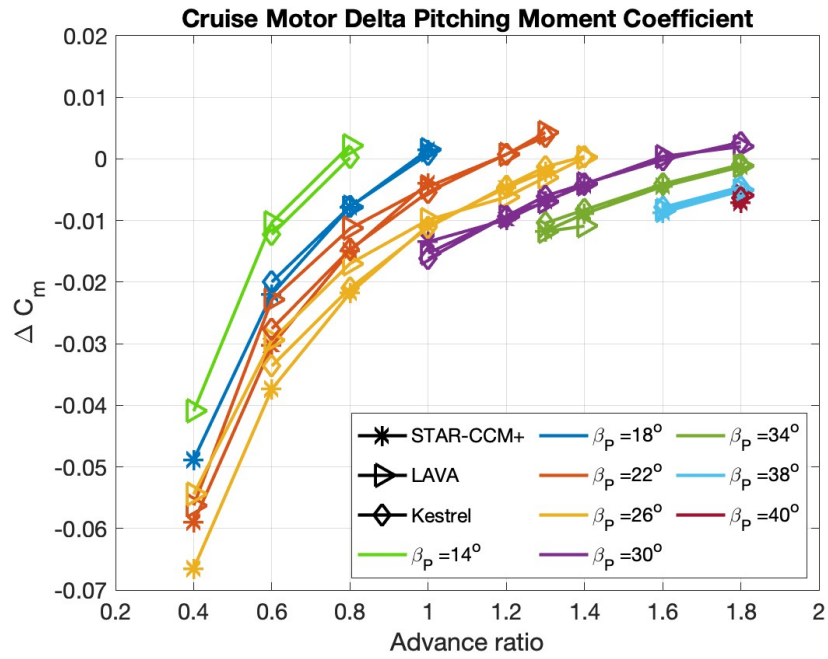


Figure 29. Pitching moment coefficient increment  $\Delta C_m$  due to cruise motor (single motor).

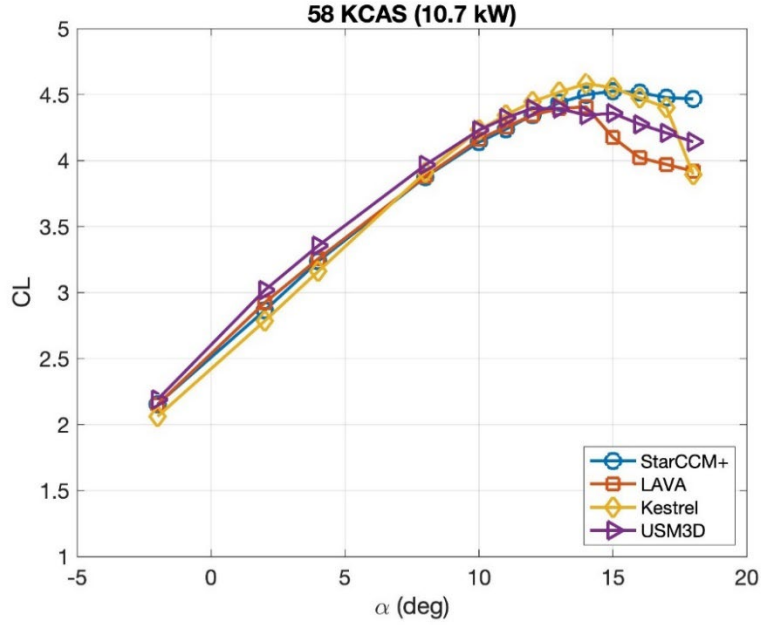


Figure 30. Lift coefficient  $C_L$  due to high-lift system at maximum blowing, flaps at 30 deg.

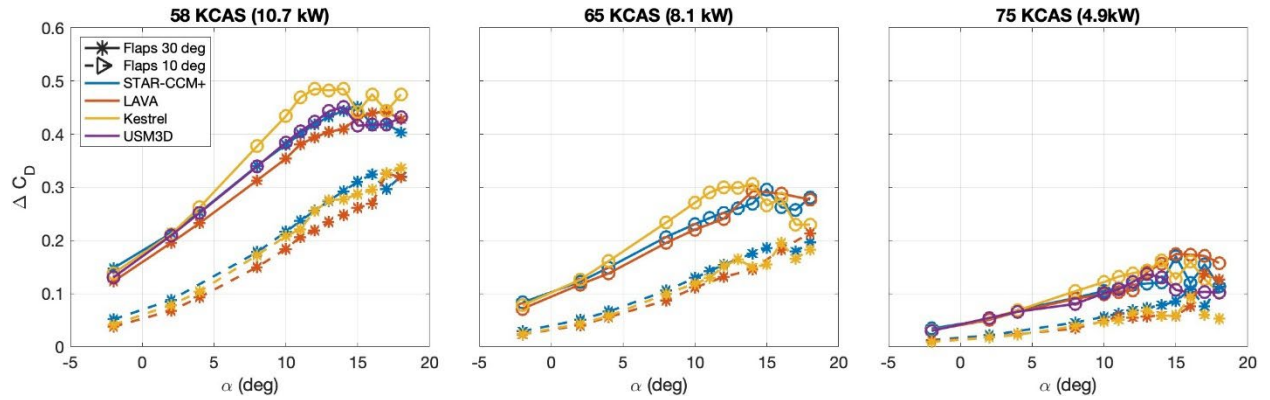


Figure 31. Drag coefficient increment  $\Delta C_D$  due to high-lift motors.

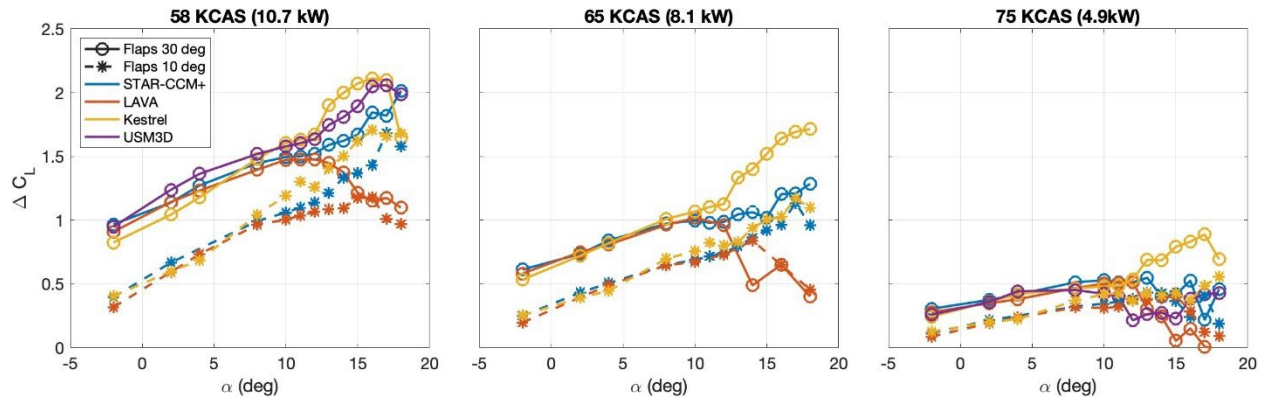


Figure 32. Lift coefficient increment  $\Delta C_L$  due to high-lift motors.

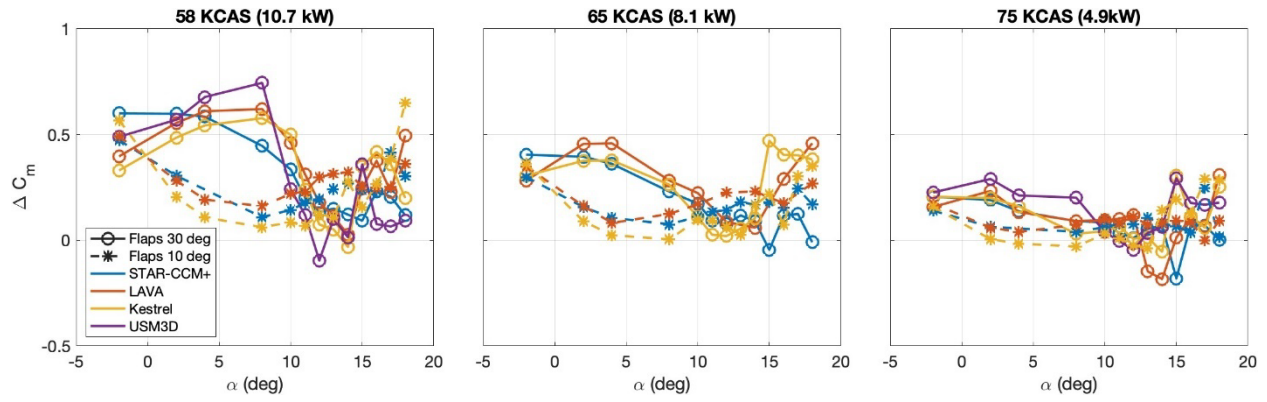


Figure 33. Pitching moment coefficient increment  $\Delta C_m$  due to high-lift motors

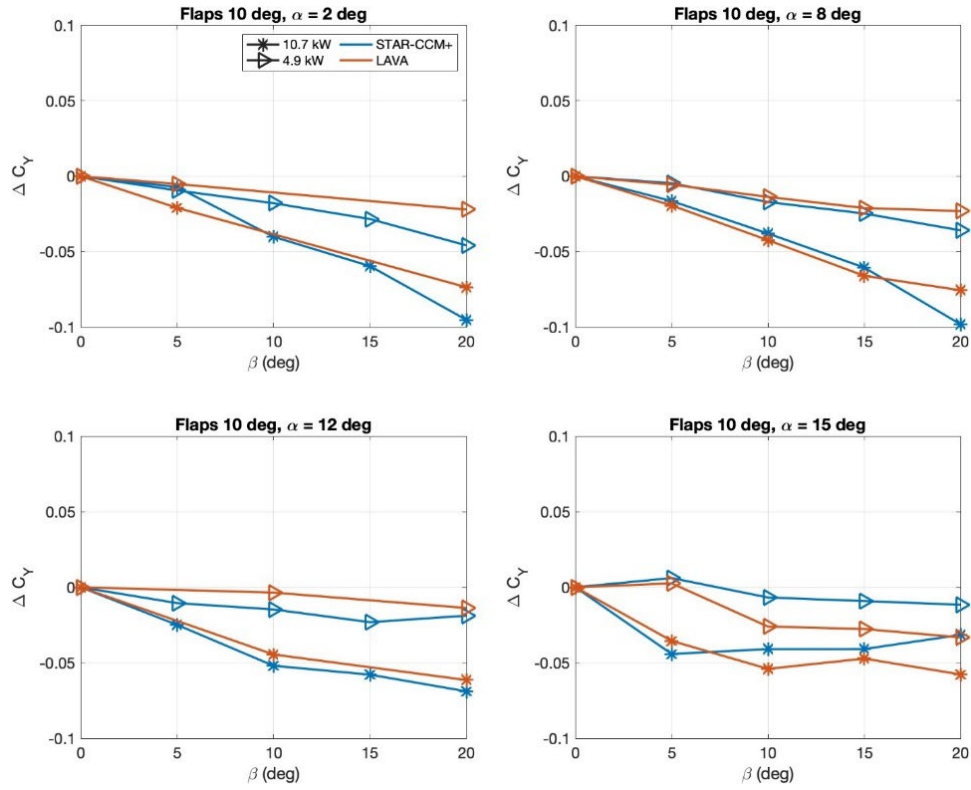


Figure 34. Side force coefficient increment  $\Delta C_y$  due to high-lift blowing, flaps at 10 deg.

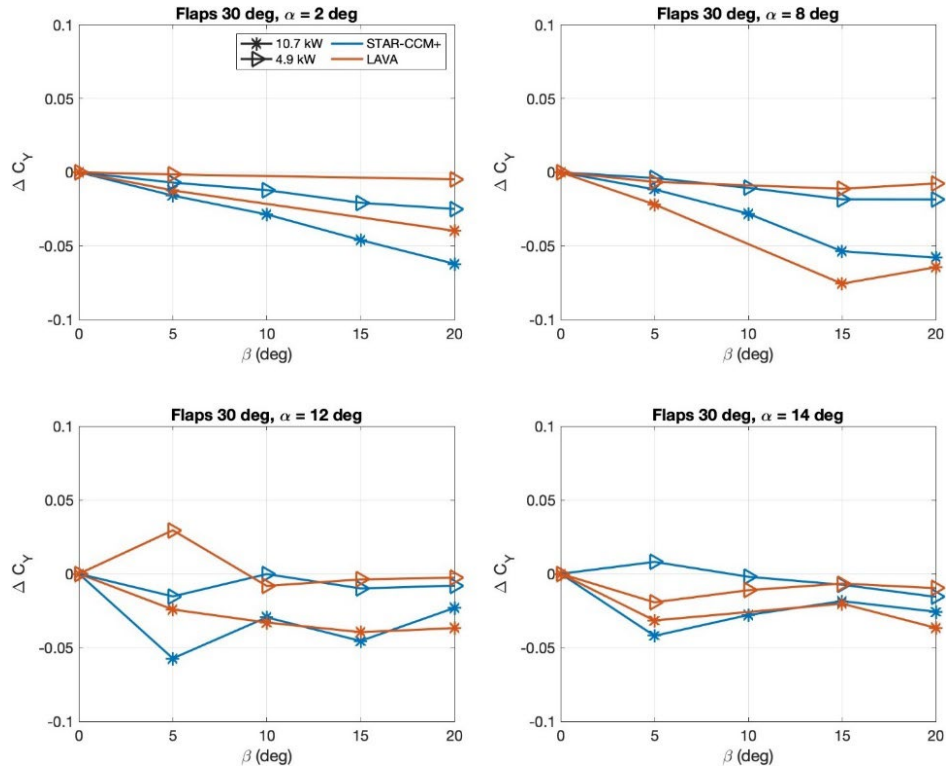


Figure 35. Side force coefficient increment  $\Delta C_Y$  due to high-lift blowing, flaps 30 deg.

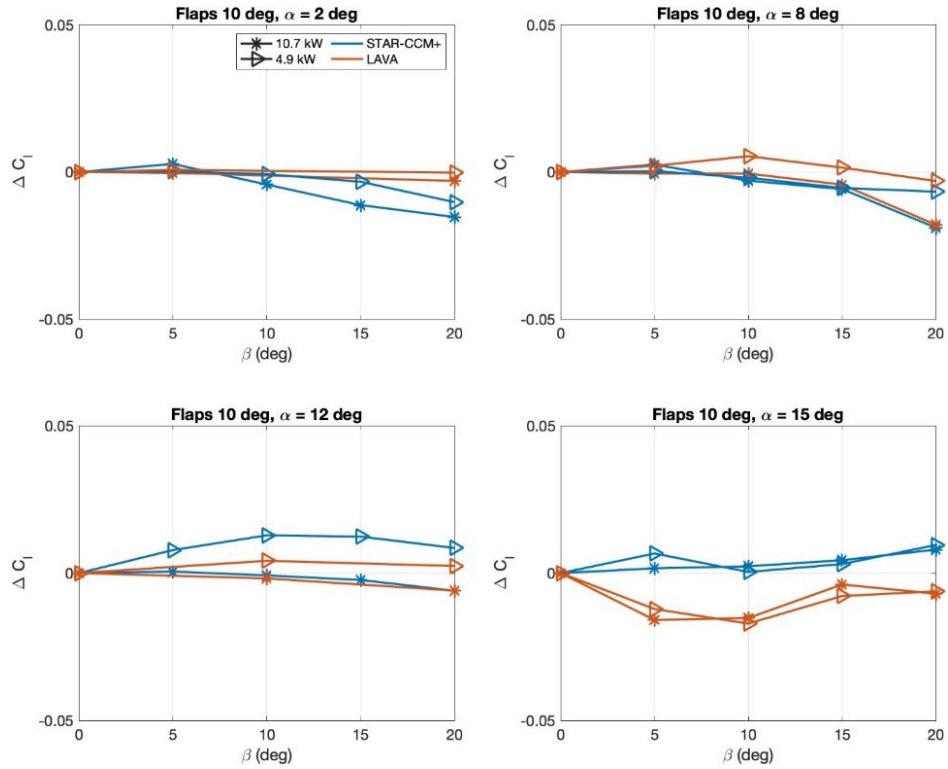


Figure 36. Rolling moment coefficient increment  $\Delta C_l$  due to high-lift blowing, flaps at 10 deg.

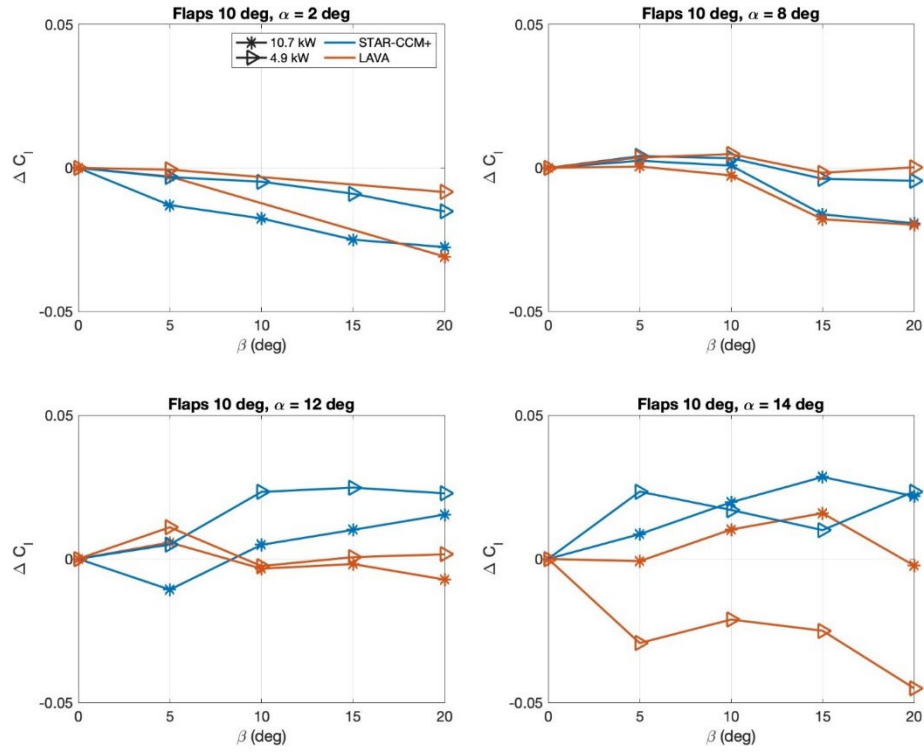


Figure 37. Rolling moment coefficient increment  $\Delta C_l$  due to high-lift blowing, flaps at 30 deg.

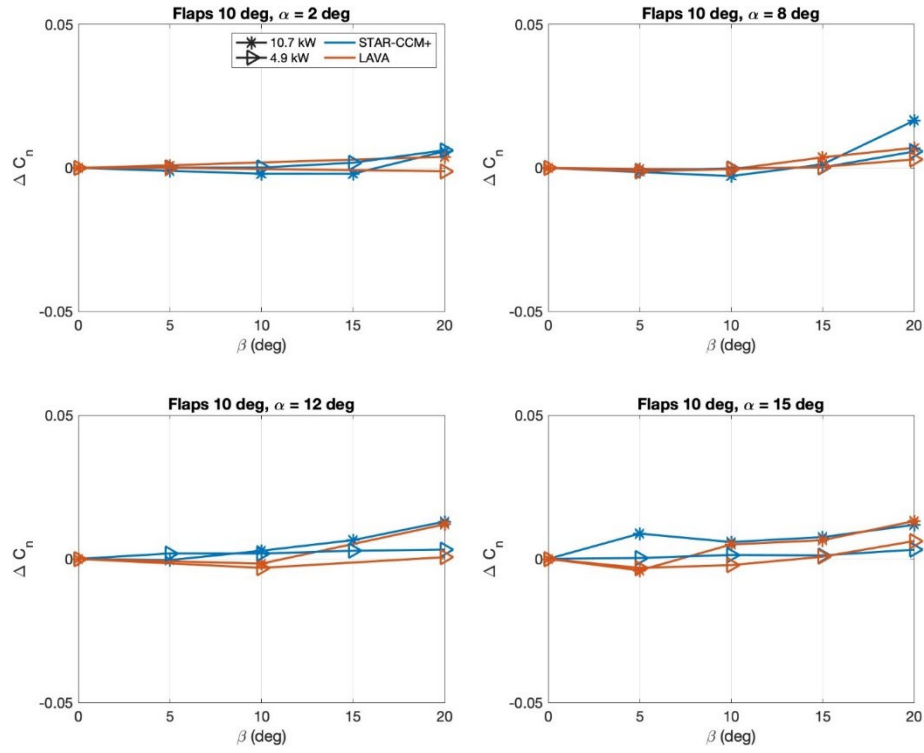


Figure 38. Yawing moment coefficient increment  $\Delta C_n$  due to high-lift blowing, flaps at 10 deg.

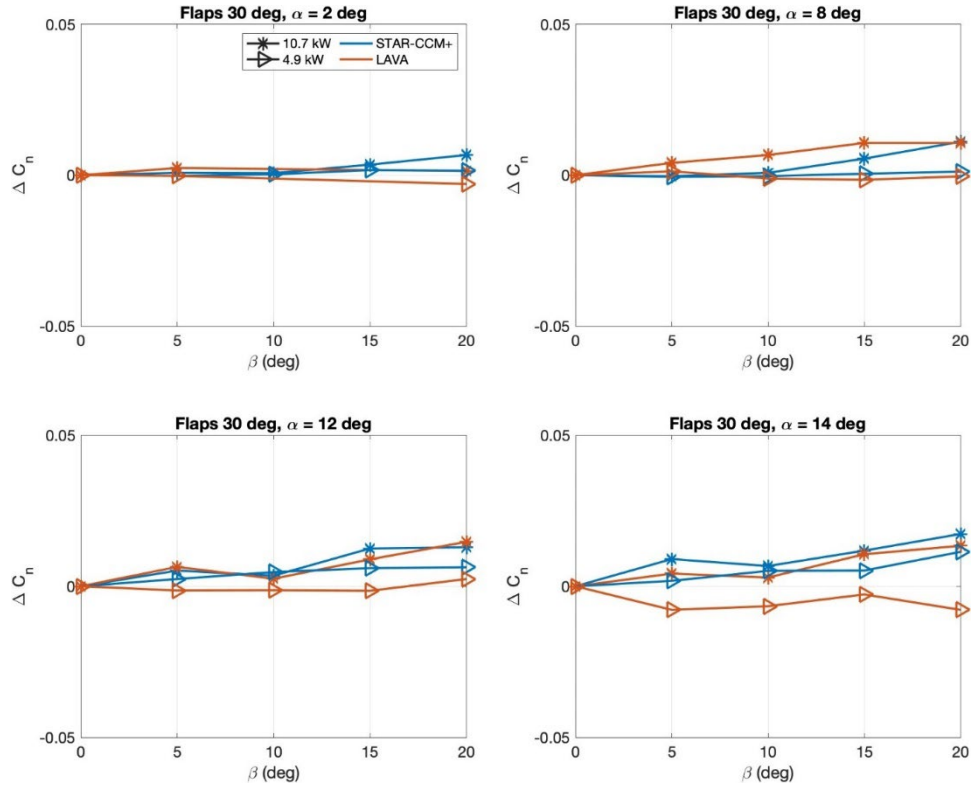


Figure 39. Yawing moment coefficient increment  $\Delta C_n$  due to high-lift blowing, flaps at 30 deg.

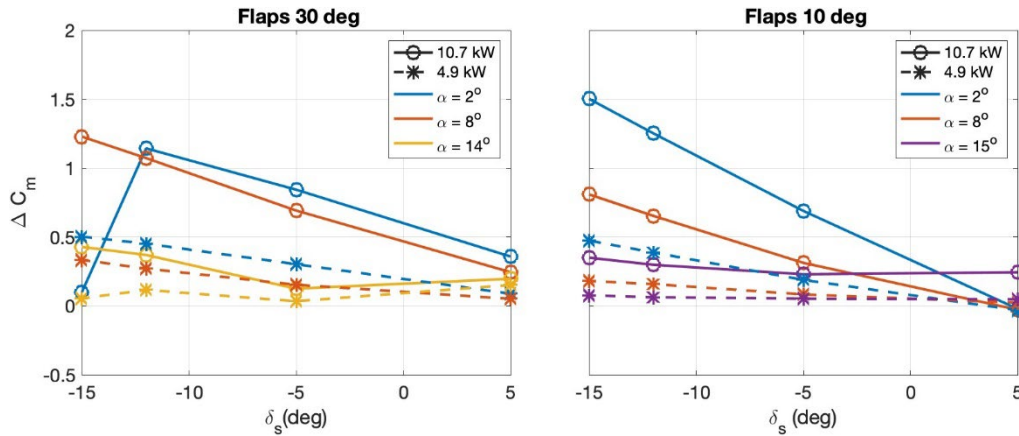


Figure 40. Pitching moment coefficient increment  $\Delta C_m$  due to stabilator deflection with high-lift blowing.

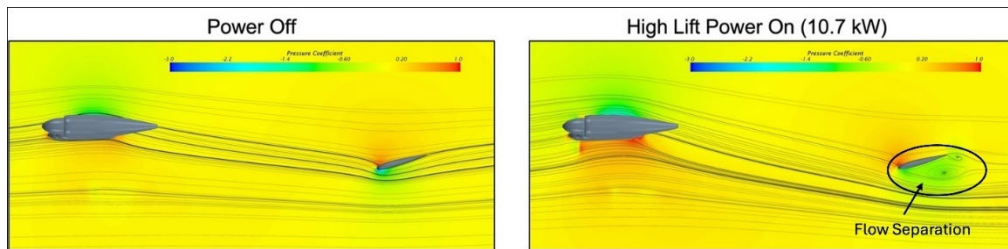


Figure 41. Streamlines showing separation on the horizontal stabilator with high-lift blowing ( $\alpha = 2$  deg,  $\delta_s = -15$  deg).

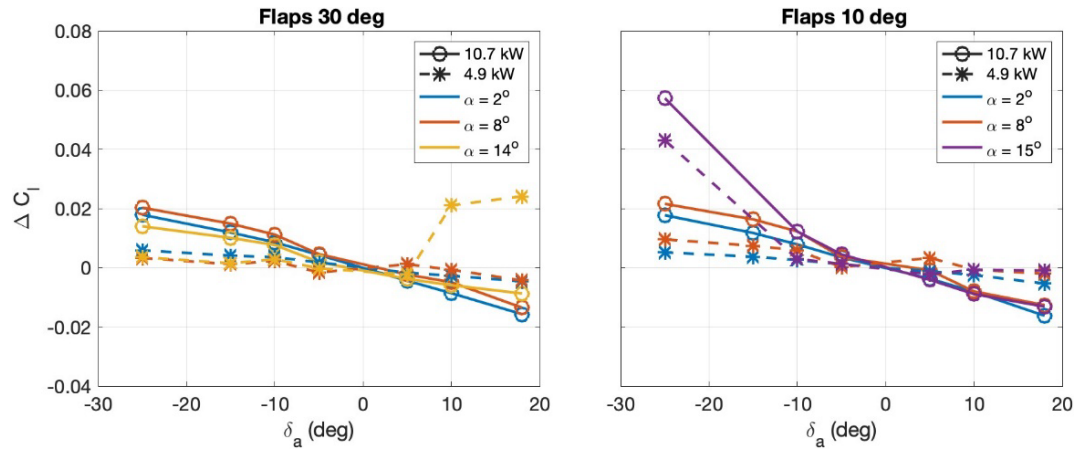


Figure 42. Rolling moment coefficient increment  $\Delta C_l$  due to aileron deflection (singled sided) with high-lift blowing.

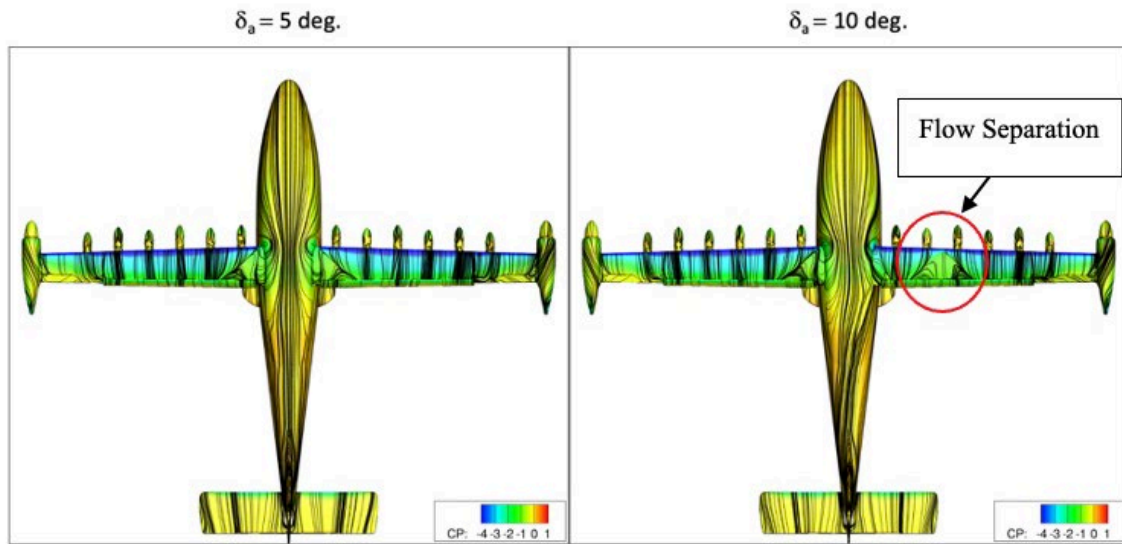


Figure 43. Streamlines showing separation bubble on right wing (right image) due to aileron deflection with high-lift blowing at 4.9 kW, at 14 deg angle of attack.

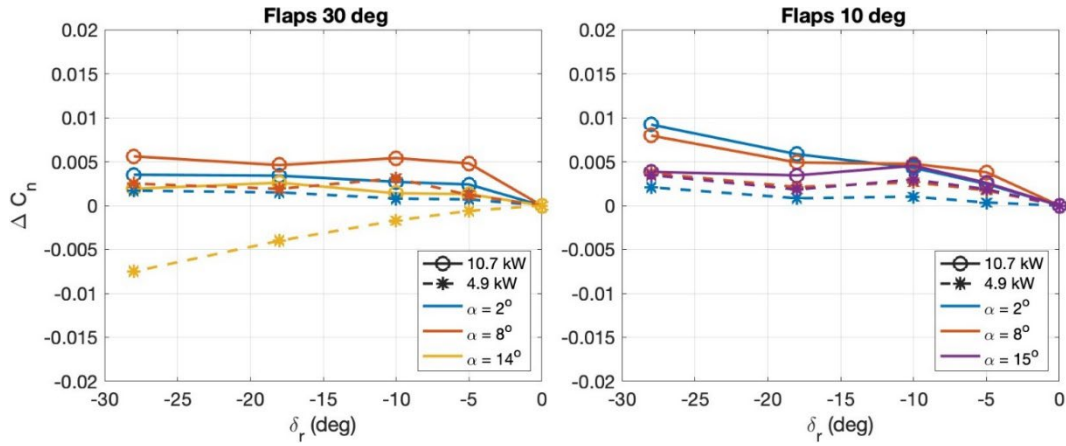


Figure 44. Yawing moment coefficient increment  $\Delta C_n$  due to rudder deflection with high-lift blowing.

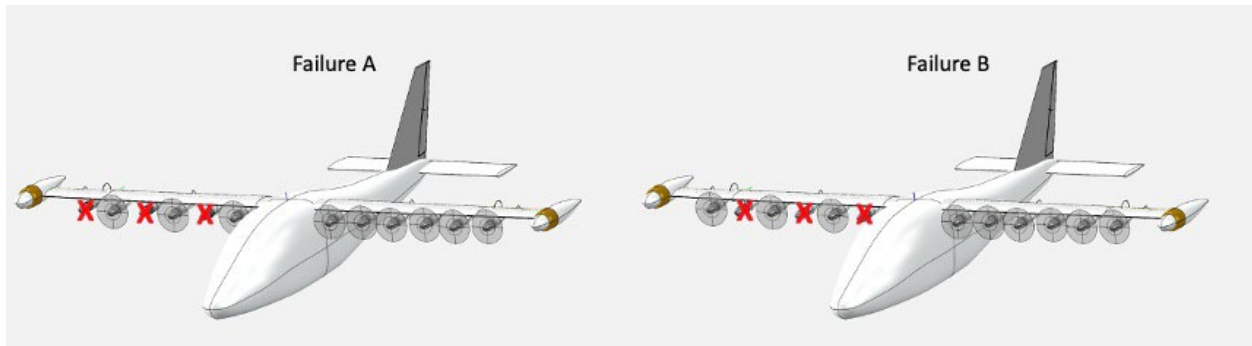


Figure 45. Computation Fluid Dynamics setup for contactor failure cases. Red “x” denotes the failed motor.

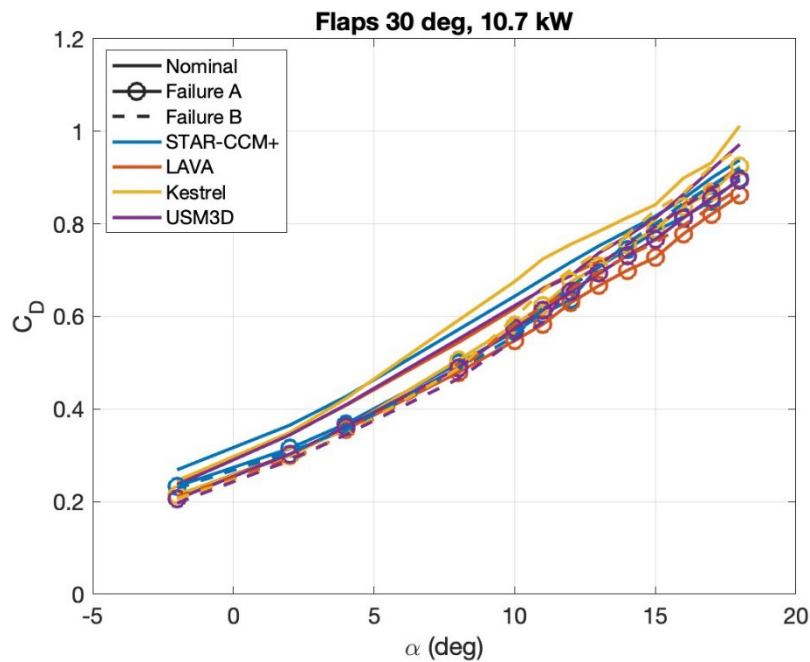


Figure 46. Drag coefficient  $C_D$  comparison for high-lift contactor failures.

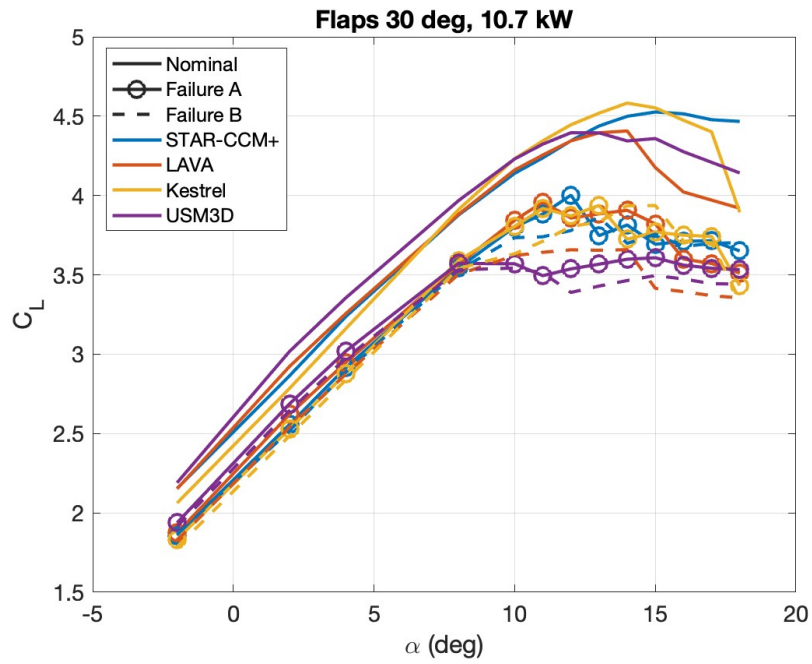


Figure 47. Lift coefficient  $C_L$  comparison for high-lift contactor failures.

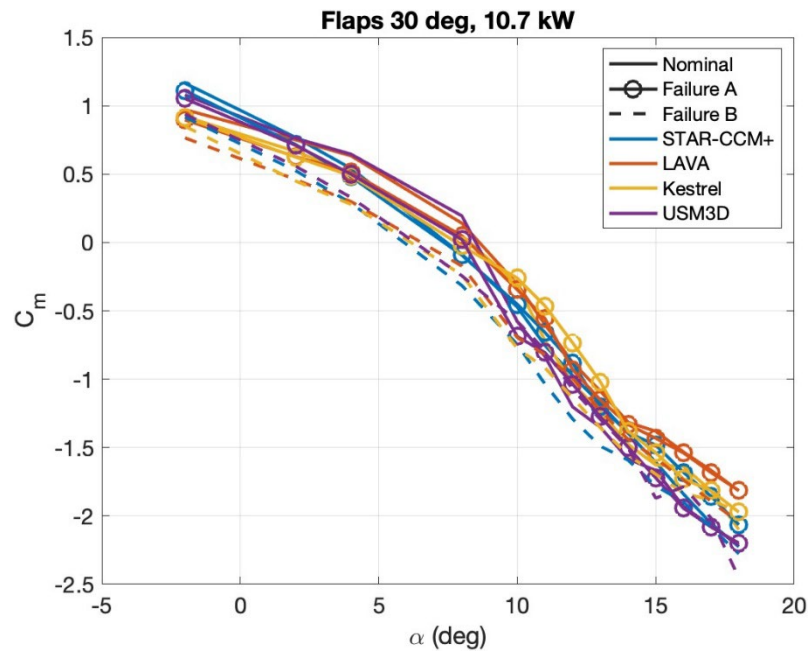


Figure 48. Pitching moment coefficient  $C_m$  comparison for high-lift contactor failures.

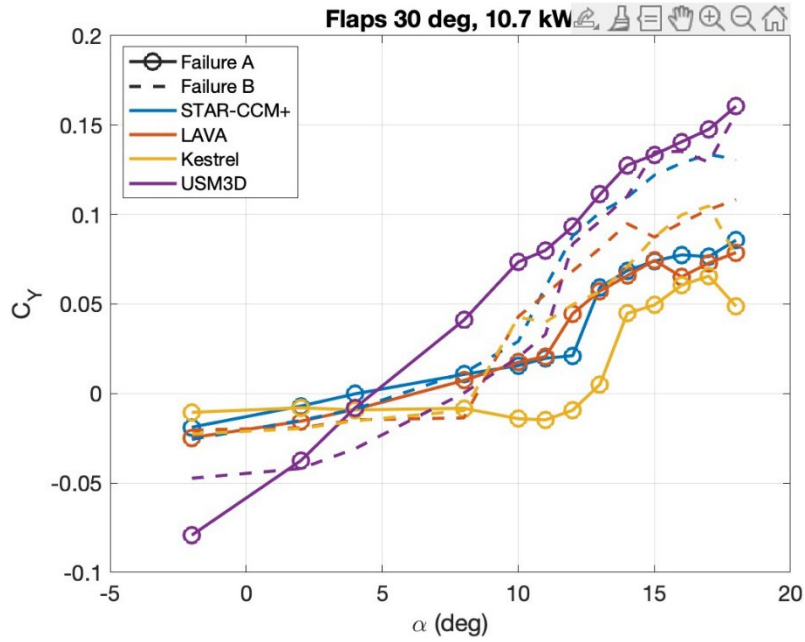


Figure 49. Side force coefficient  $C_Y$  for high-lift contactor failures.

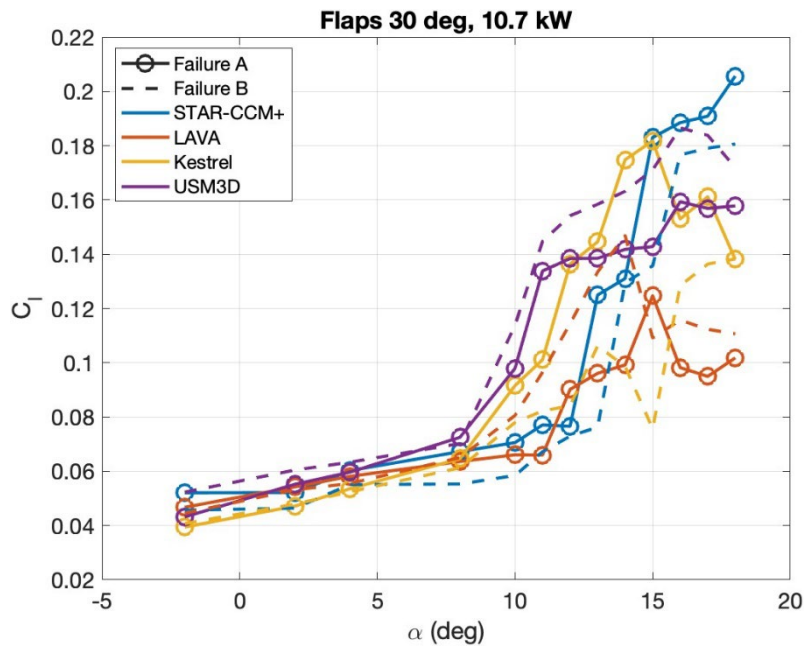


Figure 50. Rolling moment coefficient  $C_l$  for high-lift contactor failures.

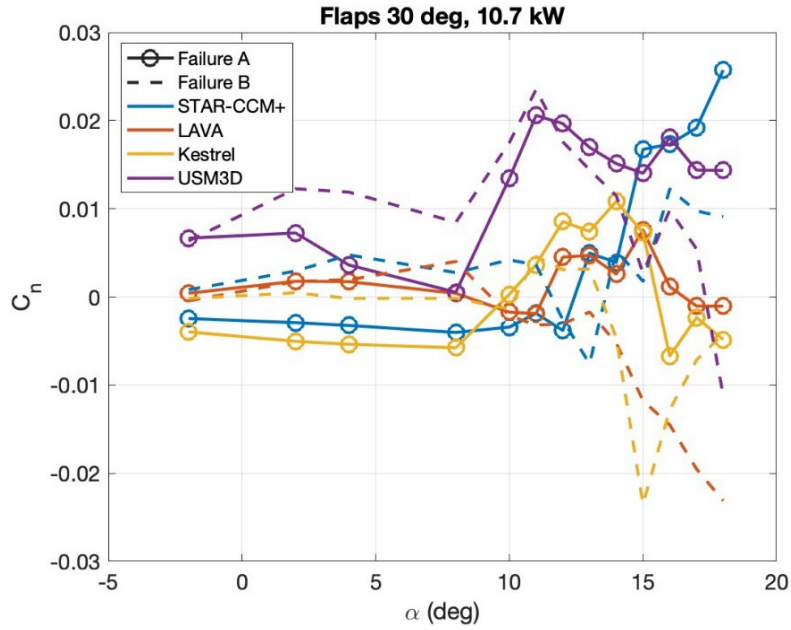


Figure 51. Yawing moment coefficient  $C_n$  comparison for high-lift contactor failures.

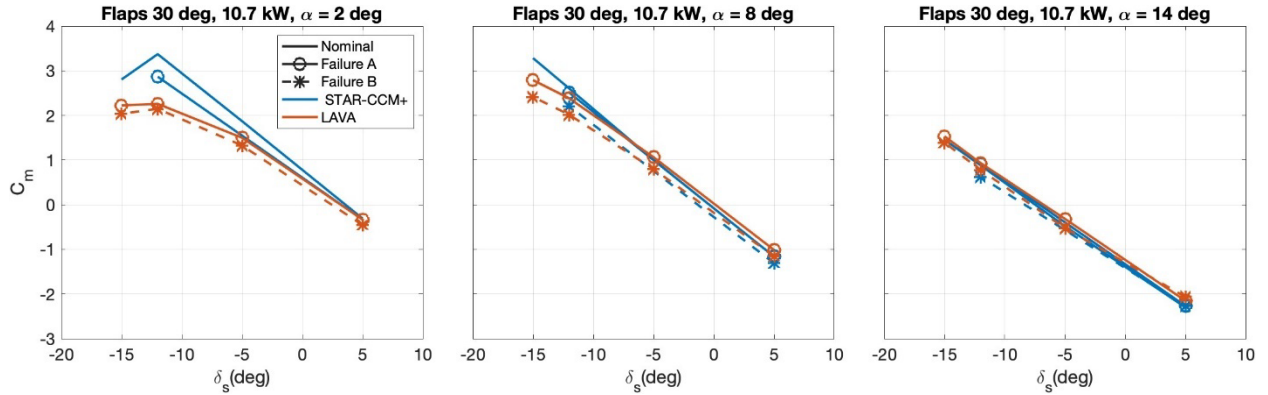


Figure 52. Pitching moment coefficient  $C_m$  due to stabilator deflection for high-lift contactor failures.

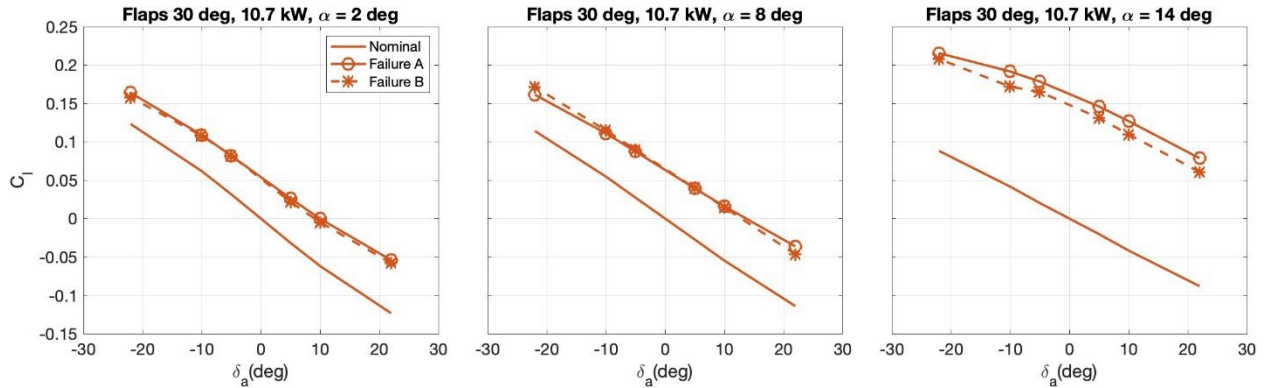


Figure 53. Rolling moment coefficient  $C_l$  due to aileron deflection for high-lift contactor failures (computational fluid dynamics results from LAVA).

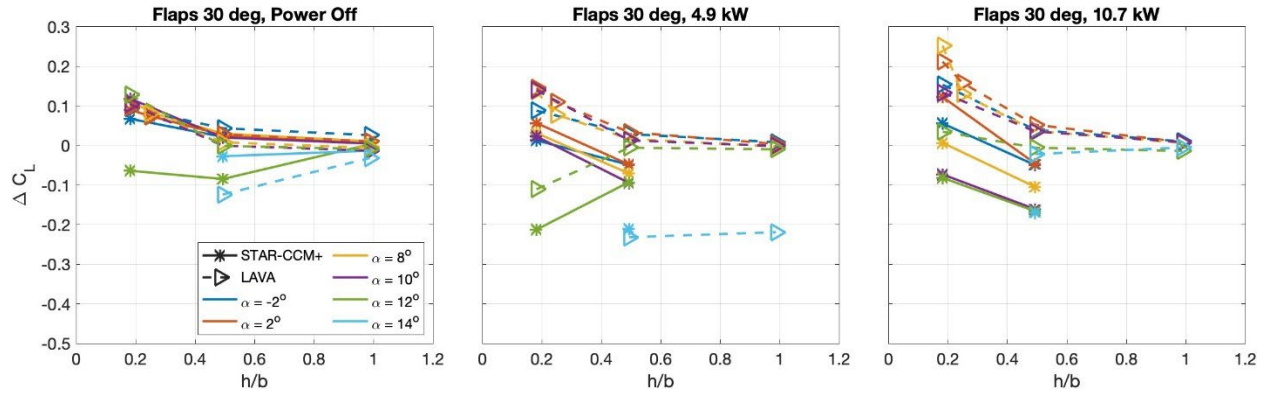


Figure 54. Lift coefficient increment  $\Delta C_L$  in ground effect, flaps at 30 deg.

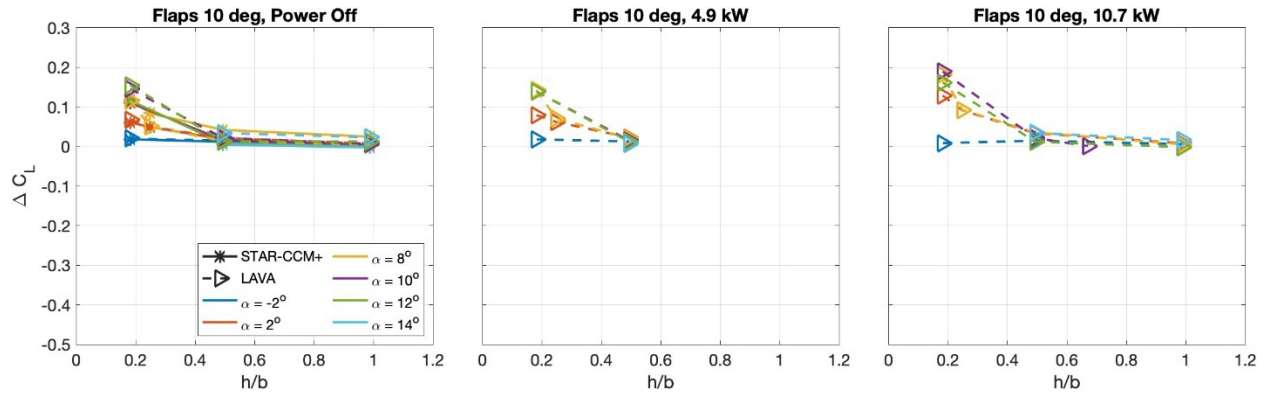


Figure 55. Lift coefficient increment  $\Delta C_L$  in ground effect, flaps at 10 deg.

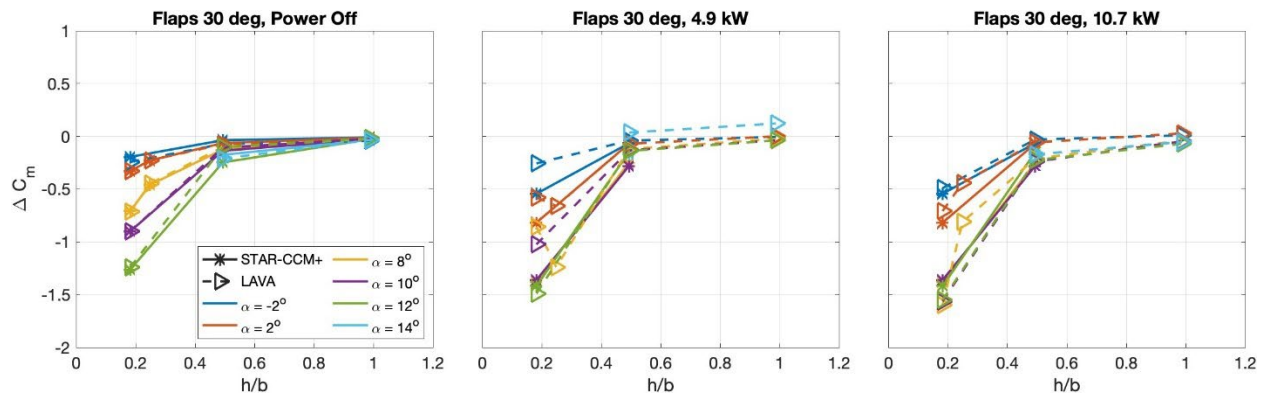


Figure 56. Pitching moment coefficient increment  $\Delta C_m$  in ground effect, flaps at 30 deg.

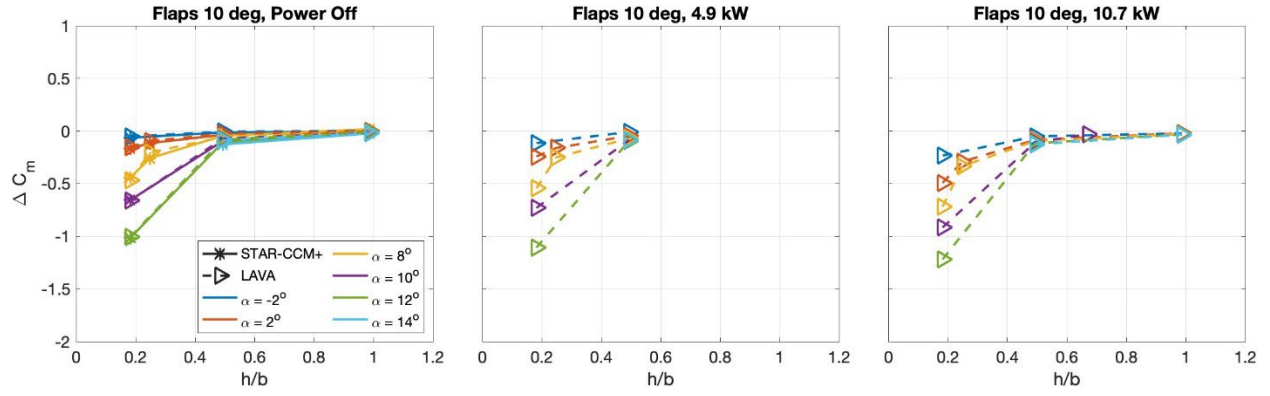


Figure 57. Pitching moment coefficient  $\Delta C_m$  in ground effect, flaps at 10 deg.

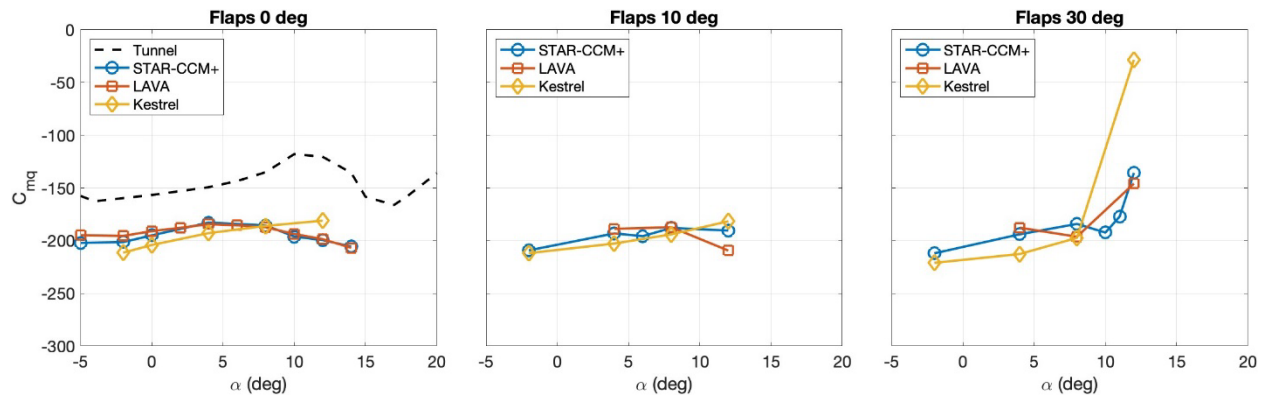


Figure 58. Modification-III pitch damping  $C_{m_q}$ .

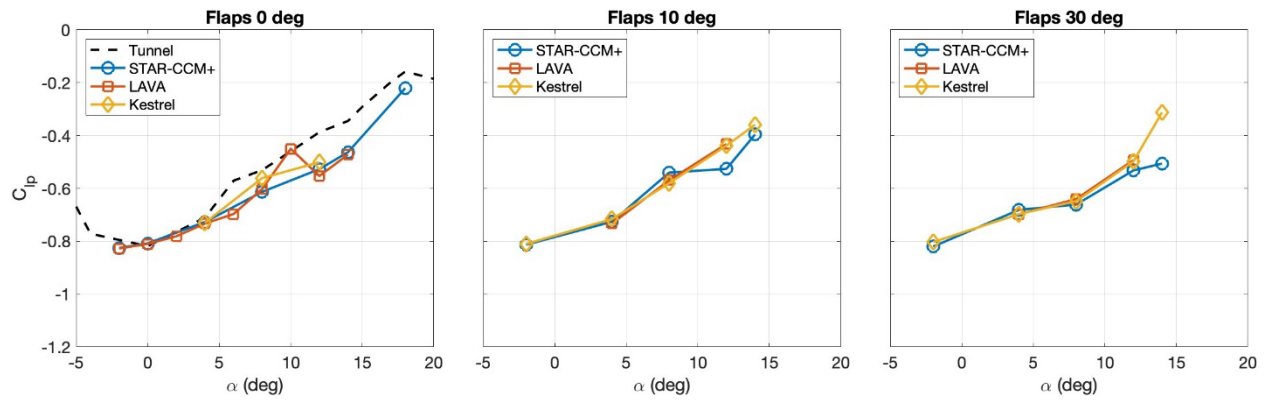


Figure 59. Mod-III roll damping  $C_{l_p}$ .

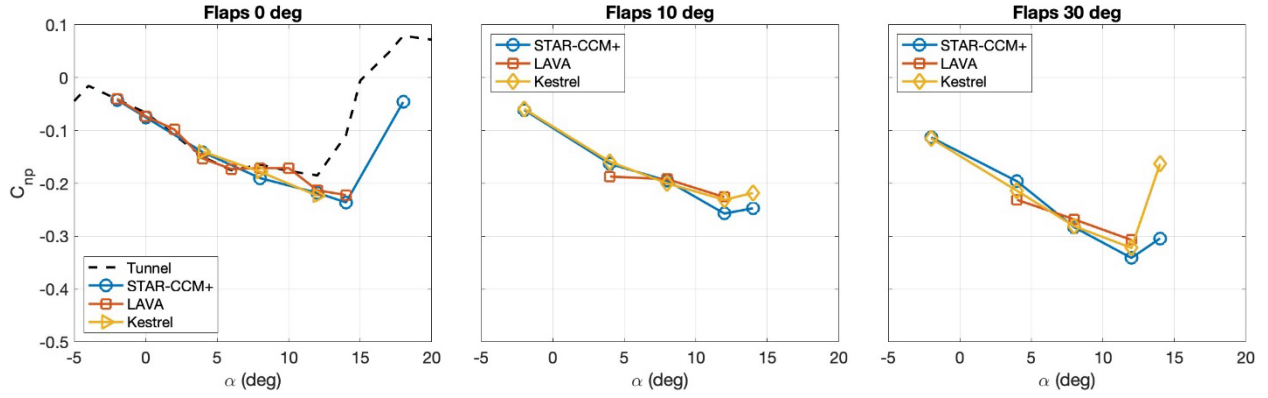


Figure 60. Modification-III yawing moment coefficient due to roll rate  $C_{n_p}$ .

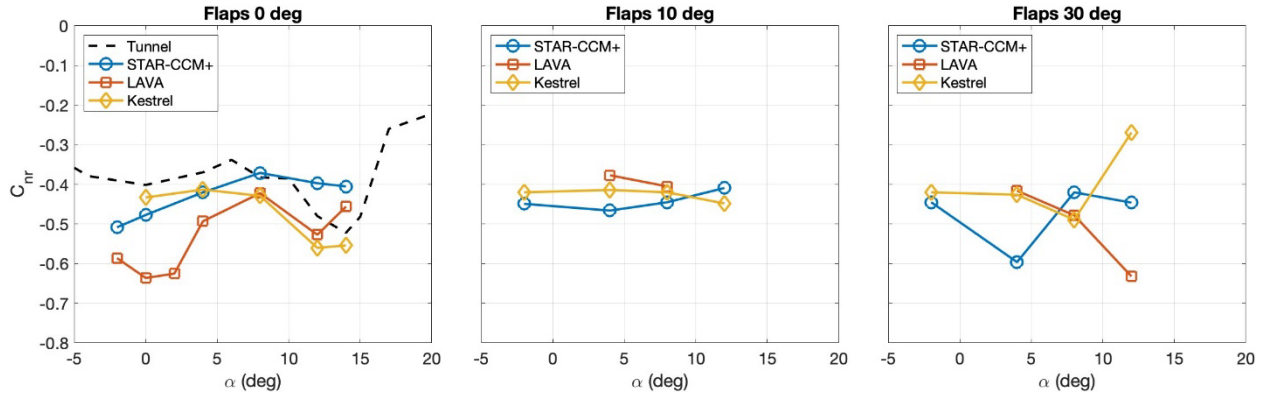


Figure 61. Modification-III yaw damping  $C_{n_r}$ .

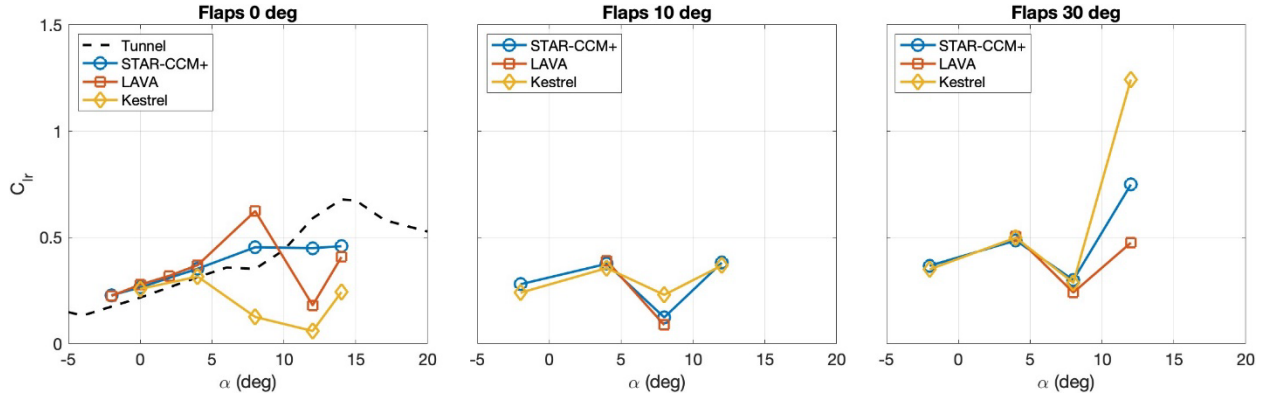


Figure 62. Modification-III rolling moment coefficient due to yaw rate  $C_{l_r}$ .

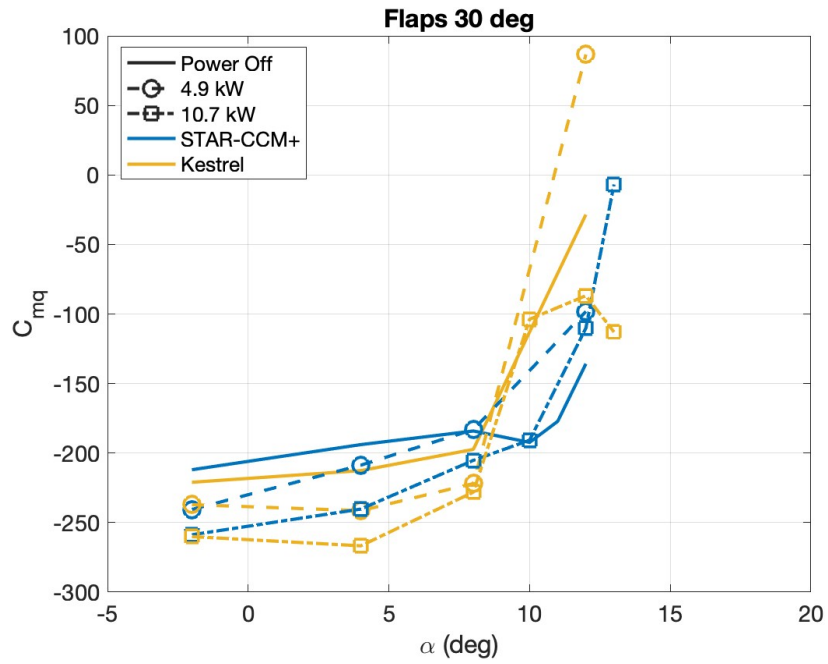


Figure 63. Pitch damping coefficient  $C_{mq}$  with high-lift power on and power off.

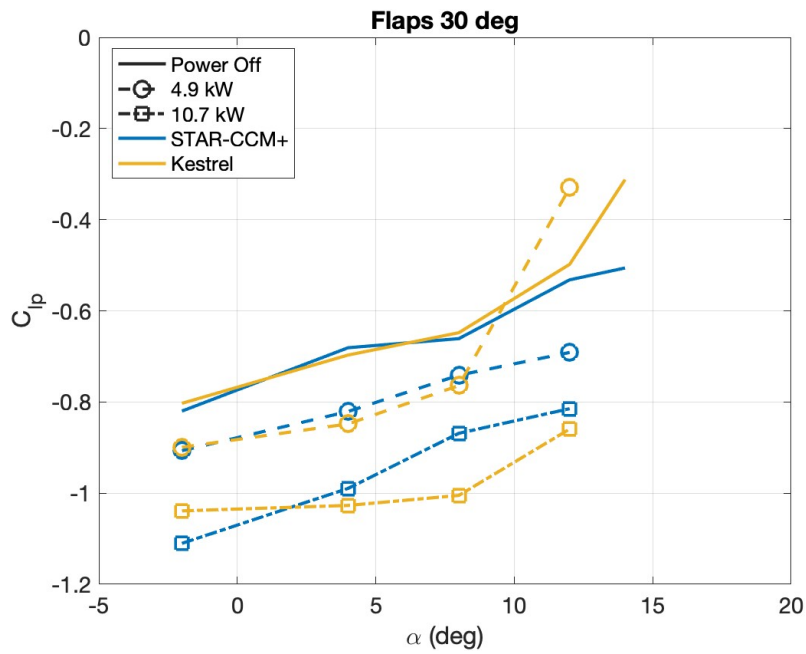


Figure 64. Roll damping coefficient  $C_{lp}$  with high-lift power on and power off.

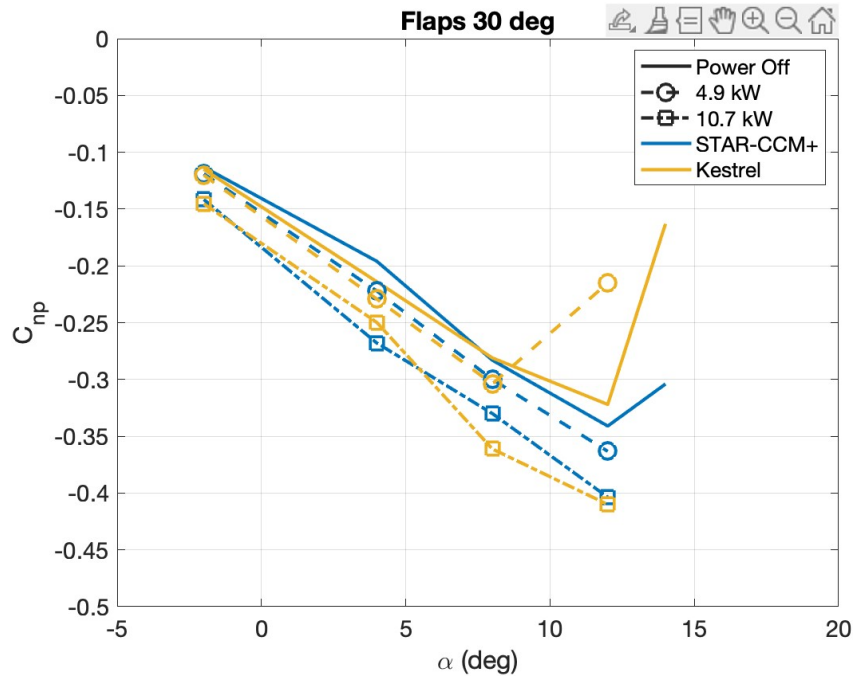


Figure 65. Yawing moment coefficient due to roll rate  $C_{n_p}$  with high-lift power on and power off.

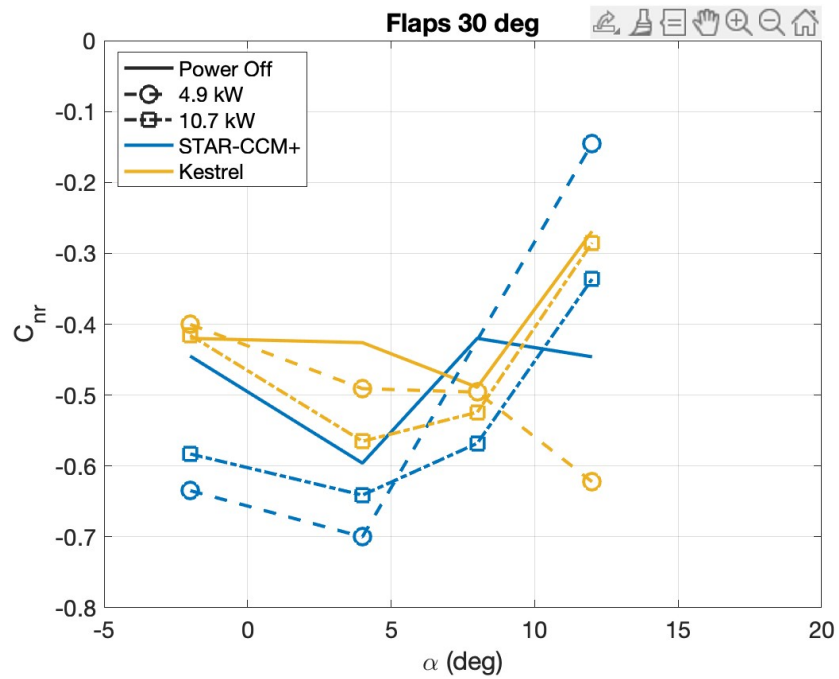


Figure 66. Yaw damping coefficient  $C_{n_r}$  with high-lift power on and power off.

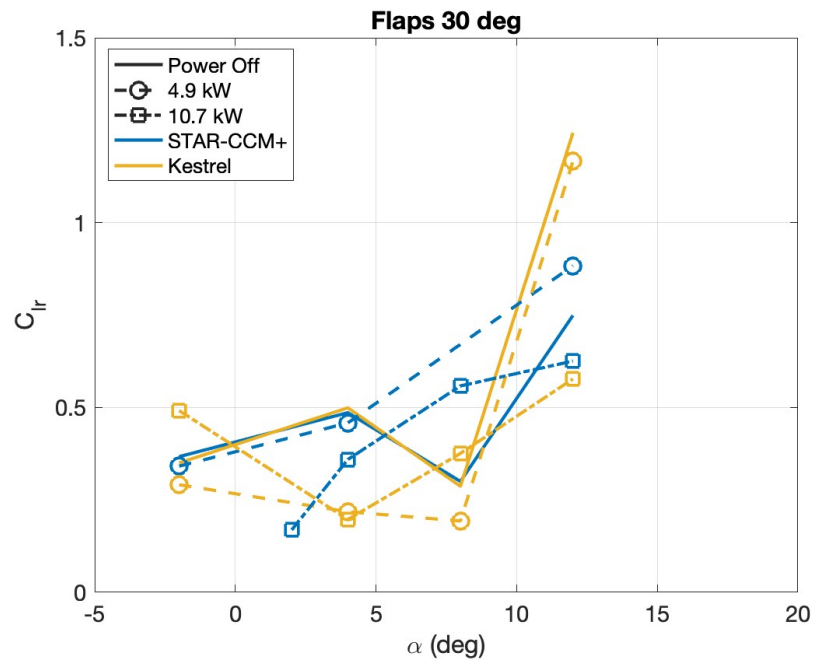


Figure 67. Rolling moment coefficient due to yaw rate  $C_{lr}$  with high-lift power on and power off.

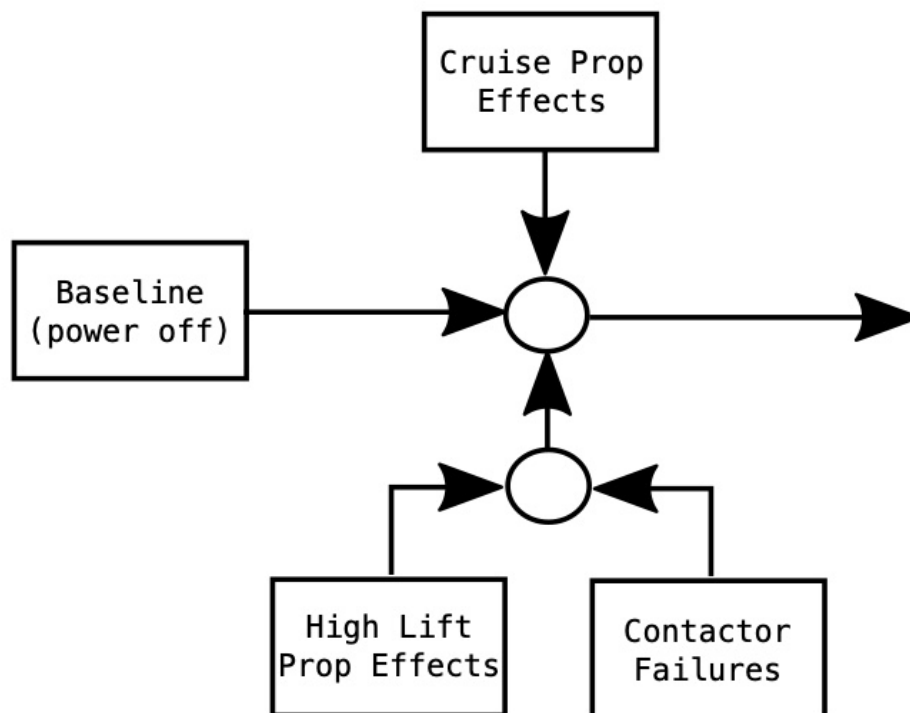


Figure 68. Aerodynamic model structure used in the aero database for the desktop and piloted simulations.

## 9 References

1. National Aeronautics and Space Administration (NASA), *NASA Aeronautics Strategic Implementation Plan – 2019 Update*, URL: <https://www.nasa.gov/sites/default/files/atoms/files/sip-2019-v7-web.pdf> Accessed February 26, 2025.
2. Clarke, S., Redifer, M., Papathakis, K., Samuel, A., and Foster, T., “X-57 Power and Command System Design,” *IEEE Transportation Electrification Conference and Expo*, Chicago, IL, 2017, URL: <https://ntrs.nasa.gov/citations/20170005797> Accessed February 26, 2025.
3. Borer, N., et al., “Design and Performance of the NASA SCEPTOR Distributed Electric Propulsion Flight Demonstrator,” *AIAA Aviation Technology, Integration, and Operations Conference*, Washington, DC, 2016, AIAA 2016-3920. URL: <https://ntrs.nasa.gov/citations/20160010157> Accessed February 26, 2025.
4. Clarke, S., et al., “X-57 Power and Command System Design,” *IEEE Transportation Electrification Conference and Expo*, Chicago, IL, 2017. URL: <https://ntrs.nasa.gov/citations/20170005797> Accessed February 26, 2025.
5. Dubois, A., van der Geest, M., Bevirt, J. B., Clarke, S., Christie, R. J., and Borer, N. K., “Design of an Electric Propulsion System for SCEPTOR,” *AIAA Aviation Technology, Integration, and Operations Conference*, Washington, DC, 2016, AIAA 2016-3925, 2016. URL: <https://ntrs.nasa.gov/citations/20160007774> Accessed February 26, 2025.
6. Viken, Jeffrey K., Viken, Sally A., Deere, Karen A., and Carter, Melissa B., “Design of the Cruise and Flap Airfoil for the X-57 Maxwell Distributed Electric Propulsion Aircraft,” *AIAA Aviation and Aeronautics Forum and Exposition*, Denver, CO, AIAA, 2017-3922. URL: <https://ntrs.nasa.gov/citations/20180003474> Accessed February 26, 2025.
7. Deere, Karen A., Viken, Jeffrey K., Viken, Sally A., Carter, Melissa B., Wiese, Michael R., and Farr, Norma, “Computational Analysis of a Wing Designed for the X-57 Distributed Electric Propulsion Aircraft,” *AIAA Aviation Forum*, Denver, CO, 2017, AIAA 2017-3923. URL: <https://ntrs.nasa.gov/citations/20170005883> Accessed February 26, 2025.
8. Patterson, Michael D., Derlaga, Joseph M., and Borer, Nicholas K., “High-Lift Propeller System Configuration Selection for NASA’S SCEPTOR Distributed Electric Propulsion Flight Demonstrator,” *AIAA Aviation Technology, Integration, and Operations Conference*, Washington, DC, AIAA 2016-3922. URL: <https://ntrs.nasa.gov/citations/20160010105> Accessed February 26, 2025.
9. Patterson, Michael D., and Borer, Nicholas K., “Approach Considerations in Aircraft with High-Lift Propeller Systems,” *AIAA Aviation, Technology, Integration and Operations Conference*, Denver, CO, AIAA 2017-3782. URL: <https://ntrs.nasa.gov/citations/20170005869> Accessed February 26, 2025.
10. Litherland, Brandon L., and Derlaga, Joseph M., “A Performance Analysis of Folding Conformal Propeller Blade Designs,” *AIAA Aviation 2019 Forum*, Dallas, TX, 2019, AIAA 2019-3676. URL: <https://ntrs.nasa.gov/citations/20200002658> Accessed February 26, 2025.
11. Borer, Nicholas K., and Patterson, Michael D., “X-57 High-Lift Propeller Control Schedule Development,” *AIAA Aviation 2020 Forum*, Virtual Event, AIAA 2020-3091. [https://ntrs.nasa.gov/api/citations/20205010303/downloads/Borer\\_Patterson\\_high-lift\\_propeller\\_schedule-manuscript-final\\_2020-05-05.pdf](https://ntrs.nasa.gov/api/citations/20205010303/downloads/Borer_Patterson_high-lift_propeller_schedule-manuscript-final_2020-05-05.pdf) Accessed February 26, 2025.
12. Siemens, “Simcenter Star-CCM+ v13.06,” 2018. URL: <https://plm.sw.siemens.com/en-US/simcenter/fluids-thermal-simulation/star-ccm/> Accessed March 11, 2025.
13. Kiris, Cetin C., Housman, Jeffrey A., Barad, Michael F., Brehm, Christoph, Sozer, Emre, and Moini-Yekta, Shayan, “Computational Framework for Launch, Ascent, and Vehicle Aerodynamics (LAVA),” *Aerospace Science and Technology*, Vol. 55, 2016, pp. 189–219.
14. Frink, N. T., Pirzadeh, S. Z., Parikh, P. C., Pandya, M. J., and Bhat, M. K. “The NASA Tetrahedral Unstructured Software System,” *The Aeronautical Journal*, Vol. 104, No. 1040, October 2000, pp. 491–499.

15. McDaniel, David R., and Tuckey, Todd R., "HPCMP CREATE™-AV Kestrel New Capabilities and Future Directions," *AIAA SciTech 2019 Forum 2019*, San Diego, CA, 7-11 January, AIAA 2019-0840, 2019.
16. Shafer, T. C., Green, B. E., Hallissy, B. P., and Hine, D. H., "Advanced Navy Applications Using CREATE™-AV Kestrel," *AIAA SciTech, 52nd Aerospace Sciences Meeting*, National Harbor, MD, AIAA 2014-0418, 13-17 January 2014.
17. Spalart, S., and Allmaras, S., "A One-Equation Turbulence Model for Aerodynamic Flows," *AIAA 30th Aerospace Sciences Meeting and Exhibit*, Reno, NV, 1992.
18. Shur, Michael L., Strelets, Michael K., Travin, Andre K., and Spalart, Philippe R., "Turbulence Modeling in Rotating and Curved Channels: Assessing the Spalart-Shur Correction," *AIAA Journal*, Vol. 38, No. 5, May 2000, pp. 784-792.
19. Venkatakrishnan, V., "On the accuracy of limiters and convergence to steady state solutions," Tech. rep., AIAA-93-0880, 1994.
20. Housman, J. A., Kiris, C. C., and Hafez, M. M., "Time-derivative Preconditioning Methods for Multicomponent Flows—Part I: Riemann Problems," *Journal of Applied Mechanics*, Vol. 76, No. 2, 2009.
21. Housman, Jeffrey A., Kiris, Cetin C., and Hafez, Mohamed M., "Time-derivative Preconditioning Methods for Multicomponent Flows—Part II: Two-dimensional Applications," *Journal of Applied Mechanics*, Vol. 76, Issue 2, 2009. <https://doi.org/10.1115/1.3086592>.
22. Saad, Youcef., and Schultz, Martin H., "GMRES "A Generalized Minimal Residual Algorithm for Solving Nonsymmetric Linear Systems," *SIAM Journal on Scientific and Statistical Computing*, Vol. 7, No. 3, 1986, pp. 856–869.
23. Chan, William M., "Overset Grid Technology Development at NASA Ames Research Center," *Computers & Fluids*, Vol. 38, No. 3, 2009, pp. 496–503.
24. Pointwise, "Grid Generation Software," 2022. URL <https://www.pointwise.com/pointwise/index.html>, [Online; accessed 31-May-2022].
25. Chan, William, "Developments in Strategies and Software Tools for Overset Structured Grid Generation and Connectivity," *20th AIAA Computational Fluid Dynamics Conference*, Honolulu, Hawaii, 2011.
26. Duensing, J. C., Yoo, S. Y., Maldonado, D., Housman, J. A., Jensen, J. C., and Kiris, C. K., "Establishing Best Practices for X-57 Maxwell CFD Database Generation," *AIAA SciTech 2019 Forum*, 7-11 January, AIAA 2019-0274, 2019.
27. Jensen, J. C., Stich, G.D., Housman, J. A., Denison, M., and Kiris, C. C. San Diego, CA, 2056.
28. Kiris, C. C., Ghate, A. S., Duensing, J. C., Browne, O. M., Housman, J. A., Stich, G-D., Kenway, G., Dos Santos Fernandes, L. M., and Machado, L. M., "High-Lift Common Research Model: RANS, HRLES, and WMLES perspectives for CLmax prediction using LAVA," *AIAA SciTech 2022 Forum*, p. 1554, AIAA 2022-1554, 2022.
29. K. A. Deere, Viken, J. K., Viken, S. A., Carter, M. B., Wiese, M. R., and Farr, N. L., *Computational Analysis of the X-57 Airplane at Unpowered Conditions (Preliminary Fuselage)*, NASA/TM20220011034, April 2022. URL: <https://ntrs.nasa.gov/citations/20210011034> Accessed February 26, 2025.
30. McDaniel, D. R., and Tuckey, T.R., "HPCMP CREATE™-AV Kestrel New Capabilities and Future Directions," *AIAA SciTech 2019 Forum*, San Diego, CA, 7-11 January, AIAA 2019-0840, 2019.
31. Shafer, T. C., Green, B. E., Hallissy, B. P., and Hine, D. H., "Advanced Navy Applications Using CREATE™-AV Kestrel," *AIAA SciTech, 52nd Aerospace Sciences Meeting*, National Harbor, MD, 13-17 January, AIAA 2014-0418, 2014.
32. Mark S. Smith, *Analysis of Wind Tunnel Oscillatory Data of the X-31A Aircraft*, NASA/CR-1999-208725, 1999. URL: <https://ntrs.nasa.gov/citations/19990018654> Accessed February 26, 2025.